MICROMACHINED ELECTRICAL FIELD-FLOW FRACTIONATION SYSTEMS WITH ON-COLUMN ELECTRICAL AND RESONANCE LIGHT SCATTERING DETECTION MODALITIES

A Dissertation
Presented to
The Academic Faculty

by

Mason Rencher Graff

In Partial Fulfillment
of the Requirements for the Degree
Doctor of Philosophy in the
School of Electrical and Computer Engineering

Georgia Institute of Technology
May 2006

MICROMACHINED ELECTRICAL FIELD-FLOW FRACTIONATION SYSTEMS WITH ON-COLUMN ELECTRICAL AND RESONANCE LIGHT SCATTERING DETECTION MODALITIES

Approved by:

Dr. A. Bruno Frazier, Advisor
School of Electrical and Computer Engineering
Georgia Institute of Technology

Dr. Ian Ferguson
School of Electrical and Computer Engineering
Georgia Institute of Technology

Dr. William Hunt
School of Electrical and Computer Engineering
Georgia Institute of Technology

Dr. Clifford Henderson
School of Chemical and Biomolecular Engineering
Georgia Institute of Technology

Dr. Anthony Yezzi
School of Electrical and Computer Engineering
Georgia Institute of Technology

Date Approved: December 21, 2005

This dissertation is dedicated to two fantastic women:

-my mother, for teaching me the value of education, and
her endless support and encouragement

and

-my wife, for her tolerance and patience with such an imperfect husband,
and her dedication to me and our children

I dearly love you both!

ACKNOWLEDGEMENTS

First, I would like to thank my advisor, Dr. A. Bruno Frazier, who has been the most influential person to me getting to this stage in my formal education. His guidance during my formative years as a graduate student at the University of Utah provided me a solid foundation upon which to build my research and other more scholarly abilities. By offering me a position in his laboratory at the Georgia Institute of Technology, he enabled me to continue my learning of knowledge, attributes and skills that will help me have a successful career. He is a very patient man and I am truly privileged to have had such a wonderful and proficient mentor.

I also thank my committee members, Dr. William Hunt, Dr. Anthony Yezzi, Dr. Ian Ferguson, and Dr. Clifford Henderson for their time, helpful comments, and support. They have been instrumental in seeing that this dissertation is accurate, appropriate and complete.

It is necessary for me to thank some of the administrative staff with whom I have had the pleasure to interact with. My deepest thanks go to Marilou Mycko for all her advice and significant efforts on my behalf. She has the fine quality of being firm in a friendly way. For me, she was truly an indispensable asset. Dr. David Hertling deserves many thanks for his advice that helped me successfully pass the Preliminary Exam. He is a kind man that I am grateful to have become acquainted with.

During my time here at Georgia Tech, I had the joy of getting to know some of my instructors very well. I thank Dr. Rob Butera for his uplifting comments and positive attitude. His door was always open and he has the great attribute of being more than willing to share his time with others. I express my sincere thanks to Gail Palmer for her endless encouragement, for becoming my friend, and for always having a smile. She is an affable, selfless and kindhearted person. To Dr. Thomas Gaylord, I wish to offer my

thank you for being such an outstanding example of kindness, hard work, excellence and dedication. I hope to one day possess such fine qualities as he appears to have mastered. I thank all of them for their willingness to take the time to help and teach me. They have furthered my knowledge and, more importantly, taught me how to be a better person.

I would also like to thank my fellow lab members for their friendship and help. We shared many great times and I will always have fond memories of our time together. The staff of the MiRC cleanroom deserves much praise for their efforts, especially Gary Spinner whom I tended to require the services of all too often.

Of course, I thank my family for their support, patience and encouragement. My mother is always honest with me and has always prodded me to pursue education, supporting me as needed along the way. My wife seems to love and respect me almost as much as I love and respect her and she sustains me in any prudent decision I may make. I am so grateful that she is the love of my life and has chosen to be my eternal companion. I thank my children for welcoming me home each night with enthusiastic and delightful hugs and for helping me unwind each day. They constantly remind me of what really matters. I thank my mother-in-law and father-in-law for allowing my family and I to learn and grow and for helping us when we make mistakes. Their love and support has provided me with the assurance that my family and I have a perpetual safety net.

Finally, I thank our Heavenly Father for giving us, His children, a wonderful world to explore and discover and for the mental and physical capacities to do so. He truly does love each one of us.

TABLE OF CONTENTS

LIST OF TABLES

LIST OF FIGURES

LIST OF SYMBOLS

a	particle radius
a_n	complex Mie coefficient
A	(channel) cross sectional area
b	channel breadth
b_n	complex Mie coefficient
C_{abs}	absorption cross section
C_{ext}	extinction cross section
C_{sca}	scattering cross section
d	(particle) diameter
d_h	hydrodynamic diameter
d_i	steric inversion diameter
D	mass diffusion coefficient
D_h	hydraulic diameter
D_n	logarithmic derivative of the Riccati-Bessel function, $\Psi_n(mx)$
E_{app}	applied electric field
E_{eff}	effective electric field
F_C	volumetric flow rate
H	theoretical plate height
H_D	diffusion factor
H_i	instrumental factor

H_n	nonequilibrium factor
H_p	polydispersity factor
H_r	relaxation factor
I	scattered light intensity
I_{par}	scattered light intensity parallel to polarization of incident light
I_{perp}	scattered light intensity perpendicular to polarization of incident light
I_T	scattered light intensity of transmitted light
I_U	scattered light intensity from unpolarized incident light
I_0	intensity of the incident light
J_x	diffusive flux of particles in the *x*-direction
k	mass distribution (i.e., partition) ratio *or* propagation constant
k_B	Boltzmann's constant
K	Mie extinction coefficient
l	channel length
L	optical path length
m	complex relative refractive index
n_{im}	imaginary refractive index
n_{med}	refractive index of the medium
n_{Re}	real refractive index
N	number of theoretical plates
N_{par}	number of particles per unit volume
P_{Wet}	wetted perimeter

r	distance from the particle at which scattered light is observed
R	retention ratio
R_c	(electrical) resistance of channel with cell
Re	Reynolds number
R_S	resolution
R_0	channel (electrical) resistance
S	Mie amplitude function
SU-8	a high contrast, epoxy-based photoresist
t	time
t_{inj}	time of sample injection
t_R	retention time
t_0	void time
T	temperature
u	characteristic (fluid) velocity
U	drift velocity
$\langle v \rangle$	average carrier fluid velocity
V	carrier fluid velocity
V_{app}	applied voltage
V_c	cell volume
V_{max}	maximum carrier fluid velocity
V_{par}	particle volume
V_R	retention volume

V_0	void volume
w	channel thickness/height
w_b	peak width
$w_{1/2}$	peak width at half-height
x	size parameter
α	separation factor
γ	steric transition factor
ΔR	change in channel (electrical) resistance
ε_r	relative permittivity
ε_0	permittivity of vacuum
ζ	zeta potential
η	dynamic (fluid) viscosity
θ	angle of observation measured from forward to scattered direction
λ	retention parameter
λ_0	incident wavelength
μ	microfabricated
μ_e	electrophoretic mobility
ξ	a Riccati-Bessel function
π_n	Mie recurrence relation
ρ	fluid density *or* electrical resistivity
ρ_{par}	particle concentration

σ	standard deviation
τ_n	Mie recurrence relation
χ	factor in Riccati-Bessel function, ξ
ψ	angle measured from scattering direction to the electric dipole
Ψ	a Riccati-Bessel function

LIST OF ABBREVIATIONS

AC	alternating current
AcFFF	acoustic field-flow fractionation
Au	gold
Cr	chromium
DC	direct current
DEF-FFF	dielectrophoretic field-flow fractionation
DI	deionized
DNA	deoxyribonucleic acid
ElFFF	electrical field-flow fractionation
FlFFF	flow field-flow fractionation
GFFF	gravitational field-flow fractionation
GLC	gas-liquid chromatography
GSC	gas-solid chromatography
HF	hydrofluoric acid
ITO	indium tin oxide
KOH	potassium hydroxide
LLC	liquid-liquid chromatography
LSC	liquid-solid chromatography
MEMS	microelectromechanical systems
MgFFF	magnetic field-flow fractionation
NaCl	sodium chloride

PBS	phosphate buffered saline
Pt	platinum
SdFFF	sedimentation field-flow fractionation
ThFFF	thermal field-flow fractionation
Ti	titanium
VHS	video home system

SUMMARY

The objective of this research is to develop efficient, non-invasive separation systems with complementary on-column electrical and optical detection modalities for use with various biological and non-biological substances. In this work, the development of three sizes of microfabricated electrical field-flow fractionation (μ-ElFFF) systems, with complimentary on-column detection systems, is presented and the data obtained from the two types of detection systems is compared.

The first detection system is the electrical conductance measurement (ECM) system. The ECM system is on-chip and can be used to detect the presence of a wide variety of analytes by measuring changes in the current flow across the channel as the analytes pass the detector. The conductivity and electrical permittivity of the sample medium (i.e., carrier fluid) also affect the current flow across the channel. The second detection system is the resonance light scattering (RLS) detection system. The RLS detection system is used for off-chip, on-column particle detection and is also useful for general flow visualization in micro channels.

This work presents the design of the μ-ElFFF systems and a description of the fabrication processes for each of the current μ-ElFFF systems. The integration of the ECM and RLS detection systems is reported and the method of characterization of the μ-ElFFF systems and the on-column detection systems is outlined and discussed. Also presented is the approach to performing a quantitative correlation of the two detection systems.

Each device was fabricated from glass substrates to enable RLS detection. For the electrode materials, platinum and indium tin oxide (a transparent conductor) were used. Separations were performed using RLS Particles^{TM} (gold nanospheres), polystyrene beads, bovine chromaffin cells and human breast cancer cells, with sizes ranging from 40 nm to 9.91 μm. Sample volumes ranged from 0.05-3.0 μL, with

concentrations ranging from 7.37 x 10^{-13} M to 1.18 x 10^{-10} M. Analysis times ranged from 35 seconds to 40 minutes, depending on the channel size and desired resolution. Distinct peaks were obtained for different sized particles in a polydisperse sample bolus. The correlation between the optical signals and the electrical measurements was quantified and showed good agreement with theory.

CHAPTER 1

INTRODUCTION AND BACKGROUND

1.1 Objective

The objective of this research was to develop efficient, non-invasive separation systems for various biological and non-biological substances. One of the major technological pushes in modern bioanalysis instrumentation development is the realization of efficient, miniaturized bioanalysis systems. In this work, three sizes of microfabricated electrical field-flow fractionation (μ-ElFFF) systems, with complementary on-column electrical and optical detection modalities, were fabricated to achieve this objective.

1.2 Scope and Novelty of Work

In this work, microfabrication technologies were used to fabricate the μ-ElFFF systems, yielding devices that have smaller system volumes, require smaller sample volumes and have shorter run times than their macro-scale counterparts. Direct, on-column detection within the miniaturized separation device was performed, improving resolution, decreasing band broadening, lowering plate height, and shortening overall analysis time. On-column optical and on-chip electrical detection systems were used and the information obtained from these detection systems was shown to be useful for determining specific electrical and physical characteristics of a sample.

The μ-ElFFF systems were fabricated from glass substrates rather than the traditional silicon substrates. Silicon substrates prohibit the use of resonance light scattering (RLS) detection; however, glass is transparent, allowing particles in the microchannel to be illuminated. Upon illumination, the particles scatter light that can be detected at low magnification (e.g., 100X). The ability to use RLS technology was not possible with earlier systems.

Field-flow fractionation (FFF) technology is capable of fractionating (or separating) a wide variety of materials and is capable of hundreds of consecutive analysis runs using a single system. A highly promising sub-technique, particularly for the analysis of biological / biochemical materials, is electrical field-flow fractionation (ElFFF). However, one of the major challenges that is presented with the use of this sub-technique is the occurrence of electrolysis at the surface of the main electrodes when the applied voltage, V_{app}, is too high for the flow rate. By reducing the channel thickness, the upper limits on the applied field, E_{app}, that electrolysis imposes can be increased. Therefore, microfabricated ElFFF (μ-ElFFF) channels with channel heights of 5 μm were designed, fabricated and tested. This decrease in channel height represents more than a 5-fold reduction in channel height from previously published works.

Complimentary electrical and optical detection systems (on-chip and on-column, respectively) were designed, fabricated and characterized. While μ-ElFFF systems with on-chip electrical detectors or off-column optical detection systems have been reported prior to this work, the simultaneous acquisition of on-chip electrical and on-column optical signals from a μ-ElFFF system is novel to this work. Additionally, the data from the two detection systems was compared and a quantitative correlation was performed. The results of the analysis verified that the detection systems could also be used independent of each other.

1.3 Survey/Description of Separation Systems

Separation systems are used to separate components found in emulsions, mixtures or colloidal suspensions. Therefore, all separation systems must have a way to differentially distinguish and maneuver one or more constituents in the sample. Separation systems may be thermally, mechanically, electrically, magnetically, acoustically or chemically driven, with more advanced systems often requiring the use of a particular combination of methods [1-6]. Systems have been developed to separate

many types and forms (i.e., gaseous, liquid, or solid) of constituents from samples, either natural (organic or inorganic) or synthetic with sizes ranging from the molecular level (a few angstroms) to tens of microns [7-15]. The size of the system is determined by the method of separation, the sample size and, in some cases, the size of the constituents to be separated.

Many of the separation systems used today were developed as macrosystems and remain macro-sized. However, with the development of microfabrication technologies, a large number of systems have been miniaturized [16-23]. Therefore, an overview of existing macro- and micro-sized separation systems is beneficial to understanding where separation science is today and where the μ-ElFFF system developed in this work fits in.

Macrosystems

Generally, macrosystems are defined as systems that do not require conventional microfabrication technologies for their manufacture. Some of the major commercially available macroscale separation systems include: distillation units, solute removal/recovery systems, centrifuges, crystallization systems and fume/dust extraction systems. Other macrosystems that consumers are more familiar with include ion-exchange units (for water purification), adsorption systems (e.g., cigarette filters) and membrane-based separation systems (e.g., reverse osmosis water purification systems, vacuum cleaner bags, tea bags). There are also many types of chromatography systems and various field-induced separation systems that are routinely used by scientists, especially in the biotechnology sector.

Microsystems

While it is necessary for many separation systems (e.g., wastewater treatment plants) to handle large amounts of sample, there are significant benefits that can be realized by miniaturizing others. By using microfabrication technologies, not only can

the physical size of the system be reduced, but sample volume, analysis time and even cost may also be reduced. A cost savings would be especially important to the biotechnology industry as the U.S. biotech separations market, according to a recent report by Business Communications Company, Inc., is expected to reach $3.6 billion by 2008 [24].

Since chromatography systems dominate the biotechnology sector, it is not surprising that one of the first separation systems to be miniaturized was a gas chromatography system [16, 17]. Liquid-based chromatography systems have also been microfabricated [18, 19, 25]. Furthermore, field-induced separation systems, such as FFF and electrophoresis, have yielded significant benefits through their miniaturization [20-23]. Where high throughput is desired, separation methods that do not require large amounts of sample can significantly benefit from miniaturization because multiple systems can be fabricated on one chip [26-28]. This attribute, when combined with the faster analysis times microsystems provide, is an important motivation for miniaturization.

1.4 Comparison of Microfabricated Separation Systems

Electrical field-flow fractionation is the separation method that was investigated for this work because of the many advantages it provides over other methods. Of course, no one method is the best for every application; however, with respect to separations of constituents suspended in a liquid, microfabricated separation systems based on ElFFF provide a broader range of abilities than other types of systems.

Microfabricated Filtration Systems

One of the more simple types of separation methods is that of filtration. Stemme *et al.* developed the first microfabricated filtration systems in 1988 [29]. In these systems, membranes with holes in them functioned as the filter. The membranes were prone to breakage, and like most subsequently developed filtration systems, were prone

to clogging. Recently, magnetically-based filtration systems have been developed [30]. These systems have the advantage over traditional filtration systems in that they do not clog as easily because the spacing of the pillars can be much larger than the magnetic components to be separated. Nevertheless, since they are only useful for magnetically susceptible materials or magnetically tagged components, the range of sample types that can be separated is low compared to μ-ElFFF systems. Furthermore, filtration systems separate sample constituents according to their size, and are therefore not as selective as μ-ElFFF, in which separations are based on both size and specific electrical properties of the components to be separated.

Microfabricated Electrophoretic Systems

In the biotechnology sector, several types of electrophoresis-based separation systems for bio-molecules (e.g., DNA, proteins) have been miniaturized since 1990 when the microfabricated version of a capillary electrophoresis device was first realized [20-22, 31-38]. These microfabricated systems have been revolutionary to the field of biotech separation science. The small volume requirements (picoliters), high fields, short separation channel lengths, short analysis times (seconds) and the ability to perform multiple simultaneous separations enables extremely high throughput and provides higher resolution than the macroscale counterparts. The nature of the separation, however, lessens the ability to make these systems portable because of the high voltages required (kilovolts). In contrast, separations in μ-ElFFF systems require less than 2 "AA" batteries (i.e., 3 volts), and could be made portable with relative ease. Additionally, microfabricated electrophoretic systems are often single-use devices, whereas one μ-ElFFF channel can be used for hundreds of separations.

Microfabricated Chromatographic Systems

Chromatographic systems have a much broader utility than electrophoretic systems, which is one reason why they have such a dominant role in biotechnology. While there are many types of chromatographic systems, they can be separated into two groups: gas chromatography and liquid chromatography.

As mentioned previously, one of the first microfabricated separation systems was a gas chromatography system [16, 17]. However, according to the report by Business Communications Company, Inc., liquid chromatography systems represented nearly 47% of the total market of biotechnology separation systems in 2003 [24]. The importance and usefulness of chromatographic systems has led many researchers to find ways to make them even more useful and powerful through microfabrication technology.

Liquid chromatography systems are generally more difficult to produce in a micro format than gas chromatography systems. This is due to the fact that while submicron support particles are available, it is difficult to pack uniform, stable beds in a microsystem and to retain the particles in the column [39]. The stationary phase in many microfabricated gas chromatographs can be deposited uniformly and at a precise thickness [40-42].

Separations in basic chromatographic systems occur because of the specific interactions of the sample constituents with the stationary phase. Because of this, they are subject to fowling and, like filtration systems, clogging. Conversely, in μ-ElFFF systems, separations are based on the mobility of the constituents, which is a function of their size and electrical properties. There is no packing material that can be fowled and clogging is highly improbable.

1.5 Field-Flow Fractionation

Field-flow fractionation was first described by J. C. Giddings in 1966 [43]. The name of this technique comes from the fact that separation in these systems is achieved

because of two factors: the field and the flow. In FFF systems, the field, applied perpendicular to the flow, works in conjunction with the flow properties of the fluid in the channels to effect a fractionation of sample components. The sample components become both spatially separated, or fractionated, as they pass through the channel and temporally separated upon their exit from the channel, eluting at different times.

General FFF Theory

While the type of field varies from one subtype to another, all types share a parabolic velocity profile, characteristic of laminar flow. Channels of FFF systems are thin, with breadth, *b*, to thickness, *w*, ratios (*b*/*w*) of approximately 100 or higher. In these thin channels (i.e., with channel thicknesses less than about 250 μm), laminar flow is established, creating the parabolic flow velocity profile mentioned above. This profile is essential for FFF and forms the basis for both the spatial separation of the sample components and their temporal separation as they exit the channel. As the sample components are forced to different heights in the channel due to the applied field, they flow at different velocities due to the flow velocity profile as shown in Figure 1.1.

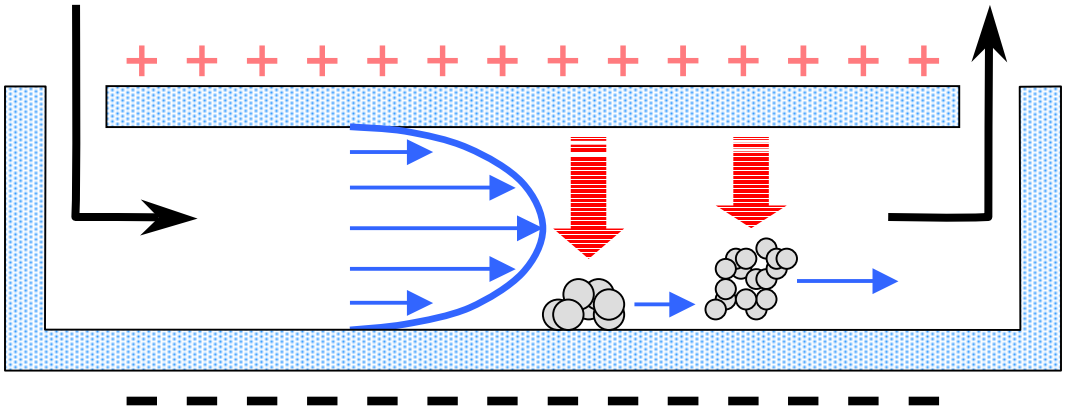

Figure 1.1: Side view schematic of a μ-ElFFF channel showing the direction of flow, the flow velocity profile (blue arrows) and the electric field (red arrows).

A key aspect that distinguishes FFF from all other techniques is its ability to separate materials over the entire colloidal size range (1-1,000 nm) with high resolution. Other distinctive attributes of FFF are that there is no stationary phase for the sample components to interact with and that the field, which enables the separation, is applied perpendicular to the flow (Figure 1.1). Because of the many types of fields, channel structures, operating modes and experimental conditions that can be used, FFF is, perhaps, the most versatile family of separation methods available.

While the versatility and adaptability of FFF are major strengths to the technique, it could be argued that they have hindered the rapid development and wide spread use of FFF. The basic principles behind FFF are relatively simple, but the numerous variations on the overall theme make it seem overwhelming to most researchers that are not well versed in FFF. As a result, a relatively small number of groups have worked in this area, and only a small fraction of subtypes have become commercially available.

Subtypes of Field-Flow Fractionation Systems

All FFF systems are useful for separating sample components according to size, but the type of field used to accomplish the task varies from one subtype to another. As a result, the many subtypes of FFF devices are classified by the type of applied field they employ to effect the fractionation of the sample components, not the effect they have on the sample components. Some of the more common subtypes are thermal, sedimentation, and flow FFF [44-51]. Other types that have been developed use acoustic, magnetic, gravitational or dielectrophoretic fields [44, 52-56]. First described in 1972, electrical FFF was one of the first subtypes developed and is the subtype that was used for this work [57].

Electrical Field-Flow Fractionation

As previously mentioned, the FFF subtype used for this work was an electrical field-flow fractionation system (ElFFF). In these systems, the top and bottom walls of the channel serve as the driving electrodes that create an electric field across the channel. Sample components are surrounded by ions in the carrier solution and a potential (the electrokinetic or zeta potential, ζ, is established between ions near the surface of the particle and the bulk of the carrier fluid. When the particle enters the electric field, the electrostatic force causes the particle to move toward the accumulation wall at a rate proportional to the electrophoretic mobility, μ, of the particle. For a given carrier fluid, the size of the sample components, coupled with their zeta potential, determines their electrophoretic mobility. It is the electrophoretic mobility that ultimately determines the degree to which the components are retained in the channel.

The ElFFF subtype is extremely versatile and separations of polymer beads, metal nanospheres and several types of biological components have been effectively demonstrated.

Thermal Field-Flow Fractionation

Thermal field-flow fractionation (ThFFF) was the first subtype of FFF to be developed. In this method, the thermal field is established by heating one wall of the channel while maintaining the opposite wall at a much lower temperature. Sample components flowing through the channel diffuse toward the cold wall via thermal diffusion. The components that are more susceptible to the thermal field (i.e., have higher thermal diffusion coefficients) are more strongly forced toward the cold wall than those that have lower thermal diffusion coefficients.

Typically, ThFFF has been used for separation and analysis of polymers. In addition to determination of particle diameter, with ThFFF, the determination of

molecular weight, the thermal diffusion coefficient, physicochemical and surface properties is possible.

Sedimentation Field-Flow Fractionation

Sedimentation field-flow fractionation (SdFFF) is one of the few subtypes that have become commercially available. It is a useful method for separating colloidal particles, ranging from 100 nm-100 μm in diameter, that have a different density than the carrier solution. In SdFFF, the channel is rotated at a high velocity, subjecting the sample components to a centrifugal force. This force is equal to the product of the component's effective mass and the centrifugal acceleration.

Since the effective mass of the analyte is a function of its mass and its relative density with respect to the carrier solution, SdFFF systems can be used to determine particle size or density. One of the major benefits of SdFFF systems is that the retention increases with the third power of the particle diameter, providing a larger size-based selectivity than other subtypes of FFF.

Flow Field-Flow Fractionation

The field employed by flow field-flow fractionation (FlFFF) systems is a crossflow of a second stream of carrier solution that passes through the permeable walls of the channel. Each wall is composed of a frit that is covered with a semi-permeable membrane that allows the carrier fluid to pass through, but prevents the sample from exiting the channel as the second stream of carrier solution is driven across the channel. The second stream passes through the walls in a perpendicular direction to the axial flowstream (characteristic of FFF systems), forcing all sample components against the accumulation wall. The center of mass for larger particles is higher in the channel than that of the smaller particles and because of the parabolic velocity profile, they travel at a faster rate.

For the most commonly used channel dimensions, the size range of sample components that can be fractionated in a FlFFF system is from 2 nm – 100 μm. This represents the largest size range of any FFF subtype. This characteristic is important since FlFFF is the only subtype of FFF that fractionates sample components exclusively by size.

Acoustic Field-Flow Fractionation

The acoustic FFF (AcFFF) subtype is the most recent to be explored and developed. These systems are rather complex to design and fabricate when compared to other FFF subtypes. In AcFFF systems, one of the channel walls functions as an acoustic transducer (e.g., lithium niobate). The transducer must be carefully chosen because it is the properties of the transducer that determine the fundamental resonant frequency and the thickness the opposing wall needs to be for a given material. The channel thickness is precisely defined so that a standing pressure wave across the channel is maintained. As samples pass through the channel, the pressure wave forces them to distinct positions within the channel, corresponding to distinct velocities in the laminar flow, thereby effecting the separation.

The AcFFF systems separate sample components not only according to size, but also according to the components' density and compressibility. No other FFF subtype can separate components by their density and compressibility. This is an ability unique to the AcFFF subtype.

Magnetic Field-Flow Fractionation

Magnetic field-flow fractionation (MgFFF) has not been well developed since it is only useful for sample components that have a magnetic susceptibility. Shunk *et al.* fabricated a channel using a conventional parallel-plate design with the bottom wall resting on the core of an electromagnet. In their configuration, a gradient in the magnetic

field was established across the channel. Retention in these channels is proportional to the square of the magnetic gradient.

Typical particles separated in MgFFF devices are metal, metal alloys or particles that are complexed with such particles, since in these systems, particles are separated according to their relative magnetic permeabilities.

Gravitational Field-Flow Fractionation

Like SdFFF, gravitational field-flow fractionation (GFFF) systems separate sample components based on their effective mass. These systems are quite simple since they only require a channel (open or closed), fluid flow and gravity. In contrast to SdFFF, the force on the sample components in GFFF is proportional to the acceleration due to gravity instead of a centrifugal acceleration.

These systems are useful for larger analytes and analytes with high effective masses because of the relatively low acceleration due to gravity. This also means that the flow rates and the resulting analysis times are usually lower than a similar separation in an SdFFF system.

Dielectrophoretic Field-Flow Fractionation

Dielectrophoretic (DEP) forces on sample components occur when a non-uniform electric field interacts with field-induced electrical polarization in the components. Dielectrophoretic field-flow fractionation (DEP-FFF) systems typically use interdigitated electrodes on the bottom wall to generate the DEP forces. In this arrangement, different sample components are levitated to different equilibrium heights in the channel, determined by the DEP (upward) and sedimentation (downward) forces.

This technique has been shown to be effective for separating components based on their dielectric properties and densities. Wang *et al.* demonstrated the usefulness of this FFF subtype for separating live cells. The DEP-FFF subtype could become a

significant tool in biotechnology since labeling is not necessary, the cells remain viable and DEP-FFF exploits physical characteristics that play little or no role in other cell separation/analysis methods.

1.6 Microfabricated Electrical Field-Flow Fractionation Systems

Gale *et al.* developed the first μ-ElFFF in 1997, about 25 years after the first description of ElFFF [23, 58]. Miniaturizing ElFFF systems yielded many benefits including shorter analysis times, higher resolution, lower power requirements and reduced sample/carrier volumes [59, 60].

These systems can be used for fractionating many types of samples. Some of the different types of particles separated in μ-ElFFF systems include polystyrene beads, gold nanospheres, whole blood components, and protein coated particles [58, 61, 62]. They are capable of fractionating many other types of materials and therefore, could have applications in environmental monitoring, developing drug delivery systems (e.g., liposome or micelle characterization), emulsion characterization, cell separation, sorting DNA fragments, or further research on zeta potentials. Their small size and low sample volume requirements make them appealing to benchtop research and analysis. These factors, combined with the low power requirements of μ-ElFFF systems, would make them ideal candidates for creating a portable system that could be used for on-site clinical or environmental science applications.

1.7 Detection Methods for Microsystems

Laser-induced fluorescence detection, UV-VIS absorbance, AC conductometric detection, mass spectrometry, chemiresistors, and simple microscopy are some of the detection methods that have been used in microsystems [19, 21, 35, 41, 63-69].

Off-Chip Detection

Most often, detection in microsystems is performed off-chip. This is logical because the detection systems are already fabricated (i.e., they do not need to be designed into the microsystem) and researchers are already familiar with the detection instruments and the associated protocol. Examples of off-chip detection methods (from those mentioned above) are the laser-induced fluorescence detection, UV-VIS absorbance, and mass spectrometry.

Laser-Induced Fluorescence Detection

Laser-induced fluorescence detection is a commonly used technique for detecting biological components. In this method, the analytes are first labeled with fluorescein molecules. Next, a UV laser is focused on a small volume of the sample to excite the fluorescein molecules, and the fluorescent light can be detected by using a microscope and a photomultiplier tube.

UV-VIS Absorbance

For detection of samples using UV-VIS absorbance, the light from the source may be directed to the microchannel via an optical fiber. The light can either pass through the channel to a fiber connected to the detector or a reflector may be built into the microchannel to direct the light to another fiber on the same side that leads to the detector. The detector measures absorbance and can be used to determine the type of sample that is passing through that region of the microchannel.

Mass Spectrometry

Mass spectrometry is a technique that is used for detecting samples after they have passed through the microsystem. The samples can be introduced into the mass spectrometer in liquid or gaseous form via a connection to the output of the

microchannel. If a sample is contained in a liquid, it is vaporized before passing through to the detector of the spectrometer.

On-Chip Detection

Performing detection on-chip can increase the complexity of the microsystem's fabrication, but doing so provides many benefits for separation systems. Some of the benefits that can be realized include an increase in resolution, faster analysis times and smaller overall system size. Additionally, by performing detection on-chip, it is possible to direct samples to other devices on the same chip that can further manipulate, collect or analyze the sample components. Some methods of on-chip detection that have been demonstrated include AC conductometric detection and chemiresistors.

AC conductometric detection

AC conductometric detection can be a relatively easy method to integrate if the microsystem requires metal deposition. For this type of detection, an AC electric field is established between two or more conductive electrodes that are placed in the path of the sample components. As the samples pass the electrodes, there is a measurable change in the current flow between the detectors. Once the system has been calibrated, the magnitude of the current change can be used to identify the concentration of the sample or its composition assuming one or the other is known.

Chemiresistors

Chemiresistors are materials that, upon adsorbing the sample components, experience a change in resistivity. This change is measured and indicates the presence of the sample and the concentration can be determined. The variety of samples that can be detected with a given chemiresistive material is limited since the sample must be adsorbed. It is common for chemiresistors to not be specific (i.e., they adsorb more than

one type of sample constituents). As a result, a second type of detector may be required to complement the chemiresistor.

1.8 Resonance Light Scattering

In this work, an integrated, on-chip electrical detector will be correlated with the measurements from an on-column resonance light scattering (RLS) detection system. The use of RLS detection with the μ-ElFFF system was first demonstrated in 2001 and represents the first use of RLS detection with a microsystem [61].

Overview

Resonance light scattering detection can be used for a large range of particle sizes. In this method, the sample is illuminated by white light that is directed to the microdevice from the lamp via an optical fiber. As the light passes through the microchannel, the sample components scatter light at a distinct wavelengths based on their composition and size. For effective implementation of this technique, the incident light must be directed through the microdevice at an angle so that the less intense scattered light can be seen through a microscope objective perpendicular to the channel.

Advantages of Resonance Light Scattering Detection

The costs associated with implementation of RLS detection are minimal when compared to other detection methods (e.g., mass spectrometry). The two main components required for off-chip RLS detection are a light source and a compound microscope—two apparatuses that most laboratories already have. The intensity of the scattered light from particles with diameters of a few nanometers can be very high, enabling visualization of individual particles. Furthermore, constant monitoring of the sample components can be performed with RLS, eliminating the photo-bleaching effect seen in fluorescence detection methods. To facilitate detection of certain biological samples, functionalized metal nanospheres can be easily attached, increasing the intensity

of the scattered light. In addition, the sample components can scatter light at distinct wavelengths according to composition and size. This property can be exploited to not only detect the presence of the sample, but to identify the individual components. Finally, RLS is easy to use in conjunction with other methods, as in this work, to enhance sample detection and analysis.

1.9 Specific Aims of this Work

There are four specific aims that have been identified to accomplish the objective of this research. These aims are

1. To design and fabricate a glass-based μ-ElFFF system for optical and electrical detection of biological and non-biological samples,
2. To integrate resonance light scattering detection with the μ-ElFFF system,
3. To characterize the μ-ElFFF system, and
4. To determine a quantitative correlation of optical and electrical signals.

The accomplishment of these tasks has resulted in the development of efficient, non-invasive separation systems with complementary on-column electrical and optical detection modalities for use with various biological and non-biological substances.

Specific Aim #1: Design and Fabricate a Glass-based μ-ElFFF System for Optical and Electrical Detection of Biological and Non-biological Samples

Microfabricated ElFFF systems capable of on-chip electrical detection have been previously developed, but optical (RLS) detection was not possible in the systems. In order to accomplish the task of integrating RLS particle detection with existing μ-ElFFF technologies, it was necessary to make material and design changes to μ-ElFFF devices that were previously developed. Therefore, a new design for the μ-ElFFF system was

generated that includes features necessary to perform RLS detection and on-chip electrical detection, and features that make the detection electrodes more robust and less likely to fail.

Specific Aim #2: Integrate Resonance Light Scattering Detection with the μ-ElFFF System

To accomplish the second aim of integrating resonant light scattering particle detection with the μ-ElFFF system, materials that are less conventional to MEMS processing technologies were required. As a result, fabrication necessitated the modification of several standard processes and the development of new processes.

Specific Aim #3: Characterize the μ-ElFFF System

The third aim was to perform separations of biological samples and RLS particles to characterize each μ-ElFFF system. Three sizes of channels were fabricated for various types of sample components ranging from molecular chains (e.g., DNA) to whole cells (e.g., bovine chromaffin cells). The use of gold RLS particles facilitated the characterization of the μ-ElFFF systems.

Specific Aim #4: Determine a Quantitative Correlation of Optical and Electrical Signals

Finally, the fourth aim was to determine a quantitative correlation of the optical and electrical signals. While on-chip electrical detection has been characterized in previous μ-ElFFF systems, there is no previously published data for on-column optical detection in these systems.

1.10 Outline of Chapters

The theory of both FFF and RLS will be expanded upon in Chapter 2. Chapter 3 describes the design and fabrication of the μ-ElFFF systems and details of the processes

used will be provided. An overview of the basic operation of the entire setup, the details regarding the characterization experiments and the results of each experiment will be presented in Chapter 4, followed by a description of the components, operation and parameters of both the electrical and RLS detection systems in Chapter 5. The methods used to determine the quantitative correlation of the electrical and optical measurements followed by a demonstration of the correlation will comprise Chapter 6. In Chapter 7, the final chapter, the novel contributions of this work will be highlighted and some possible directions for future work based on the results of this research will be presented and discussed.

CHAPTER 2

THEORY

2.1 Introduction To Chromatographic Systems

Between the years 1902-1906, a Russian botanist, Tswett, invented and developed the chromatographic method while working on the isolation of chlorophyll and other plant pigments [70, 71]. Although Tswett had a profound understanding of the physicochemical phenomena involved in chromatography, he never described chromatographic separations in mathematical terms [72]. Perhaps the lack of a mathematical model, coupled with skepticism from other researchers, was the main reason why his work was not fully accepted or appreciated until 1931, when Kuhn and Lederer rediscovered his work and used it to successfully separate carotenes and xanthophylls [73-75]. Even after the work of Kuhn and Lederer, the technique was used only occasionally. Then, in 1940, a mathematical model was developed by Wilson and in 1941, a famous paper by Martin and Synge provided a theoretical framework for the basic chromatographic process [76, 77]. While the vast majority of the early work was focused on liquid chromatography, over the next several years, other types of chromatography were developed, including gas-solid and gas-liquid subtypes [78, 79]. Chromatography, in all its forms, has since become one of the world's most widely used separation and purification techniques.

Chromatographic processes are separation methods that belong to two main categories: adsorption chromatography and partition chromatography. Adsorption chromatography depends on successive adsorptions and desorptions of components in a liquid or gas mixture to a solid adsorbent. The less strongly adsorbed materials travel faster than the strongly adsorbed materials, becoming separated as they migrate through the system. In partition chromatography, a liquid or gas mixture interacts with a stationary liquid phase instead of a solid adsorbent. This method is based on the partition

principle that states that if substance X is soluble in and mixed with two immiscible solvents, A and B, it will partition itself between the two solvent in a constant ratio (termed the partition ratio) as long as neither solvent is saturated. This is shown by the following equation as

$$\frac{\text{concentration of X in A}}{\text{concentration of X in B}} = \text{constant}. \tag{2.1}$$

For components in a sample that have different constants, repeated distributions of each component between the two phases will cause some to move faster than others, thereby enabling a separation of the components.

The main element in chromatography systems is the tube, or column, that contains the packing, adsorbent and/or liquid (held as a thin film on a porous solid support) stationary phase through which the liquid or gas mobile phase (containing the sample to be analyzed) passes. This design enables the two phases to move relative to each other, which is necessary for a repetition of the distribution or adsorption of a solute component between the two phases.

The two types of mobile phases—liquid and gas—combined with the two types of stationary phases—liquid and solid—yields four basic types of chromatographic systems, appropriately identified by their respective mobile and stationary phases. These four types are liquid-solid chromatography (LSC), liquid-liquid chromatography (LLC), gas-solid chromatography (GSC), and gas-liquid chromatography (GLC).

2.2 Comparison of ElFFF to Chromatographic Systems

Like chromatographic techniques, electrical field-flow fractionation (ElFFF) is a flow-based separation methodology. In both types of systems, a finite volume of a sample mixture is injected into the flowing mobile phase/carrier fluid that passes through the column/channel. As the sample components travel through, they become separated into distinct bands and elute at different times based on their interaction with the stationary phase/field, making the systems useful as analytical tools.

Field-flow fractionation was developed several decades after chromatography, yet because of their similarities, much of the terminology, characterization parameters, and theory are the same or closely related. Four important characterization parameters common to both ElFFF and chromatographic systems are

1. Retention time/volume
2. Retention ratio
3. Plate height/number of theoretical plates
4. Resolution

Calculation of these fundamental parameters is important for characterizing an individual system with respect to sample compositions and for being able to compare the separation performance of one system with another.

Retention Time/Volume

In both ElFFF and many types of chromatographic systems, a device near the output may be used to detect the presence of sample components after the separation has occurred. The result is a plot of the detector's response (usually proportional to the flux of sample components) as a function of time or volume (Figure 2.1). The retention time of a sample component, t_R, is defined as the time from sample injection to the time of the peak resulting from the detection of the component. The retention volume is the amount of liquid or gas that passes the detector between t=0 and $t = t_R$. If the flow rate, F_C, is constant, then the retention volume, V_R, is

$$V_R = t_R F_C . \tag{2.2}$$

The amount of time between sample injection and the peak of the detector's response for sample components that are not retained in the column/channel is termed the

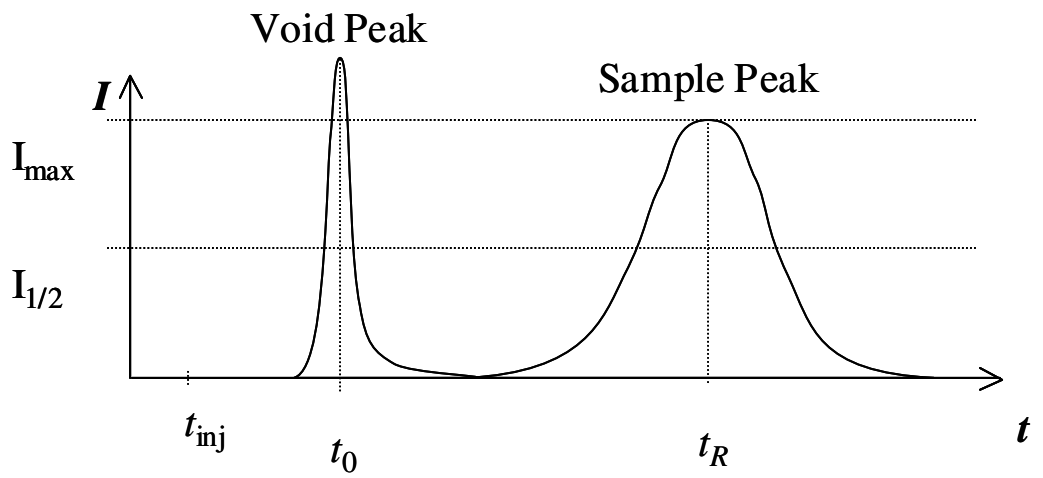

Figure 2.1: Depiction of a fractogram of measured current versus time. Time of injection, t_{inj}, void time, t_0, and the retention time, t_R, are shown.

void time, t_0, and the corresponding volume can be calculated using Equation 2.2 by substituting t_0 for t_R. The resulting volume is called the void volume, V_0. Usually, it is more common to calculate the retention time with respect to the void time because the resulting value will be more accurate for characterizing the system since it eliminates any variability there may be in the injection procedure.

Retention Ratio

The retention ratio, R, also known as the retardation factor, represents the ratio of the distance traveled by a retained sample component to that traveled by an unretained component. That is,

$$R = \frac{t_0}{t_r}. \tag{2.3}$$

In ElFFF, the value of R ranges from 0 to 1, and in certain types of FFF (e.g. hyperlayer FFF) its value can exceed 1. This parameter is relatively easy to calculate and can be used to estimate certain physicochemical properties of analytes.

Plate Height/Number of Theoretical Plates

Similar to the way FFF has drawn upon chromatographic terms and techniques, chromatography separations have often been compared to distillation processes. In 1941, Martin and Synge applied the plate theory concept, used for distillation processes, to separations achieved via chromatographic methods [80]. They defined a plate as "that region in which the average concentration of the solute in the two phases is the same as that which would be obtained if the solute were actually in equilibrium with the two phases in the region". In FFF and chromatographic systems, it is useful to know the height equivalent of the theoretical plates, or the plate height, H. This value is the physical length of the plate region, as defined above, as it relates to the column/channel. By dividing the total length, *l*, of the column/channel by the plate height, the number of theoretical plates, N, is obtained, as shown in the following equation:

$$N = \frac{l}{H} \tag{2.4}$$

For each type of separation system, the number of plates is a relative measure of its efficiency at separating the components in a sample mixture. In an expression to calculate resolution, developed by J. H. Purnell and used for high-performance liquid chromatography, the square root of the number of plates is proportional to the resolution [81]. Therefore, systems with high resolutions have low plate heights.

Resolution

The resolution, R_S, of chromatographic or FFF systems is the degree to which components in a sample mixture can be separated such that a plot of the detector response will show more than one peak. It is usually defined mathematically as

$$R_S = \frac{2(t_{R_2} - t_{R_1})}{w_{b_1} + w_{b_2}}, \tag{2.5}$$

where the numerator contains the difference between the retention times of two analytes and the denominator is the sum of the two peak widths, w_b, as measured at the base of each peak. Sometimes the term w_b is replaced by 4σ, where σ is the standard deviation of the peak, in which case

$$R_S = \frac{2(t_{R_2} - t_{R_1})}{4(\sigma_1 + \sigma_2)} = \frac{(t_{R_2} - t_{R_1})}{2(\sigma_1 + \sigma_2)}. \tag{2.6}$$

As previously mentioned, Purnell related the number of theoretical plates to resolution, as shown by

$$R_S = \frac{1}{4}\left(\frac{\alpha - 1}{\alpha}\right)\left(\frac{k}{1+k}\right)\sqrt{N}\,, \tag{2.7}$$

where the separation factor, α, a comparison of the net retention times of two peaks is

$$\alpha = \frac{t_{R_2} - t_0}{t_{R_1} - t_0}, \tag{2.8}$$

and *k* is the partition ratio as defined by the constant in Equation 2.1. The partition ratio is also known by its recommended term, the mass distribution ratio [82].

While each of these four important parameters are common to both chromatographic and ElFFF systems, there are some major differences that will be discussed in the next sections.

2.3 ElFFF Theory

In contrast to chromatographic systems, separations in common FFF systems (e.g. ElFFF), are not based on the interactions of the sample components with a stationary phase. Instead, the separations occur due to the position of the analytes in the channel's flow pattern, as determined by the degree to which they are affected by the applied field, hence the name field-flow fractionation [83].

Laminar Flow

For separations to occur in ElFFF systems, it is essential to have laminar flow within the channel. Laminar flow is characterized by a near-parabolic flow profile, and is usually present when the Reynolds number is below about 1500 [84, 85]. The transition from laminar flow to turbulent flow occurs somewhere between the Reynolds number range of 1500 to 2500, with higher values characterized by turbulent flow. The Reynolds number, *Re*, is easily calculated as

$$Re = \frac{\rho D_h u}{\eta} \tag{2.9}$$

where ρ is the density of the fluid, u is the characteristic velocity in the channel, η is the dynamic viscosity of the fluid, and D_h is the hydraulic diameter, given by

$$D_h = \frac{4 \times \text{Cross Sectional Area}}{\text{Wetted Perimeter}} = \frac{4A}{P_{Wet}}. \tag{2.10}$$

The cross sectional area, A, refers to the area of the channel through which the flow passes and the wetted perimeter, P_{Wet}, is the perimeter of the channel that is in direct contact with the flowing fluid.

Electric Field

Another factor required for separations in ElFFF channels is an electric field applied perpendicular to the direction of fluid flow. The applied electric field, E_{app}, is dependent upon the applied voltage, V_{app}, and the channel thickness, w, or

$$E_{app} = \frac{V_{app}}{w}. \tag{2.11}$$

However, caution must be exercised because the effective electric field, E_{eff}, is often lower than 1% of the applied electric field [12, 62, 86]. There are two main reasons why the effective field is much less than the applied field. First, before any charge transfer

can begin across the interface between the driving electrodes and the carrier fluid, the standard potential barrier must be overcome. This barrier, or resistance, is dependent on the electrode material and the composition of the carrier fluid. The second factor that reduces the effective field is the formation of a polarization layer at the interface. This layer, often called a double layer, is composed of ions that in effect create an electric field that opposes the applied field, thereby shielding the bulk of the carrier fluid from the applied voltage. The double layer is quite complex and has attracted the attention of many researchers who have extensively studied the topic and attempted to explain it [87].

One way to determine the effective electric field is to perform separations of analytes with known electrophoretic mobility [88]. In this way the effective electric field can be calculated as

$$E_{eff} = \frac{6Dt_R}{\mu_e w t_0} = \frac{2k_B T t_R}{\mu_e w \pi \eta d_h t_0} \tag{2.12}$$

where T is the temperature, k_B is Boltzmann's constant. Terms specific to the analyte are the mass diffusion coefficient, D, the hydrodynamic diameter, d_h, and the electrophoretic mobility, μ_e. For a spherical particle, d_h is equal to the particle's diameter, d.

Electrophoretic Mobility

A number of factors influence the movement of particles that are subjected to electrophoretic conditions, and the overall combined effect is expressed in terms of the electrophoretic mobility,

$$\mu_e = \frac{\zeta \varepsilon_r \varepsilon_0}{6\pi\eta}. \tag{2.13}$$

Equation 2.13 is valid for small particles in carrier fluids of low ionic strength, and shows that electrophoretic mobility is proportional to the zeta potential, ζ, of the

particle and the permittivity of the carrier fluid, $\varepsilon_r \varepsilon_0$, and inversely proportional to the viscosity of the carrier fluid.

Electrokinetic/Zeta Potential

If ions of one sign are an integral part of, or are adsorbed by a particle, then the particle is said to be charged. When the charged particle is suspended in a solution, an electrical double layer is formed around it. This double layer is composed of the charges fixed to the particle and the relatively mobile counterions of the carrier fluid that accumulate near the particle (Fig. 2.2)[89]. The ions immediately surrounding the particle are bound so tightly that they move with the particle, defining a surface of shear

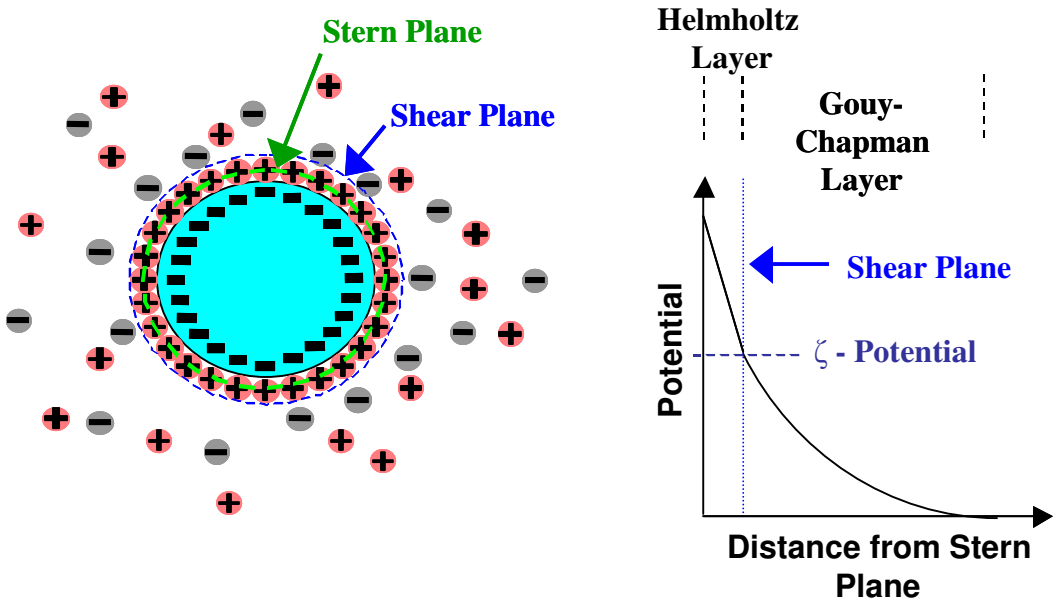

Figure 2.2: Depiction of (left) a small particle and ions in solution, the Stern plane, the shear plane and the establishment of an electrokinetic potential; and (right) a graph showing the potential as a function of distance from the Stern plane.

distinct from the particle's actual surface. The potential at the shear surface, with respect to that of the bulk carrier fluid is what governs the electrophoretic mobility of the particle and is therefore termed the electrokinetic or zeta potential. The value of the zeta potential and the thickness of the double layer both increase as the ionic concentration of the carrier fluid is decreased.

2.4 Basic Characterization Parameters

Characterization of the μ-ElFFF systems, the third specific aim, is similar to that performed on chromatographic systems, and includes the determination of four basic parameters for each design:

1. Plate height (H)
2. Retention parameter (λ)
3. Steric inversion diameter (d_i)
4. Biocompatibility (qualitative)

Knowing the values of these key aspects is essential to comparing the separation efficiency of these systems with previously developed technologies.

Plate Height

In order to compare the efficiency of current μ-ElFFF systems with other separation systems, measurements of the systems' plate heights need to be performed. Plate height is a measure of the degree of band broadening per unit length along the direction of flow, with shorter the plate heights indicating to less band broadening. As shown by Equations 2.4 and 2.7, shorter plate heights correspond to a higher degree of resolution and more efficient separations.

There are many factors that contribute to the total plate height of a system, namely,

$$H = \sum H_i + H_p + H_n + H_D + H_r . \tag{2.14}$$

The first factor, H_i, is the instrumental factor. The instrumental factor includes factors specific to the device (e.g. surface roughness, joints, etc.), connected elements (e.g. tubing, injection ports, etc.) and sample plug length. This component can be significant in poorly designed systems; however, in carefully designed systems, its contribution to the overall plate height may be negligible.

The second component, H_p, is due to sample polydispersity. As expected, and as shown by Equation 2.14, a sample with low polydispersity will yield a shorter total plate height than one with high polydispersity. Since the effect the electric field has on a particle is directly related to its hydrodynamic diameter and composition, particles in a polydisperse sample will equilibrate to different heights in the channel, with the smaller ones on the leading edge of the band. However, the differences between the particles in a polydisperse sample are usually so small that it is impossible to separate them into two distinct peaks.

Nonequilibrium effects, H_n, are the principal origin of dispersion (Figure 2.3). Particles in the channel form a cloud of a certain thickness and length. The laminar flow profile dictates that the particles closer to the center of the channel flow at a faster rate than those closer to the accumulation wall. This velocity gradient produces a broadening of the cloud (increased length) in the direction of carrier flow. These effects are dependent on the channel thickness and the strength of the applied field, as shown by

$$H_n = \frac{24D^2\langle v\rangle}{U^3 w}, \tag{2.15}$$

where diffusivity is given by D, U is the drift velocity, $\langle v\rangle$ is the average carrier velocity and w is the channel thickness.

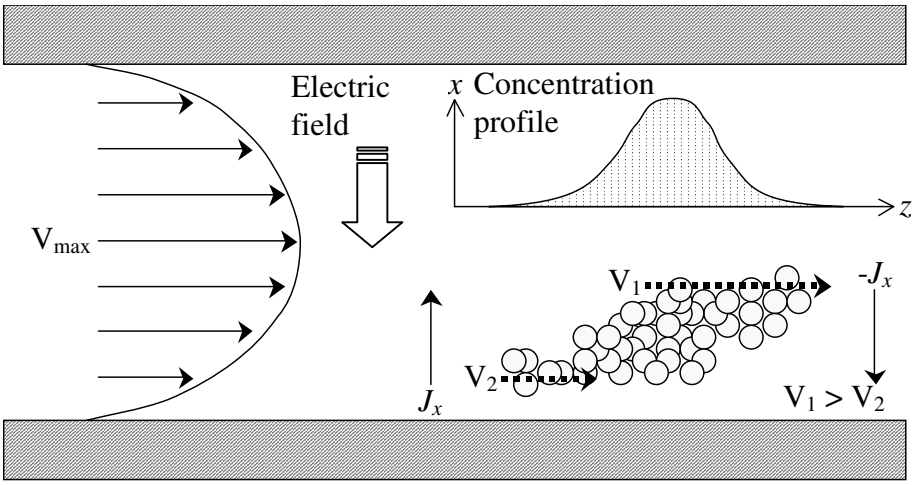

Figure 2.3: Dispersion occurs due to concentration gradients within particle bands. Higher particles, moving faster than lower ones, are forced to lower positions due to diffusive flux (J_x) and slow down.

Another factor that affects plate height is the contribution of diffusion within the sample, defined as H_D. Like H_i, H_D is often negligible when compared to the other factors. This component, due to axial diffusion, is usually negligible because most analytes have high molecular weights that correspond to small diffusion coefficients. However, if the flow rate is sufficiently low, then H_D becomes a factor that must be accounted for.

The last factor that contributes to the overall plate height, termed H_r, is due to relaxation effects. When a sample is first introduced into the channel, time is required for the analyte to relax into its quasi-equilibrium distribution. While the value of this term may be estimated, it is often more simple to eliminate it by allowing the analyte to relax in the absence of carrier flow (i.e., stop-flow relaxation). This is done by injecting the sample and stopping the flow when the sample first enters the field. The flow should be stopped for an amount of time equal to the maximum time required for an analyte to travel the length of the channel.

Experimentally, the number of theoretical plates (inversely proportional to plate height) can be determined by

$$N = 5.54\left(\frac{t_R}{w_{1/2}}\right)^2, \tag{2.16}$$

where t_R is the retention time and $w_{1/2}$ is the width of the peak at half-height (Figure 2.4).

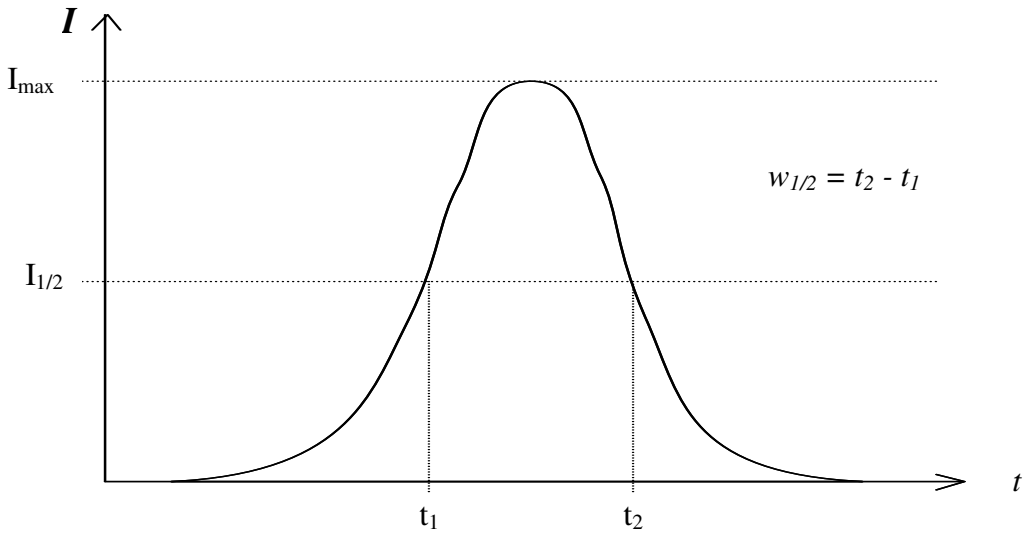

Figure 2.4: Diagram showing how values for t_1 and t_2 are found to determine the value of $w_{1/2}$.

By injecting a volume of an unretained fluid (e.g. 0.17 N NaCl solution) into the channel of each device at various flow rates, the resulting data can be analyzed to determine the number of theoretical plates with respect to each flow rate using Equation 2.16. Additionally, plate heights for each flow rate can be easily calculated using Equation 2.4,

which shows that the number of theoretical plates is inversely proportional to plate height.

Retention Parameter

Retention parameters, λ, are specific for different sample components and vary only with different applied field strengths and channel thicknesses since

$$\lambda = \frac{D}{\mu_e E_{eff} w} = \frac{D}{Uw}. \tag{2.17}$$

Low retention parameters are characteristic of efficient separation systems. Furthermore, retention parameters provide a relative measure of the thickness of the particle fields, parallel to the electric field. As demonstrated previously in Section 2.3, the thickness of the particle field in conjunction with the parabolic flow velocity profile in the channel determines the velocity of the particles and directly impacts their time of elution. The resulting retention time can be used in Equation 2.3 to determine the retention ratio. Once this value is known then, by combining Equations 2.12 and 2.17, the retention parameter can be found to be

$$\lambda = \frac{R}{6}. \tag{2.18}$$

This equation holds for high retention levels. Therefore, even if the sample components are unknown, the retention parameter can still be calculated, enabling the determination of physicochemical properties. From Equations 2.3 and 2.18 it can be seen that a lowering of the retention parameter, λ, will result in higher retention times. Likewise, Equation 2.17 shows that an increase in drift velocity for a given channel height will also yield higher retention times. The use of Equation 2.17 requires caution, however, since under normal circumstances, the drift velocity, also a function of channel height, would be calculated as

$$U = \frac{\mu_e V_{app}}{w}. \tag{2.19}$$

However, as explained in Section 2.3, because of the high capacitance created as a result of double layer effects at the electrode/carrier fluid interface and the high impedance due to the charge transfer resistance of the carrier fluid, it has been shown that the effective electric field is much smaller (<1%) than that calculated by dividing the applied potential difference by the channel height (i.e. the applied electric field). This results in a much lower drift velocity, corresponding to a much higher value of λ (i.e., lower retention). One way this effect may be lessened is by using a pulsed voltage, as shown by Lao, et al. [90].

Steric Inversion Diameter

In μ-ElFFF systems, there is a particle size limit, known as the steric inversion diameter, where the separation mode changes from "normal" to "steric". This diameter can be estimated theoretically by

$$d_i = \sqrt{\frac{2k_B T}{3\pi\gamma\eta U}}, \tag{2.20}$$

where γ is a dimensionless number on the order of unity (used to compensate for wall repulsion and other effects). It is important to note that in μ-ElFFF systems, the value of d_i has been shown to increase with increasing conductivity of the carrier solution [12]. This fact indicates that in these systems, d_i depends on the effective diameter of the particles, not just their physical diameters.

The steric inversion diameter can be found experimentally by maintaining a constant potential while varying the particle diameter or, if using a single particle size, by increasing the voltage until there is no more increase in the retention time. The latter method is usually not employed for ElFFF systems since the voltage may exceed the limit for electrolysis. Since the drift velocity, U, for a given system is not known initially, the value of d_i for each system must be found experimentally by maintaining a constant potential while injecting particles of various diameters in a specific carrier fluid.

Biocompatibility

It is of great interest to be able to use μ-ElFFF systems for a wide range of biological materials. If samples containing whole cells are used, it may be essential for certain applications that the cells remain viable after the separation is complete. Therefore, the systems should be tested to determine whether or not cells remain viable. This can be done by using specific stains or dyes and visual inspection of the cells before, during and after the cells are subjected to the electric field.

For separations of DNA markers, it is important that the surfaces prohibit the adhesion of the markers in order to accurately and effectively separate the individual components (minimize band broadening) as well as to maximize the yield (sample out/sample in). To qualitatively measure the yield, any DNA markers remaining in the channel after a separation can be labeled and optically detected.

2.5 Theory of Electrical Conductivity Detection

The Coulter counter method is widely used to count cells for biological studies, and has been cited extensively in the literature [91, 92]. In this method, a measurement is made of the change in resistance of a channel as a cell passes through it. It is well known that the resistance of the channel, R_0, can be defined as

$$R_0 = \frac{\rho l}{A} = \frac{\rho l A}{A^2}, \tag{2.21}$$

where ρ is the resistivity of the carrier medium, l is the length of the channel, and A is the cross-sectional area of the channel. Furthermore, if there is a cell in the channel, then the new resistance across the channel,

$$R_c = \frac{\rho}{A^2}\left(V_c + lA\right), \tag{2.22}$$

is directly related to the volume of the cell (V_c). Therefore, when a cell passes through the channel, there is a change in resistance,

$$\Delta R = R_c - R_0 = \frac{\rho}{A^2} V_c . \tag{2.23}$$

The ratio of this change in resistance to the original resistance of the channel is then

$$\frac{\Delta R}{R_0} = \frac{V_c}{lA}, \tag{2.24}$$

meaning that for each cell that passes through the channel, there is a measurable change in resistance that is directly proportional to the volume of that cell. If the size of the cells in a monodisperse sample is known, then it should be possible to derive the concentration of the cells as they pass the detector electrodes. Conversely, if the concentration is determined by using the optical method described above, then the electrical data could be used to determine the size of particles in a monodisperse sample.

2.6 RLS Theory

Optical detection and classification of various types of RLS particles can be achieved based on their light scattering properties. It may be said that the scientific study of light scattering began with the experiments performed by Tyndall in 1868 [93]. Tyndall's work demonstrated the relation between the suspended particle's size and the intensity and polarization of the scattered light. Later, in 1871, Lord Rayleigh provided a theoretical framework to the problem of relating the properties of the scatterer to the angular distribution of the scattered light for particles much smaller than the incident wavelength [94, 95]. To provide a theory applicable to homogeneous spheres of arbitrary size, in 1908, Gustav Mie treated the problem rigorously using classical electromagnetic theory [96]. A combination of the theories of Rayleigh and Mie enables one to approximate the optical characteristics of small, homogeneous, spherical light scattering particles.

Rayleigh Theory

The Rayleigh theory, developed for small light-scattering particles, is only applicable to particles whose diameters are less than about 1/20 the wavelength of incident light [97]. Under these conditions, the wavelength of the scattered light under white light illumination remains constant. This phenomenon can be explained by the fact that if a particle is much small compared to the wavelength of an electromagnetic wave, then the instantaneous electromagnetic field is uniform over the extent of the particle [98]. As a result, every electron in the particle sees the same phase of the wave and a dipole is created. The oscillating electrons radiate electromagnetic energy and it is this secondary emission that constitutes the scattering. The electrons oscillate with the same phase and therefore, there is no interference of the scattered light.

Additionally, a change in particle size results in a significant change in scattered light intensity (intensity ∝ radius^6) as given by

$$I = \frac{16\pi^4 a^6}{r^2 \lambda_0^4} \left| \frac{m^2 - 1}{m^2 + 2} \right|^2 \sin^2 \psi \tag{2.25}$$

where a is the particle radius, r is the distance from the particle at which the scattered light is observed, and λ_0 is the wavelength of the incident light in the medium. The term m is a complex relative refractive index used for absorptive particles, dependent on the real and imaginary refractive indices of the particle in a vacuum (n_{Re} and n_{im}, respectively) and the refractive index of the medium, n_{med}, given by

$$m = \frac{\left(n_{\mathrm{Re}} + i n_{im}\right)}{n_{med}}, \tag{2.26}$$

(where $i = \sqrt{-1}$) and ψ is the angle measured from the scattering direction to the dipole as shown in Figure 2.5 [98]. The intensity of the scattered radiation in the yz-plane (i.e., $\psi = 90°$) is

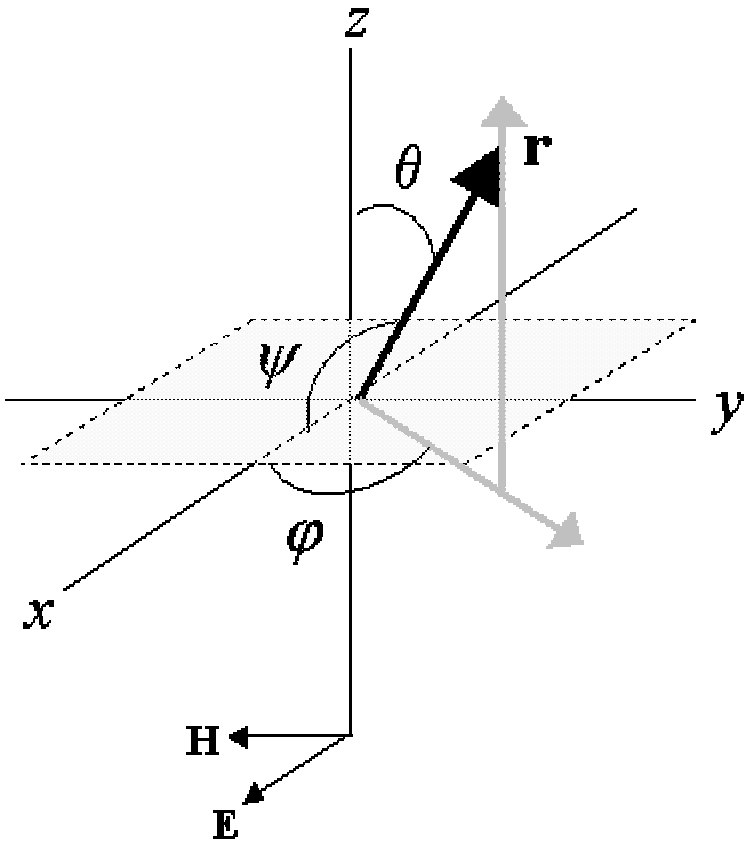

Figure 2.5: Diagram showing the coordinate system for light scattering from a small particle (center at origin) with the incident light in the positive *z*-direction and an electric polarization along the *x*-axis.

$$I_{perp} = \frac{16\pi^4 a^6}{r^2 \lambda_0^4} \left| \frac{m^2 - 1}{m^2 + 2} \right|^2 \tag{2.27}$$

and is independent of the angle of observation since all directions in this plane are equivalent with respect to the dipole. The intensity of the scattered radiation in the *xz*-plane, where the value of ψ is variable, is

$$I_{par} = \frac{16\pi^4 a^6}{r^2 \lambda_0^4} \left| \frac{m^2 - 1}{m^2 + 2} \right|^2 \cos^2 \theta \tag{2.28}$$

where θ, the angle of observation as measured from the direction of the incident light to the direction of the scattered light is

$$\theta = \left(\frac{\pi}{2}\right) - \psi . \tag{2.29}$$

For the case of an unpolarized incident wave, the intensity of the scattered light is the average of the two incoherent, linearly polarized components that are perpendicular and parallel to the scattering plane. This is shown by

$$I_U = \frac{I_{perp} + I_{par}}{2} = \frac{8\pi^4 a^6}{r^2 \lambda_0^4} \left| \frac{m^2 - 1}{m^2 + 2} \right|^2 \left(1 + \cos^2 \theta\right). \tag{2.30}$$

In the usual case of colloidal solutions irradiated by visible light, the average distance between particles is very large with respect to λ_0, and therefore, there are no coherent phase relations between the light waves scattered by different particles. Consequently, the total energy scattered per unit volume is proportional to the particle concentration. For a suspension of spherical particles of uniform size, the concentration and diameter can be determined through measurement of the attenuation of the incident beam [99]. Rewriting the equation above in terms of the particle volume, V_{par}, instead of the radius, *a*, yields the intensity scattered per unit volume,

$$N_{par} I_U = \frac{9\pi^2 N_{par} V_{par}^2}{2 r^2 \lambda_0^4} \left| \frac{m^2 - 1}{m^2 + 2} \right|^2 \left(1 + \cos^2 \theta\right), \tag{2.31}$$

where N_{par} is the number of particles per unit volume.

Mie Theory

As previously mentioned, the Mie theory is useful for determining light scattering properties of any sized homogeneous, spherical particles [96, 97, 100-103]. This theory takes into account the light scattered by electrons in different parts of the particle, making it useful for large particles. Recent work has shown that as particle size increases beyond

that of the Rayleigh size limit, several changes occur in light scattering and absorption properties [100]. Of particular interest is the shifting of absorption and scattering spectral profiles toward longer wavelengths (i.e., different sized particles correspond to different colors of scattered light). These shifts are caused by electrons in different positions within the particle oscillating with different phases, thereby generating interference in the scattered light. In addition to the changes in the wavelength of the scattered light, since the refractive index of most metals depends very strongly on the incident wavelength, λ_0, the intensities of the scattered light vary from the λ_0^{-4} proportion calculated by the equations above.

By measuring the amount of light absorbed by a suspension of particles, the extinction cross section, C_{ext}, which is the sum of the light scattering power of a particle, C_{sca}, and its absorption cross section, C_{abs}, or

$$C_{ext} = C_{sca} + C_{abs}. \tag{2.32}$$

can be determined from the equation

$$I_T = I_0 e^{-\rho_{par} C_{ext} L}, \tag{2.33}$$

where I_0 is the intensity of the incident light, I_T is the intensity of the transmitted light, ρ_{par} is the concentration of the particles and L is the optical path length. The extinction cross section is directly proportional to the Mie extinction coefficient, K, and inversely proportional to the volume of one particle, where

$$K = \frac{C_{ext}}{V_{par}}, \tag{2.34}$$

and has units of cm^{-1}.

According to the Mie theory, the extinction coefficient is determined by the expression

$$C_{ext} = \frac{2\pi}{k^2} \sum_{n=1}^{\infty} (2n+1) \mathrm{Re}(a_n + b_n), \tag{2.35}$$

where the propagation constant, k, is defined as $k = \frac{2\pi n_{med}}{\lambda_0}$ and the term n=1 corresponds to the electric dipole. Noteworthy is the fact that C_{ext} is a function of the incident wavelength. A plot of C_{ext} versus wavelength would show that different sized gold particles have distinct 'resonance' peaks at wavelengths between 500 and 700 nm for gold particles with diameters between 20 to 140 nm [97]. The terms a_n and b_n in the equation for determining the extinction cross section are complex coefficients defined in terms of Bessel and Riccati functions by

$$a_n = \frac{\left[\left(\frac{D_n(mx)}{m}\right)+\left(\frac{n}{x}\right)\right]\Psi_n(x)-\Psi_{n-1}(x)}{\left[\left(\frac{D_n(mx)}{m}\right)+\left(\frac{n}{x}\right)\right]\xi_n(x)-\xi_{n-1}(x)} \tag{2.36}$$

$$b_n = \frac{\left[mD_n(mx)+\left(\frac{n}{x}\right)\right]\Psi_n(x)-\Psi_{n-1}(x)}{\left[mD_n(mx)+\left(\frac{n}{x}\right)\right]\xi_n(x)-\xi_{n-1}(x)}, \tag{2.37}$$

with the size parameter, $x = \frac{2\pi a n_{med}}{\lambda_0} = ka$, and $D_n(mx)$, the logarithmic derivative of $\Psi_n(mx)$, defined by

$$D_n(mx) = \frac{d\ln\Psi_n(mx)}{d(mx)}. \tag{2.38}$$

Further, D_n satisfies the downward recurrence relation

$$D_{n-1} = \frac{n}{mx} - \frac{1}{D_n + \frac{n}{mx}}. \tag{2.39}$$

This calculation is started with a value of $n = N_{\max}$, calculated with $N_{\max} = n_{\max} + 15$. It is assumed that $D_{N_{\max}} = 0.0 + i0.0$, and the number of terms, n_{max}, is determined with the

expression $x+4x^{1/3}+2$, where x is the size parameter defined above. The Riccati-Bessel functions, Ψ and ξ, are recurrence relations given by

$$\Psi_{n+1}(x)=\frac{2n+1}{x}\Psi_n(x)-\Psi_{n-1}(x) \tag{2.40}$$

$$\xi_n=\Psi_n-i\chi_n. \tag{2.41}$$

The initial values used in the evaluation of these functions are

$$\Psi_{-1}(x)=\cos(x) \tag{2.42}$$

$$\Psi_0(x)=\sin(x) \tag{2.43}$$

$$\chi_{-1}(x)=-\sin(x) \tag{2.44}$$

$$\chi_0(x)=\cos(x). \tag{2.45}$$

According to the Mie theory, the intensity of the scattered light (when the incident light is unpolarized) is

$$I_U=\frac{\lambda_0^2}{8\pi^2 n_{med}^2 r^2}\left(|S_1|^2+|S_2|^2\right), \tag{2.46}$$

where S_1 and S_2, termed the amplitude functions, are evaluated using the expressions

$$S_1=\sum_{n=1}\frac{(2n+1)(a_n\pi_n+b_n\tau_n)}{n(n+1)} \tag{2.47}$$

$$S_2=\sum_{n=1}\frac{(2n+1)(a_n\tau_n+b_n\pi_n)}{n(n+1)}, \tag{2.48}$$

where the upward recurrence relations,

$$\pi_n=\left(\frac{(2n-1)\cos\theta}{n-1}\right)\pi_{n-1}-\left(\frac{n}{n-1}\right)\pi_{n-2} \tag{2.49}$$

$$\tau_n=(n\cos\theta)\pi_n-(n+1)\pi_{n-1}, \tag{2.50}$$

are started with $\pi_0=0$ and $\pi_1=1$.

2.7 Conclusions

Many of the characterization parameters used for ElFFF are similar or the same as those used for chromatographic systems. Both are flow-based separation methods in which a finite sample volume is injected into a flowing media. The theory for these separation methods took many years to be developed, and much work continues to learn more about these systems.

Much information can be gained by employing a combination of electrical and optical detection. Particle size, volume or type can be determined using these methods of detection. The Rayleigh and Mie theories explain how optical detection can be useful for sample characterization of a wide variety of particle compositions and sizes. The change in intensity and color with respect to particle size can be exploited to analyze a wide variety of samples.

In this work, the main type of particles to which these theories will be applied are RLS Particles^{TM}. Commercially available, RLS Particles^{TM} are metal (i.e., gold or silver) nanospheres with diameters ranging from 40 nm to 100 nm. The gold RLS Particles^{TM} can be easily conjugated with specific antibodies, making them practical tools for detection and analysis of certain types of biological samples [104-108]. Additionally, the Mie theory can be used to calculate the concentration and may be used to determine the composition and polydispersity of a sample.

CHAPTER 3

μ-ElFFF SYSTEM AND FABRICATION PROCESS DESIGN

3.1 Design

This chapter describes the design and fabrication of μ-ElFFF systems of various channel heights and the development of two, complimentary on-column detection systems for integration into the μ-ElFFF systems.

Design Rules

Before proceeding with the design and fabrication of the devices, four channel design rules were established; that is, the channel had to

1. Have a high aspect ratio (channel width:height > 100:1) to provide a laminar parabolic velocity flow profile
2. Be fabricated of materials that are biocompatible
3. Enable on-column optical detection
4. Have flat, smooth channel surfaces

The high aspect ratio is important for two reasons. First, for a given channel cross sectional area and applied voltage, a high width-to-height aspect ratio makes it possible to maximize the electric field, as the electrodes will be more closely spaced. Second, increasing the aspect ratio while maintaining the same channel cross sectional area increases the wetted perimeter (see Equation 2.10). This, in turn, corresponds to a decrease in the hydraulic diameter and the Reynolds number (Equation 2.9). Therefore, by increasing the aspect ratio, the chance of having laminar flow within the channel is increased. This is of great importance since the flow velocity profile that is characteristic of laminar flow is required for separations to be effected in ElFFF systems.

The second design rule, the biocompatibility of the channel, is necessary for these systems to be useful for performing separations of biological components like whole cells, proteins or DNA. This aspect is important because of the growth of the biotechnology field and the growing interest in biochemical analysis and sample preparation. One of the novel characteristics of this work is the use of glass substrates to build a microsystem. Glass is a non-conventional material for MEMS fabrication technologies, yet it is a material that is used extensively in the biologically-related fields. While glass is not a traditional material for MEMS technologies, it is an ideal material for building a biocompatible μ-ElFFF system. Glass substrates can be processed in many similar ways as silicon is. Therefore, glass is a good choice for both its biocompatibility and its manufacturability.

Fabricating the μ-ElFFF devices with transparent substrates enables optical detection to be performed—the third design rule. In the μ-ElFFF system, for optical detection to be possible between the electrodes, it is necessary to choose transparent electrode materials. One common example of a transparent, conductive material is indium tin oxide (ITO).

Finally, the fourth design rule is to make the sidewalls of the channel smooth. Rough sidewalls could make the flow more turbulent and increase the plate height, as the instrumental factor contribution (H_i in Equation 2.14) would have a larger value. As described in Chapter 2, the increased plate height would cause a decrease in separation efficiency.

Design Modifications

The fabrication of early μ-ElFFF systems revealed several minor problems, as may be expected when developing a new system. The five main problems that were encountered included

1. Poor adhesion of SU-8 to glass
2. Modification of the glass surfaces through standard MEMS processes
3. Inherent intricacies of using thin, non-standard substrates in a cleanroom environment
4. Adverse effects of glass-to-glass bonding processes on patterned electrodes (i.e., oxidation, breaking)
5. Poor performance of common bonding adhesives (for both the substrates and the interconnects)

As a result, several design changes were implemented and key processes were modified and characterized, enabling the successful development of the current systems.

3.2 System Components

The μ-ElFFF systems, with integrated RLS detection and on-column ECM detection, have three main components: a separation channel, an electrical conductance detector, and features to enable optical RLS detection.

Separation Channel

The separation channel is somewhat different than in similar, previously developed systems [62]. The most notable change is that both substrates are glass, which enables RLS detection. As a result, the current design requires both thick (~1 mm) and thin (~150 μm) slides. While the thick slides are standard 25 mm x 75 mm x 1 mm microscope slides, and readily available, the thin slides require modification through photolithographic processes and wet etching with HF. Furthermore, the input and output ports are created by either an isotropic wet etch (using HF) or by mechanical drilling (using a diamond tipped bit) rather than by using a KOH etch. While the first channels were lined with gold (the electrode material), the new channel electrodes are made using

platinum or indium tin oxide (ITO). Platinum metal is preferred over gold for making the electrodes since chrome or titanium adhesion layers migrate up through the gold and oxidize during thermal bonding. The oxidation of the metals that migrated to the surface causes them to be nonconductive. Since the electrical connections are made on the surface, this migration and subsequent oxidation makes the devices unusable. The main reasons for choosing ITO to use as the electrode material, as mentioned above, are that it is transparent and conductive, even after performing the thermal bonding. For the current design, channels are made in three different thicknesses: 5μm, 30μm and 150μm. Wet etching of a glass slide and bonding another slide on top forms the thin (5μm) channels. The 30μm channels include a photolithographically defined spacer (SU-8 10, MicroChem, USA). For the thick (150μm) channels, a glass spacer is used to define the height.

ECM Detector

The ECM detector is comprised of two thin metal traces (photolithographically defined to be approximately 75 μm wide), one on each of the top and bottom substrates. They are located near the end of the separation channel, 500 μm away from the main electrodes, to allow for maximum time between introduction of the sample into the channel and detection of the separated analytes.

Optical RLS Detector

For RLS particle detection, an upright, bright field microscope (12-561T Micromaster, Fisher Scientific Co., Pittsburgh, PA) with a modified illumination scheme is used to view particles as they move through the separation channel and at the ECM detector. This is made possible by "windows" incorporated along the length of the channel in the metal electrodes or through the use of ITO as the electrode material. A

CCD camera attached to the microscope allows digital capturing of images and video as well as analog recording to VHS.

3.3 μ-ElFFF System Fabrication

Process Flows

The first step toward developing the μ-ElFFF systems was to create process flow diagrams and layouts of the masks required for the photolithographic processes (Figures 3.1-3.5). A process flow for an existing μ-ElFFF system is shown in Figure 3.1. The

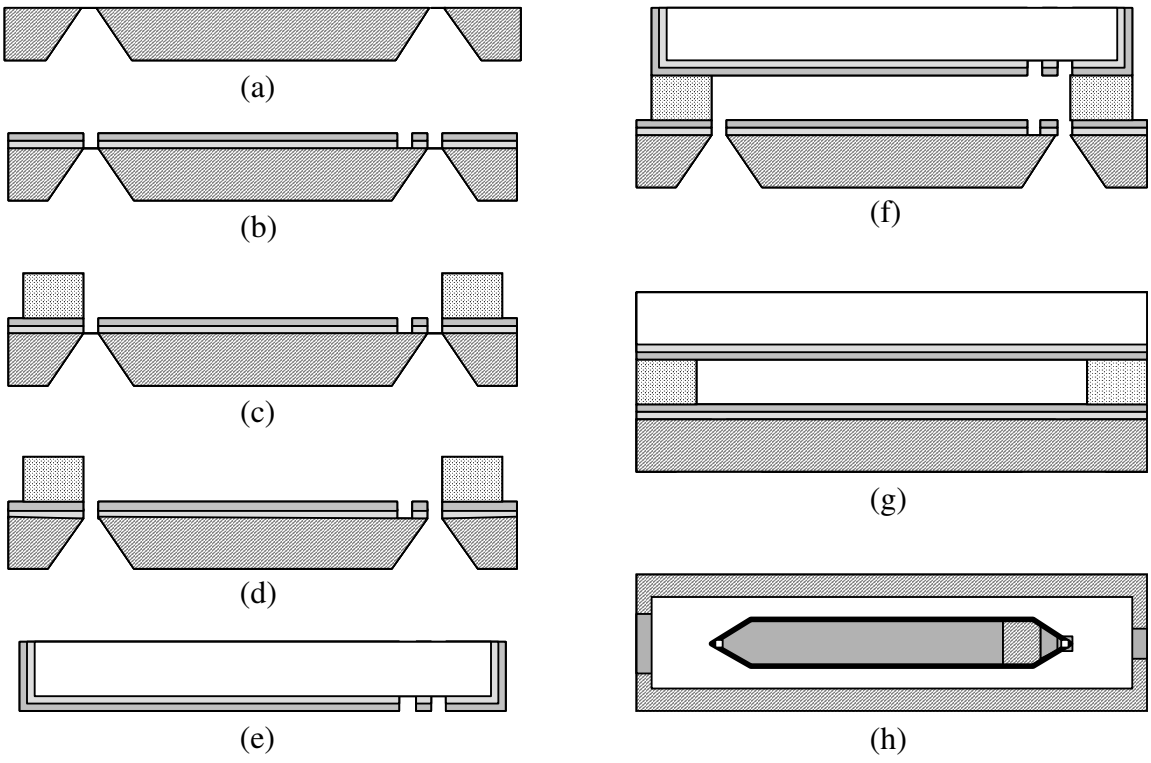

Figure 3.1: Process flow diagram showing bottom silicon substrate after (a) KOH etching, (b-c) depositing and patterning metal and polyimide, and (d) opening of ports; top substrrate after (e) depositing and patterning metal; (f) bonding of top and bottom substrates and (g) resulting channel cross section; and (h) top view of completed μ-ElFFF system.

process flows shown in Figures 3.2 and 3.3 reflect changes that were made in order to integrate the RLS particle detection. The major changes included replacing the silicon substrate with glass, creating "windows" in the electrodes along the length of the channel or using ITO, and developing bonding processes for making channels of each height.

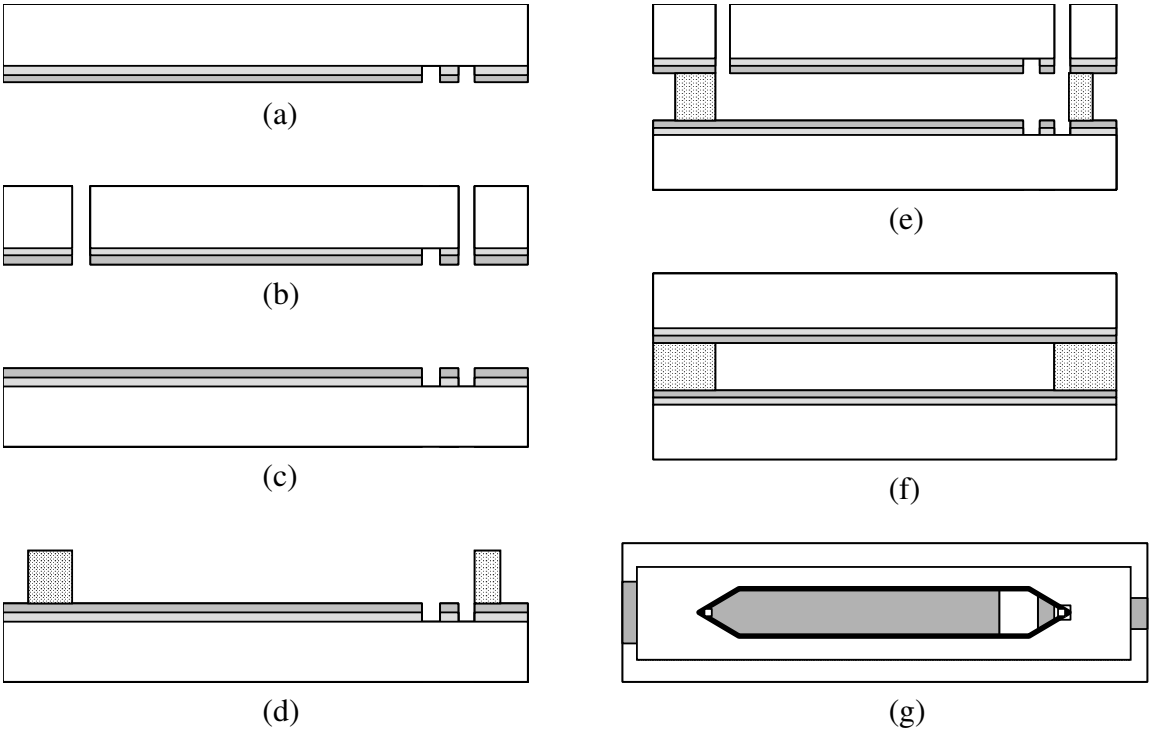

Figure 3.2: Process flow diagram showing top glass substrate after (a) depositing and patterning metal and (b) drilling input and output ports; bottom glass substrate after (c) depositing and patterning metal and (d) SU-8; (e) bonding of top and bottom substrates and (f) resulting channel cross section; and (g) top view of completed μ-ElFFF system.

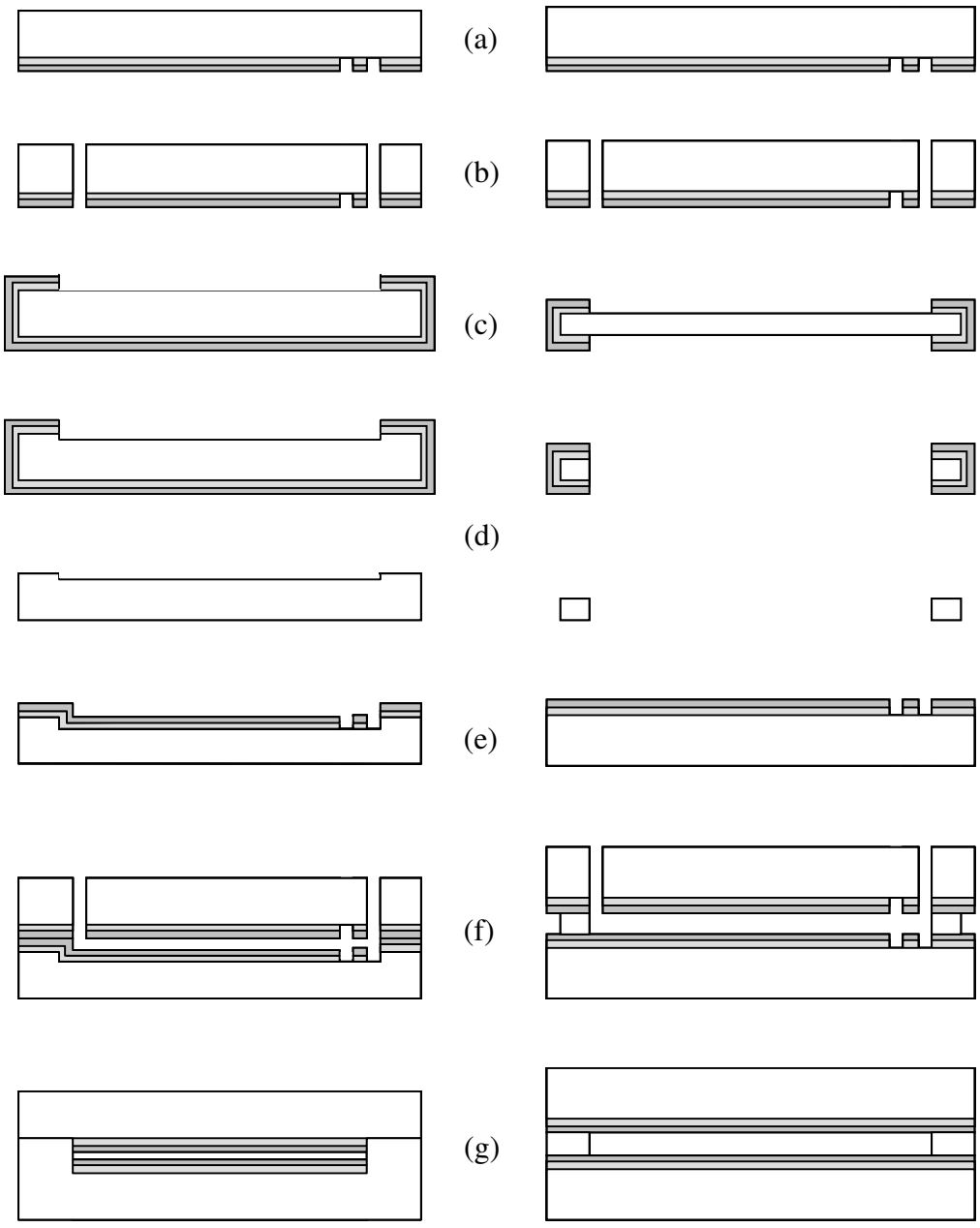

Figure 3.3: Process flows for all thermally bonded glass devices showing (a) deposition and patterning of metals on top substrates; (b) drilled ports; (c) patterned metal and photoresist prior to HF etching of glass and (d) resulting channel (left) and spacer (right); (e) patterned metal on bottom substrates; (f) bonding of top and bottom substrates; and (g) channel cross section views.

Masks for Photolithography

As stated above, masks were designed and fabricated for the photolithographic processes. Initially, there were a total of five layouts for the masks as shown in Figure 3.4. Each mask had patterns specific to each of the three channel widths (1 mm, 5 mm and 10 mm). Two of the masks were used for defining the ports and the two dimensional characteristics of all channels (Figs. 3.4A & 3.4B). The layouts on the other three masks were used to define

1. The electrodes with "windows" (Fig. 3.4C),
2. The "windowless" electrodes (Fig. 3.4D), and
3. The transparent (i.e., ITO) electrode (Fig. 3.4E).

The layouts for the "windowless" and the transparent electrodes enabled the visualization of flow patterns during separations. Specifically, for systems with metal electrodes, "windows" were patterned in the electrodes along the length of the channel, as defined by the design of the mask layout (Fig. 3.4C). Other systems made use of transparent ITO electrodes that were solid electrodes along the length of the channel (Fig. 3.4E).

After fabricating and testing several devices, it was determined that the mask layouts shown in Figure 3.4 should be modified to facilitate verification of electrode connections/integrity and to minimize the risk of damage to the electrodes during thermal bonding of the glass substrates. The result of these changes is shown in Figure 3.5. Specifically, the number of abrupt changes in size or shape was reduced by adding tapers or rounding corners, respectively.

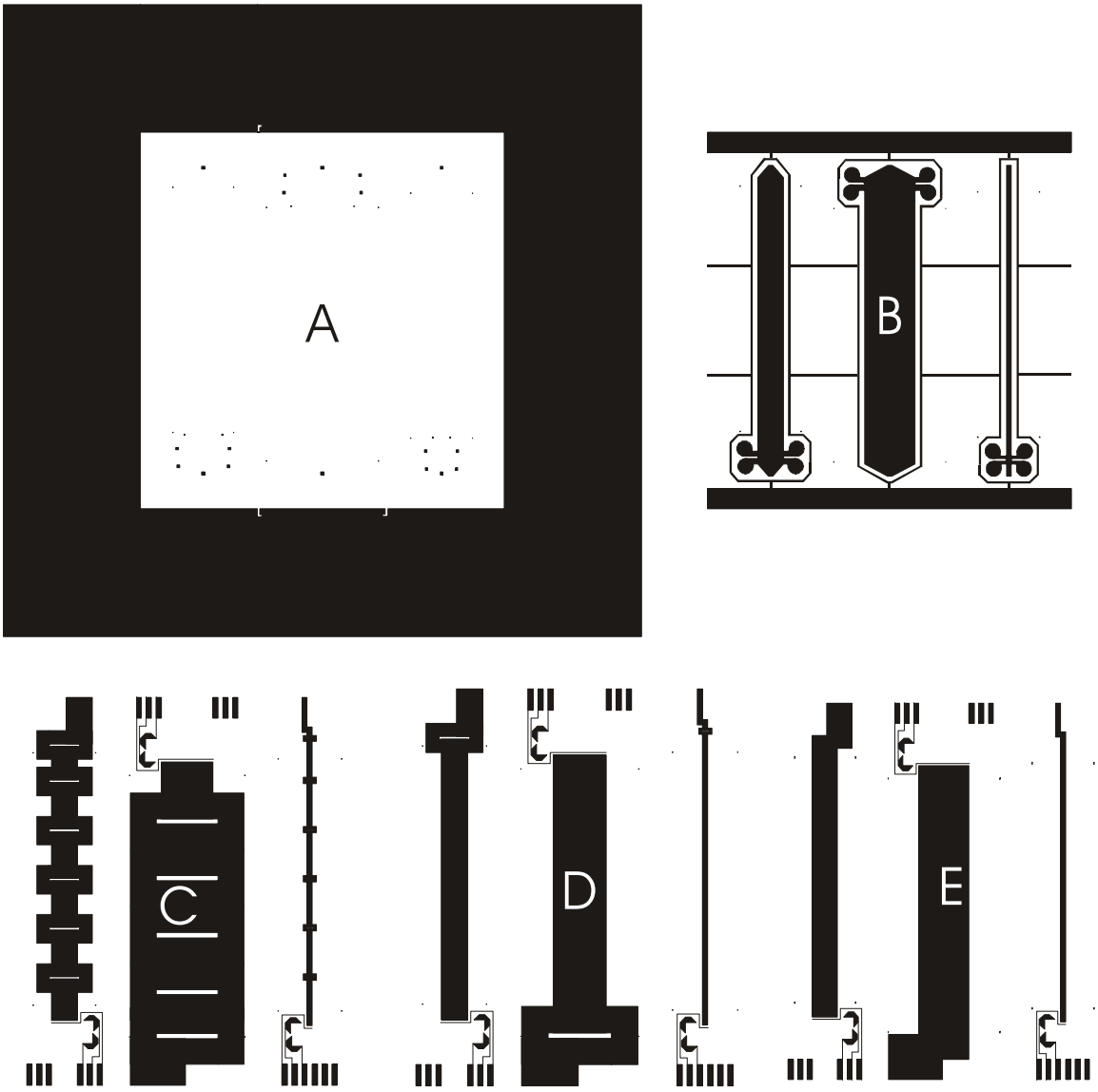

Figure 3.4: Mask layouts for the through-holes (ports) in top glass (A), channel walls and wicking channels / SU-8 layer (B), channels with "windows" (C), channels without "windows" (D), and channels with transparent electrodes (E). Masks A and B are common to all three channel designs.

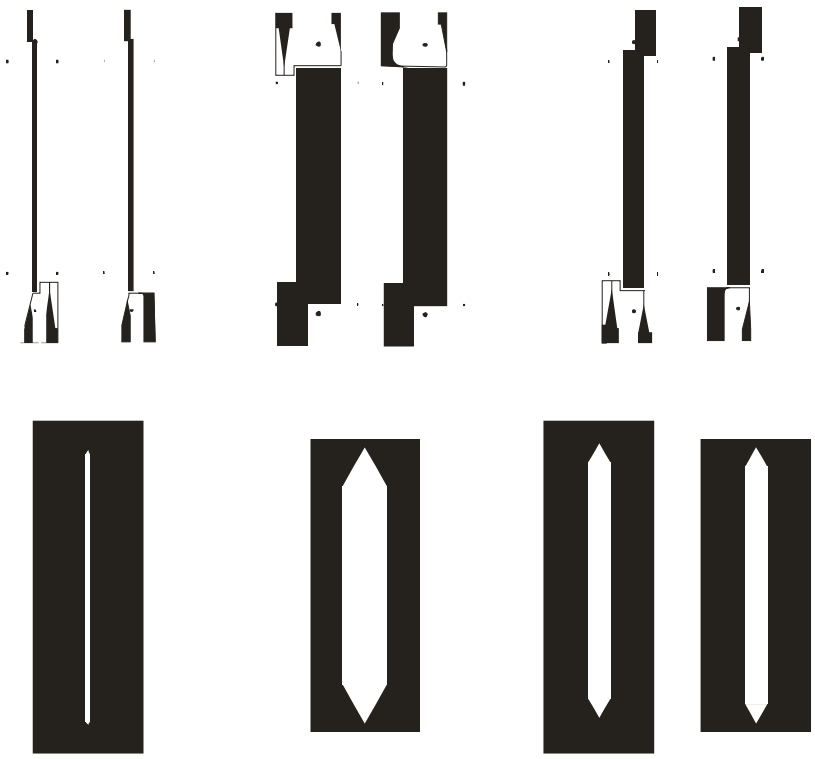

Figure 3.5: Mask layouts for the three sizes of μ-ElFFF channels showing (a) two electrode configurations per channel and (b) layouts that define the channel walls (long ones for 0.5 μm channels; short ones for making spacer on 150 μm channels).

Channels of 5 μm Height

As shown in Figures 3.2 and 3.3, the fabrication for each μ-ElFFF device of a certain channel height is slightly different. For the fabrication of the 5 μm channel height device, the first step is to coat the bottom glass with metal (500 Å Cr / 1000 Å Au). After patterning the metal using standard photolithographic techniques to define the channel, the glass is etched in a 25% solution of HF for 15 minutes, corresponding to an etched channel depth of 5 μm. Following the etch, the photoresist and the metals are removed using acetone and wet etchants, respectively. The next steps are to spin-on and pattern a negative tone photoresist (NR-9 8000P, Futurrex, Inc., Franklin, NJ) to define the areas

where the electrodes will be deposited. After depositing the electrode material, by RF sputtering for ITO or by electron beam (E-beam) deposition for Ti/Pt, a lift-off is performed by soaking the pieces in acetone for approximately 3 minutes. At this stage, the input and output ports are mechanically drilled into the top substrate. It is necessary to clean the top and bottom pieces prior to bonding. The cleaning consists of rinses with acetone, isopropanol and deionized (DI) water, followed by the use of a commercial glass cleaner. For bonding, the pieces are visually aligned and placed between boron nitride coated ceramic plates before being loaded into a high-temperature oven. The pieces are then thermally bonded to each other at 645°C for 3.5 hours. A cross section of the resulting channel is shown in Figure 3.6. Noteworthy is that the interface between the original substrates is no longer visible due to the complete bonding that occurred.

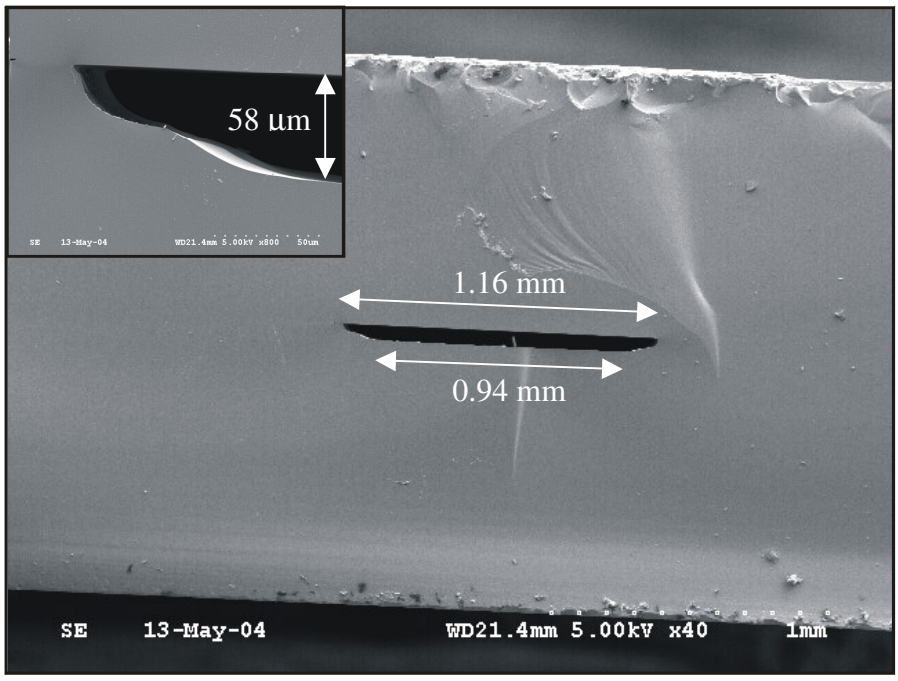

Figure 3.6: Cross section of 58 µm x 1mm channel made by wet etching in HF and subsequent thermal glass-to-glass bonding. Also shown is a close-up of the channel sidewall (inset).

For the 5 μm channels, the thermal bonding process caused problems both with the electrodes and with the channels. Electrodes made of Cr/Au were rendered unusable due to the migration of the chrome to the electrode surface and subsequent oxidation thereof. Changing the adhesion layer to titanium yielded the same results. However, making the electrodes using Ti/Pt solved this problem. Additionally, the channels collapsed due to the high aspect ratio (breadth/height=2000), so a lower aspect ratio of 200 was used.

Channels of 30 μm Height

To fabricate the devices with 30 μm high channels, the first step is to pattern the electrodes on clean glass substrates using the lift-off process as outlined above. For these devices, Ti/Pt, Cr/Au or ITO could be used for the electrodes. Next, a 30 μm thick layer of SU-8 is spun onto the bottom substrate and patterned to define the channel. Ports are then drilled in the top substrate, followed by a thorough cleaning with acetone, isopropanol and DI water. After visual alignment of the top and bottom pieces and clamping them together, a preliminary bonding is performed. This bonding step is performed in a convection oven at 85°C for 1 hour followed by a second bake at 125°C for 3 hours. Final bonding is accomplished by wicking a solventless, low-viscosity, UV adhesive into the wicking channels and curing under a UV light source for 1 hour. This step completes the fabrication of the device (Figure 3.7).

The main problem with the 30 μm channel height devices was that SU-8 would delaminate over time. Therefore, the SU-8 devices are useful for a limited time and are not as robust as thermally bonded devices. Additionally, there is some debate regarding the biocompatibility of SU-8. Replacing the SU-8 with a biocompatible material would solve this problem. However, finding a biocompatible material that can provide similar aspect ratios may prove difficult. Furthermore, the bonding protocol outlined above would likely require modification if SU-8 was substituted by another material.

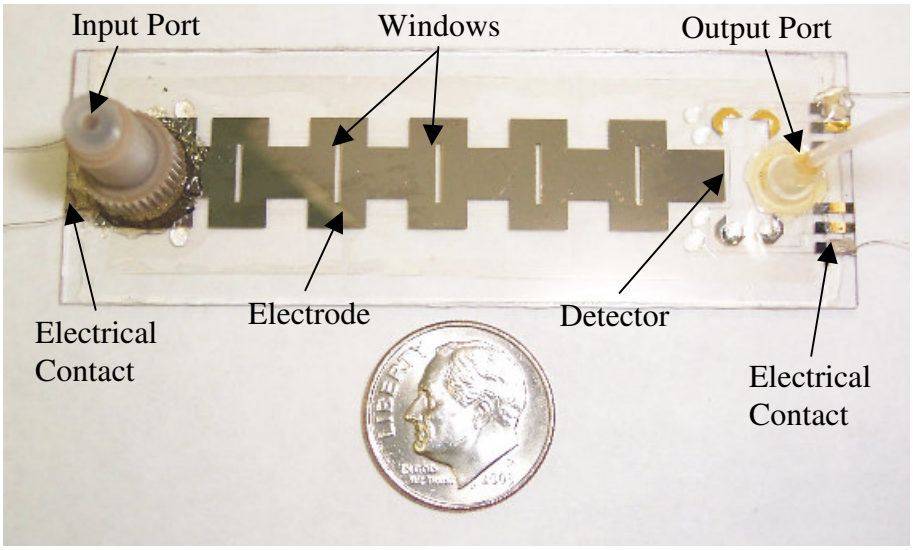

Figure 3.7: Picture of completed μ-ElFFF device with a 30 μm channel height. The channel is 6.2 cm in length and 0.5 cm wide. Input and output ports, electrodes, windows and electrical contacts are labeled.

Channels of 150 μm Height

Patterning electrodes using the lift-off process, as described above for fabricating the 30 μm high channel devices, is the first step in making the 150 μm high channel devices. Next, mechanical drilling through the top substrate is used to create input and output ports. A thin metal layer (500 Å Cr / 1000 Å Au) is then sputtered onto both sides of a thin (150 μm) borosilicate glass slide. A thick positive tone photoresist (AZ 4620, Clariant, USA) is spun on and patterned (on both sides) to define the channel. The metals are then wet etched to expose the glass in preparation for a wet etch in 25% HF for 15 minutes. For the chrome, a commercially available etchant is used, while a custom solution composed of 4 g of KI, 1 g of I_2 and 40 mL of DI water is used to etch the gold. Following the HF etch, the photoresist and the metals are completely removed with acetone and wet etchants (as described above), respectively. Finally, following a visual

alignment of all three substrates, the device is placed between two boron-nitride coated ceramic plates and baked in a high-temperature oven at 645°C for 3.5 hours. A completed 150 µm channel height device with ITO electrodes is shown in Figure 3.8.

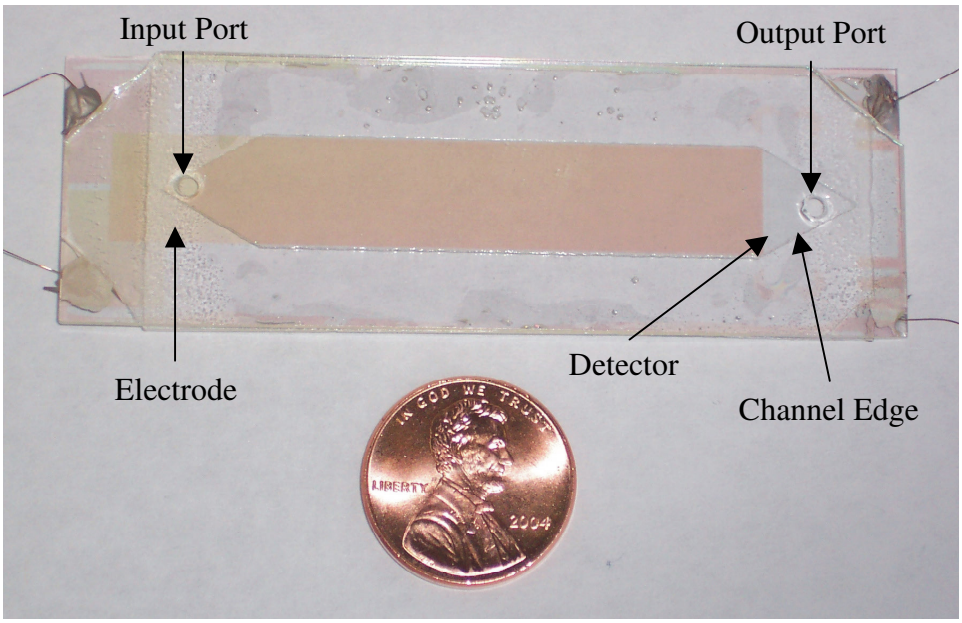

Figure 3.8: Picture of a completed µ-ElFFF device with a 150µm x 6.2 cm x 1 cm channel and transparent, ITO electrodes. The input port is on the left and the electrical contacts (2 on each end) are shown.

The larger devices with the 150 µm high channels proved extremely robust and could be used for hundreds of runs over the course of many weeks. Their main limitation was the degradation of the electrodes (both the main and the ECM electrodes) as a result of high voltages or high currents.

3.4 Conclusions

Three sizes of μ-ElFFF devices were built, ranging from 5 μm to 150 μm in channel height. The systems that were bonded using thermal bonding of glass to glass were much more robust than those that were bonded by other means. For the μ-ElFFF devices, the main electrodes were Cr/Ar, Ti/Pt or ITO, deposited using RF sputtering or E-beam deposition. For the electrodes made of non-transparent conductors (i.e., Cr/Au and Ti/Pt), openings in the electrodes enabled limited visualization of the channel interior at discrete positions along the length of the channel. However, the transparency of the ITO electrodes enabled visual observation of the flow in all areas of the channel. In the next chapter, Chapter 4, the operation and characterization of the μ-ElFFF systems will be presented, and in Chapter 5, both the ECM system that was fabricated as per the above discussion and the optical detection will be described in detail.

CHAPTER 4

OPERATION AND CHARACTERIZATION OF THE μ-ElFFF SYSTEMS

In this chapter, the details of the experimental setup will be provided. Additionally, the methods used to characterize each of three sizes of μ-ElFFF systems will be outlined. The results of each characterization procedure will be presented, followed by a discussion of the results.

4.1 Method Of System Operation/Experimental Setup

In order to characterize the μ-ElFFF systems, an experimental setup with five main components was used. These components were

1. A syringe pump-to flow the carrier fluid and samples through the devices
2. A sample injector-to introduce sample components into the channel
3. A microscope-to enable viewing of device operation and optical detection of sample components
4. Electronic devices-to provide detection signal and signal measurement and recording
5. A desktop PC-to facilitate digital data capture, storage and analysis and to control electronic devices

These five components were successfully used in various combinations and configurations to perform all the experiments required for characterization of the μ-ElFFF systems.

Syringe Pump

For this work, a syringe pump (KDS 100, KD Scientific, Holliston, MA) was used to flow the carrier solution (e.g., DI water) through the system under test at various flow

rates and with various syringes. Flow rates ranged from 0.01-9.0 mL/hr (0.06-0.17 cm/s) with an accuracy of ±1% per manufacturer's data sheet. Plastic syringes (BD Luer-Lok™, Becton, Dickinson and Company, Franklin Lakes, NJ) with volumes of 1, 3, 10 and 30 cc were used as they were less prone to leakage than all-glass syringes at the lower flow rates.

The syringes held the carrier fluid, which for this work was usually DI water. The pump was set to deliver the carrier fluid through the μ-ElFFF systems at a fixed rate, and was left running between runs to help prevent electrolysis within the channels due to the applied voltage on the main electrodes (that provided the electric field for the separations) and that on the AC detector. In general, the former contributed more to electrolysis since a steady DC voltage was applied to the electrodes. In contrast, the signal maintained at the detector electrodes was completely or mostly composed of an AC voltage.

The choice of flow rates was important because low flow rates enable high-resolution separations to be performed. This is mainly a result of the analytes being subjected to the electric field for a longer period of time, but also because the sample components are given more time to reach equilibrium. However, if the flow rate is too low, axial diffusion begins to negatively affect the resolution. High flow rates can also yield low resolution, but are useful for fast analyses. For each system, optimal resolution and analysis time can be achieved by using the flow rate that corresponds to the lowest plate height. Therefore, for each of the μ-ElFFF systems developed, the plate heights as a function of carrier fluid velocity were determined.

Sample Injection

There are several factors related to sample injection that should be addressed in order to realize the greatest efficiency when performing separations in the μ-ElFFF systems.

Method

Figure 4.1 shows that the method of sample injection can affect the plate height.

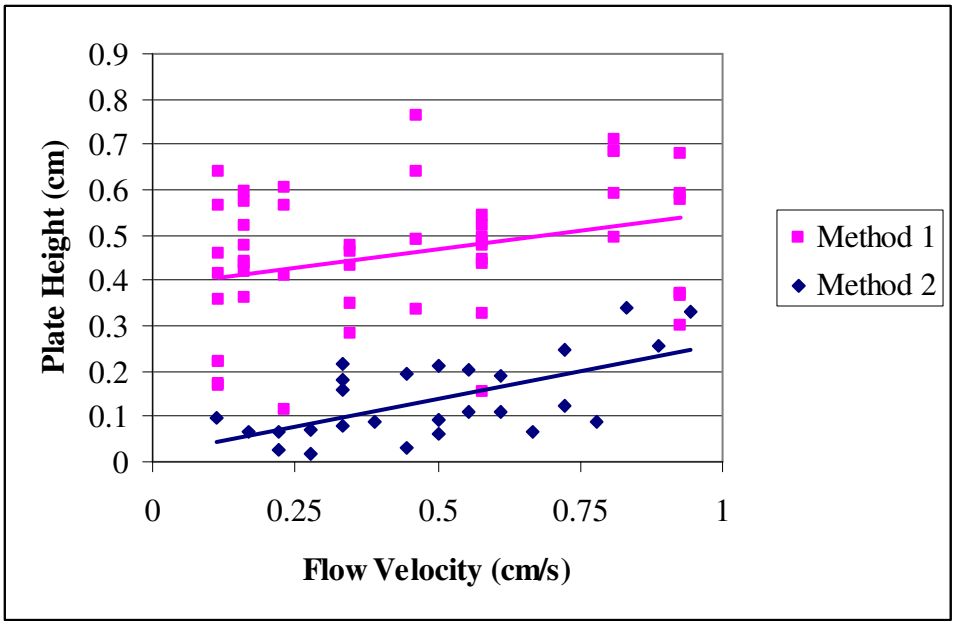

Figure 4.1: Graph of plate height versus flow velocity for two different sample injection methods in a μ-ElFFF system with a channel height of 5.0 μm

For the plate height tests, the sample was 1 M NaCl and there was no voltage applied to the main electrodes. Tests were performed at various flow velocities and the plate heights were calculated using MATLAB (Appendix B). The code was modified according to the specific channel that was under test, as the calculation of theoretical plate heights requires the use of the length of the channel and the calculation of the flow velocities depends on the cross-sectional area of the channel.

The two configurations for sample injection that are represented in the graph in Figure 4.1 are shown in Figure 4.2.

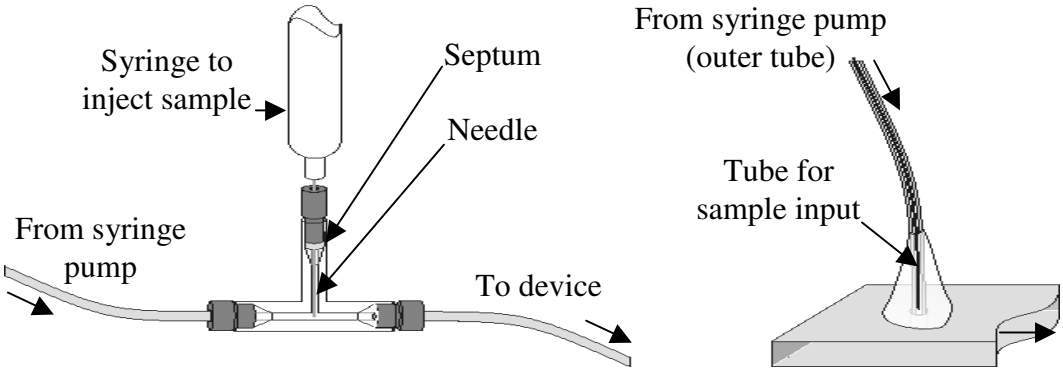

Figure 4.2: Configurations of two sample injection methods where (l) the sample is injected into a "T" connector through which the carrier fluid flows that carries it to the μ-ElFFF system; and (r) where a small tube is passed through a larger tube. The sample passes through the small tube directly to the channel entrance, while the carrier fluid flows through the larger tube.

Plate height tests show that if the sample is injected at the beginning of the channel, which is also the beginning of the electric field for the μ-ElFFF systems tested, then the plate height is greatly reduced. The reduction in plate height occurs because the sample plug has less time to diffuse axially if injection occurs at the channel entrance. Gale demonstrated similar results [62]. Plate heights can be further reduced by minimizing dead volumes and areas where the flow may become turbulent (e.g., abrupt junctions at tubing connection points).

Speed

The speed at which the sample plug is introduced can also affect the measured plate height. To minimize the impact of human error on the plate height measurements, electronic sample injection valves or constant rate syringes can be used. The electronic valves have the extra benefit of being controllable via computer software. This feature

enables the injection of the sample at a more precise time than if directly controlled by a human, as in the case of a constant-rate syringe. Unfortunately, electronic injection valves usually have a sample loop to define the volume of the sample plug and as a result, are placed upstream of the channel entrance. In contrast, the needle of a constant rate syringe can be placed at the entrance of the channel. Therefore, for all experiments, a constant-rate syringe (CR-700-20, Hamilton Co., Reno, NV) was used to inject 0.05-3.0 μL of sample solutions, with concentrations as low as 1.08 pM, into the input port of the μ-ElFFF channels.

Volume

For any separation to occur in μ-ElFFF systems, the volume of the sample plug needs to be much smaller than the volume of the channel. For instance, sample volumes of 1 μL could easily be used in the channels with a height of 150 μm (volume=93 μL), whereas for the smaller channels with a height of 5 μm (volume=0.31μL), even sample volumes of 0.1 μL were relatively large. If the sample volume is too large, no separation will be detectable.

Concentration Effects

The concentration of the sample components should be taken into consideration when performing separations in μ-ElFFF systems. Problems can arise if the concentration of individual sample components is too high or too low.

First, the amplitude of the electrical detection signal increases with increasing concentrations of analytes. Therefore, if two sample components have retention times that are close enough, the peaks may blur together. High concentrations also create problems with optical detection since the overlapping of particles makes determination of concentration based on particle counting less accurate. Intensity measurements will also become nonlinear with respect to particle concentration.

In contrast, if the sample components have a low concentration, the electrical detector will not respond to the analytes and detection can only be accomplished through optical detection. The fact that individual particles can be seen using RLS technology, allowing detection of low concentrations of analytes, is one of the major benefits of using optical detection with the μ-ElFFF systems. The RLS Particles™ used for testing the μ-ElFFF systems had diameters of 40-, 60-, and 80-nm and concentrations of 1.08, 4.32, 8.63, 17.27, 34.54, and 51.81 pM (or, 0.0625-, 0.25-, 0.5-, 2.0- and 3.0-OD respectively).

Device Placement on Microscope and Preparation for Testing

Another major component that was used for the integration of optical RLS detection with the μ-ElFFF systems was a modified, bright field microscope (Micromaster™ I Series, Fisher Scientific Co., Pittsburgh, PA) (Figure 4.3). In order to perform RLS detection, the sample must be illuminated at an angle. To achieve this, a

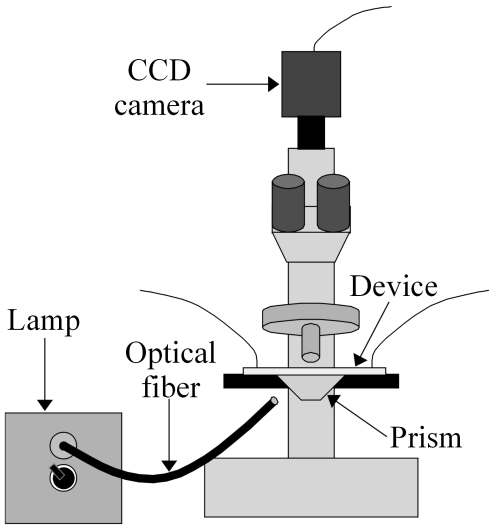

Figure 4.3: Optical setup for testing the μ-ElFFF systems, showing the location of the prism that is integrated into the microscope stage.

custom-made prism was mounted to the bottom side of the stage. The end of a fiber optic light guide was placed perpendicular to one side of the prism. The light source for the fiber optic was a 150-watt, tungsten halogen bulb (Imagelite™ Model 20, Lite Mite Series™, Stockeryale Inc., Salem, NH).

To minimize light scattering by scratches or defects on the top surface of the prism or the bottom surface of the μ-ElFFF systems, a drop of immersion oil (Type FF, R. P. Cargille Laboratories, Inc., Cedar Grove, NJ) was placed on the stage prior to positioning of the μ-ElFFF system. Both surfaces of the μ-ElFFF systems were cleaned using a commercial glass cleaner before being placed on the stage.

Once the system was in place, the stage was positioned so that either a window in the main electrode or the region around the detector electrodes was visible through the microscope. The largest magnification that could be achieved was 100X (10X objective + 10X eyepiece). The 40X objective was unusable for the μ-ElFFF systems because of its short working distance (i.e., <1mm).

Electronic Devices

Five different electronic devices were used in order to accomplish separations and detection:

1. A signal generator-to provide an AC signal to the detector electrodes
2. A multimeter-to measure the current between the detector electrodes
3. A color CCD camera-to image the sample components in the channels
4. A power supply-to apply a DC electric potential to the main electrodes
5. A VCR-to record the optical signal from the CCD camera

Only the signal generator and the multimeter were used for each run as the other three devices were used as necessary, depending on the conditions of each individual run.

Signal Generator

The signal generator (33250A, Agilent Technologies, Inc., Palo Alto, CA) was used to provide an AC signal to the detector electrodes. The amplitude of the signal normally ranged from 2.5-7 V_{pp}, with the lower voltages being used for separations in the thinner channels. An increase in the amplitude would result in an increase in the current measured across the detector electrodes, as expected and predicted by Ohm's Law. The frequency used depended on the sample components to be detected. For instance, for polystyrene beads, a frequency of 2 MHz provided a significant change in the current measured between the detection electrodes, whereas for gold RLS particles, the frequency was increased to 100 MHz. In general, an increase in frequency yielded an increase in the measured current. This is likely due to a decrease in the capacitance of the double-layer at the electrode/carrier fluid interface with an increase in the frequency. For the thin channels, a DC offset was used to increase the amplitude of the detected signals. This offset ranged from 0.75 to 2 V, and while it only yielded a slight increase in the baseline value of the current between the detector electrodes, the peak signals due to the sample components were significantly higher than without the offset, providing a larger signal-to-noise ratio in the resulting plots. A possible explanation for this phenomenon may be that the sample components disrupt the increased double layer formed at the electrodes due to the DC potential, thereby reducing the capacitance of that layer, which would in effect create an increase in the potential across the channel and a corresponding increase in the current between the electrodes.

Multimeter

For measuring the AC current between the detector electrodes, a high-precision multimeter (3458A, Agilent Technologies, Inc., Palo Alto, CA) was used. It was necessary to use an instrument that could measure low AC currents with high resolution since the resistance across the channel, when DI water is used as a carrier fluid, was in

the MOhm range. The measured AC currents between the detector electrodes usually ranged from 0.5 to 25 μA, and the resolution of the multimeter is up to 100 pA, enabling sensitive and accurate measurement of the current.

CCD Camera

With the integration of RLS detection into the μ-ElFFF systems, it is necessary to electronically capture the optical data in order to transfer it for storage and analysis. To accomplish this task, a color CCD camera (Model 2222-1040/0000, Cohu, Inc., San Diego, CA) was attached to the body tube of the microscope, enabling the acquisition of the optical signal. The resolution of the camera when used in NTSC mode, according to the manufacturer's specifications, is 460 horizontal TV lines, which was sufficient for distinguishing individual RLS particles in the captured images when using 10x magnification.

Power Supply

A voltage source (E3611A, Agilent Technologies, Inc., Palo Alto, CA) was used apply a DC potential to the main electrodes of the μ-ElFFF systems to create the electric field necessary for performing separations of sample components. In the μ-ElFFF systems, applied voltages higher than about 3.5 V resulted in bubble formation due to electrolysis of the carrier fluid. However, for the systems made with ITO electrodes, the applied voltages could be much higher (>10 V) due to the increased resistance of the electrodes after performing the thermal bonding.

VCR

For recording the optical data from complete separations, a VCR was connected to the CCD camera. The major problem with the recorded signals was that the images from the CCD camera are not time-stamped. Therefore, from the recording, it is not possible to accurately determine the time of injection. To solve this problem, the field of

view was blocked with a filter wheel upon injection of the sample. Nevertheless, the conditions of the experiment are not recorded on the video, requiring some other method to link the video with the experimental data. As a result, analog video was converted and saved in a digital format in order to identify it with its corresponding experimental and measured electrical signal data. This was performed by connecting the VCR to a computer with a video capture card and using appropriate software save the data in digital format.

Computer Software and Setup

A computer running LabVIEW™ (LabVIEW™ 7 Express, National Instruments Corp., Austin, TX) was used to control the signal generator and multimeter parameters (via a GPIB connection) and to digitally acquire and save the measurement data from the multimeter and the CCD camera (via a video capture card). LabVIEW™ was chosen as the program to use because of its versatility. The program that was used to communicate with the instruments and gather and record data for each experiment was quite complex (Appendix A).

Prior to running the program, specific information regarding the experiment to be performed was entered. The information entered included the

- Filename
- Sample type and volume
- Type of carrier fluid and flow rate
- Size and other characteristics of the channel and electrodes
- Applied voltage and current between main electrodes
- Time of sample injection

Other information needed to be entered (prior to running the program) to set the signal characteristics of the signal from the signal generator to the detector electrodes and to set the measurement type (i.e., AC current) for the multimeter.

Upon running the program, the signal generator was set and the output to the detector electrodes was turned on; the measurement mode was set on the multimeter; the measurements of the multimeter were read and recorded digitally; and ten frames of the optical signal from the CCD camera were maintained in memory. The ten images were automatically written over unless the user provided input via the control panel. Upon such input, the first five files in memory would be permanently saved. It is important to note that these images are all time-stamped by the program so that the time they were recorded in relation to the time of sample injection can be accurately determined.

After the runs were completed, one file with all the parameters and all of the recorded electrical data was saved, as were the last ten images for the run, in addition to any that were saved (in multiples of five) by the user as per the method described above. Additionally, the measured data was saved as a graph in *.png format for easy viewing of the results.

Other LabVIEW programs were developed that could be used to gather the information from all experiments into a single file (not the image files) so that the information could be examined using a database program (Microsoft™ Access 2000, Microsoft Corp., Redmond, WA), or to view and sort the multiple *.png files (representing multiple experiments) to determine which experiments to select for further analysis.

4.2 System Characterization

Four items were used for characterization of the μ-ElFFF systems. First, retention parameters for various samples were obtained from each size of system. Second, the plate height for each system was determined. Third, finding the steric transition point for

each system would provide an idea of which size of μ-ElFFF system to use for a given sample, as ElFFF systems are usually operated in normal mode. The fourth item that was investigated was the biocompatibility of the channels with ITO electrodes. The determination of these four items enables a better comparison of the performance of the μ-ElFFF systems developed in this work to those developed by others.

Retention Parameters

As presented and discussed in Chapter 2, retention parameters for each separated sample component can be found from analysis of the separation data. Specifically, the retention parameter (λ) is determined from the retention time (t_r) and the void time (t_0). By combining Equation 2.3 with Equation 2.18, it can be shown that

$$\lambda = \frac{t_0}{6t_r}. \tag{4.1}$$

Sample Types

For the retention parameter experiments, two types of samples, polystyrene beads and gold RLS Particles^{TM}, were used. The polystyrene beads were either uncoated or coated with fluorescin molecules. The diameters of all particles used in the separations ranged from 40-210 nm for the thin channels and up to 9.91 μm for the larger channels.

Experimental Details

The flow rate and the applied voltage determine the retention time of a sample. Therefore, two types of experiments were performed. For the first type, the voltage applied to the main electrodes, ranging from 0 to 8.8 V, was varied from run to run (being constant throughout a single run) and the flow rate was held constant for all runs. It is important to note that in most devices, electrolysis occurred at less than 3.0 V. However, for some devices, and especially for the ITO devices, the electrode resistance was high enough that an applied voltage of 11.9 V was reached before electrolysis occurred.

In the second type of experiment, the applied potential remained constant and the flow rate was changed from run to run. Performing experiments using this method has the drawback that not all runs are run at the flow rate that corresponds to the lowest plate height, so the resolution of the system becomes non-ideal for most runs.

For all experiments where a single type of sample was used, the sample volume was kept constant. As the method and site of injection can affect the measured retention time, several runs were performed at each flow rate/applied voltage combination.

Experimental Results

Retention parameters for different sizes of gold RLS particles, PS beads and bovine chromaffin cells (~10 µm diameter) were calculated and are shown in Table 4.1. Also shown is the size and type of the channel used for each sample. Figure 4.4 shows two separations of 4.35 µm diameter, fluorescin-coated PS beads that were performed at 0.9 and 1.0 V. The difference in elution times was 81.15 seconds (567 secs vs. 649 secs).

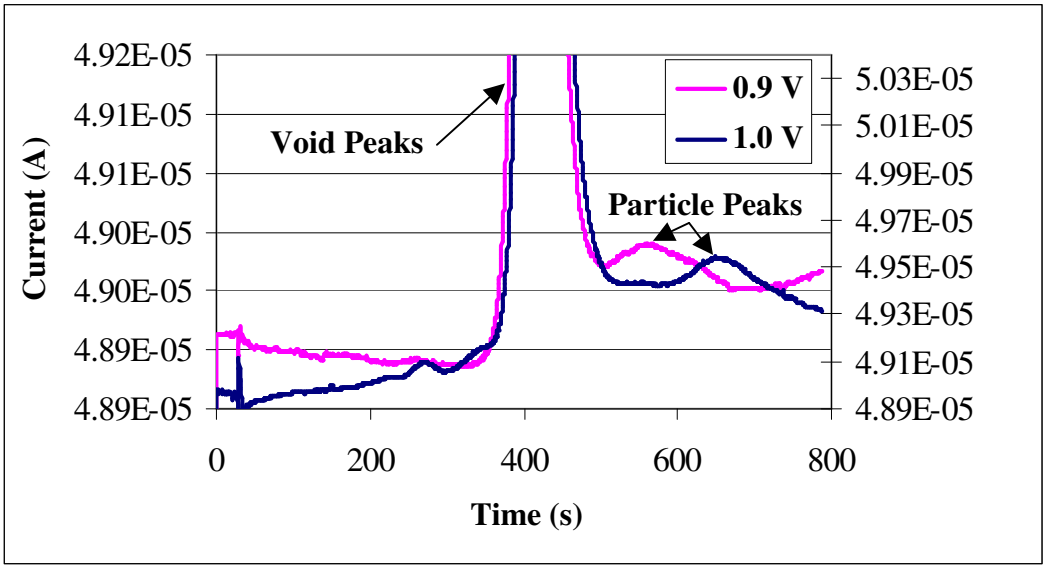

Figure 4.4: Graph from two separations of 4.35 µm diameter PS beads in a µ-ElFFF system at applied voltages of 0.9 V and 1.0 V. (t_{inj} = 30s)

Table 4.1: Retention times of various sample materials separated in μ-ElFFF systems and associated parameters.

Sample Type	Void Time (s)	Retention Time (s)	Retention Parameter	Flow Rate (mL/hr)	Channel Width (cm)	Channel Height (μm)	Applied Voltage (V)	Electrode Material
40 nm gold RLS particles	72.96	112.07	0.109	2	0.5	30	2.45	Ti/Au
60 nm gold RLS particles	72.58	116.03	0.104	2	0.5	30	2.45	Ti/Au
110 nm PS beads	381.59	554.47	0.115	1.6	1.0	150	2.0	ITO
314 nm PS beads	384.21	439.35	0.146	0.05	1.0	150	7.0	Ti/Pt
1.0 μm PS beads	66.91	92.07	0.121	6	1.0	150	1.9	Ti/Pt
4.35 μm PS beads	67.88	110.00	0.103	6	1.0	150	1.9	Ti/Pt
Bovine chromaffin cells in PBS	382.23	1108.49	0.057	0.7	1.0	150	2.5	Ti/Pt

Plate Heights

A van Deemter curve is shown in Figure 4.5. As explained in Chapter 2, the flow rate that corresponds to the lowest plate height should be used to obtain the highest resolution. Therefore, plate height experiments were performed for each system to determine the optimal flow rate for enhanced system efficiency.

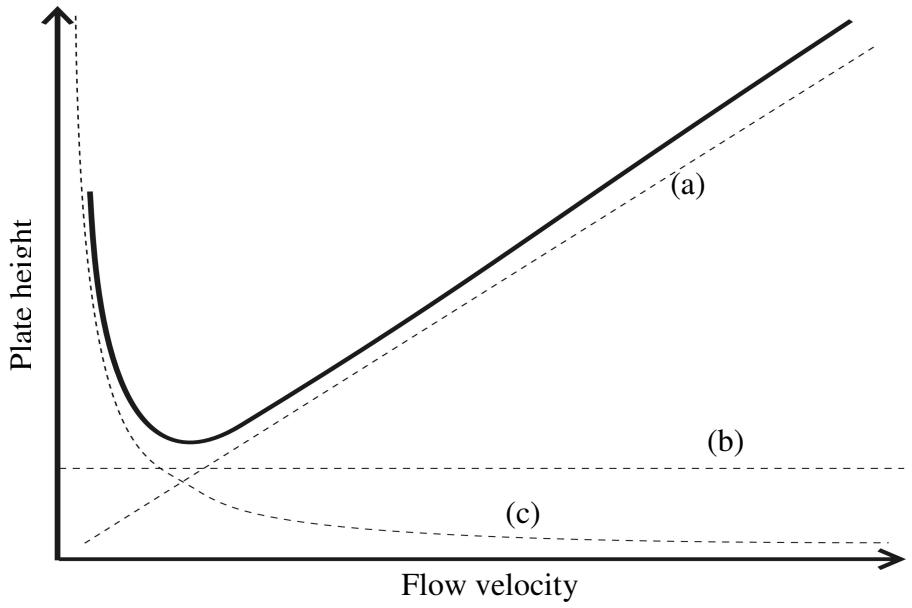

Figure 4.5: A van Deemter plot showing the relative contributions of (a) mass transfer, (b) eddy diffusion and (c) longitudinal diffusion.

Sample Types

For most plate height studies, a sodium chloride (NaCl) solution was used. The concentration ranged from 0.068 to 1.0 M. Early plate height studies were performed

using acetone. Acetone, while easily detected, the signal is not as strong as with NaCl solutions and for the channels bonded with UV glue and SU-8, there was a potential that the solvent could negatively affect the device, through dissolution of the adhesive or through swelling or delamination of the SU-8.

Experimental Details

For each set of studies, the sample volume was constant, and no voltage was applied to the main electrodes. The flow rates for each study covered the range from 0.05 to 1.0 cm/s. To determine the mL/hr rate setting of the syringe pump, the cross-sectional area of the channel (in cm^2) was multiplied by the desired rate (converted to cm/hr).

Once a constant flow was established, the sample was injected and a LabVIEW program (Appendix A) was used to save all the parameters of the run and the detector response versus time to a digital file.

A MATLAB program was written (Appendix B) to extract the plate height data from the digital files. The program performs four tasks. First, the time of the peak relative to the time of injection is calculated. Next, the peak width is determined. Third, the program uses Equation 2.16 and Equation 2.4 from Chapter 2 to calculate the number of plates and the plate height. The last task performed by the program is to plot the plate height versus flow rate.

Experimental Results

Shown in Figure 4.6 is a graph showing the plate heights for each of the three sizes of channels versus the corresponding flow velocities. The flow rates that were used for most of the high-resolution separations for the channels with heights of 5μm, 30μm and 150μm were 0.2, 2.0 and 5.0 mL/hr, respectively. Each channel was 6.2 cm in length, and the breadths of the channels of 5μm, 30μm and 150μm were 0.1, 0.5 and 1.0 cm, respectively.

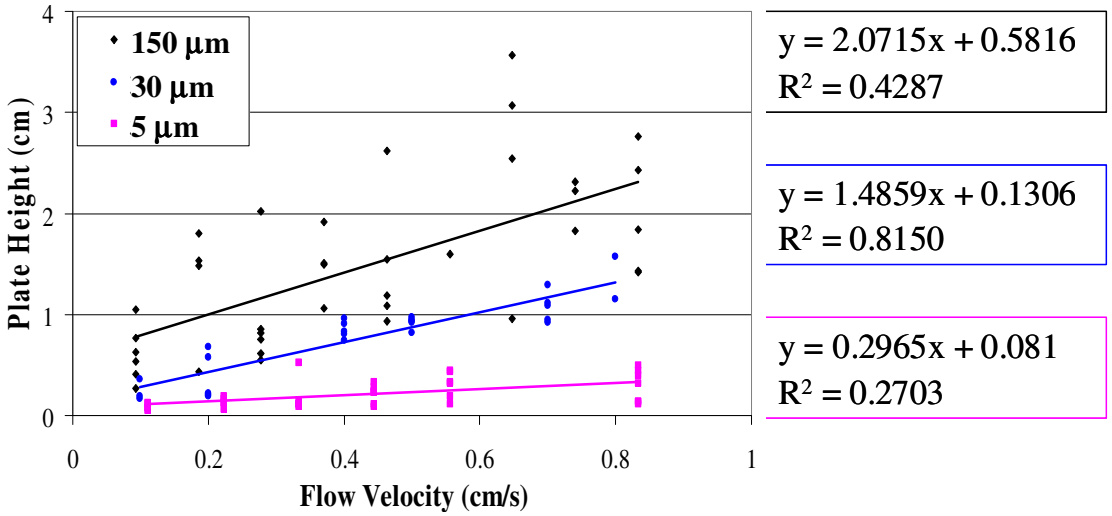

Figure 4.6: Graph of plate height versus flow velocity for µ-ElFFF systems with channel heights of (top to bottom) 150 µm, 30 µm and 5 µm.

Figure 4.6 shows that there is a significant reduction in plate height as the channel height is reduced. The slope of each trendline is determined in part by peak broadening that is a function of the square of the channel height. As a result, the slope of the trendline decreases as the channel height is decreased. It also appears from this data that the thinner channels may provide less variation from run to run, although more data is required for a more conclusive analysis.

Also shown in Figure 4.6 are linear trendlines for each set of data and their corresponding equations. The term that represents the y-intercept is the minimum value of plate height that could be achieved if longitudinal diffusion was not a factor at very low flow velocities (see Figure 4.5). However, at low flow velocities, longitudinal diffusion becomes a major factor and can drastically increase the plate height value. However, in this work, flow rates that corresponded to flow velocities in this region were avoided because they were unnecessary to achieve efficient separations. Additionally, one of the major goals of miniaturization is to reduce analysis times, making the testing of flow velocities lower than those required for satisfactory separations superfluous.

Steric Transition Points

For certain applications and for non-specific types of detection methods, knowing the steric transition point of the μ-ElFFF system can be useful. As discussed in Chapter 2, each system of a particular channel height has a particle size limit above which separations occur in the steric mode. The major characteristic of the steric mode separations is that larger particles are eluted earlier than smaller ones, just the opposite to the case with normal mode separations. If the mode of sample detection is not capable of identifying the sample components independently, and only detects their presence, then the size of analytes of similar composition cannot be determined exclusively based on elution time if the sample components have diameters larger and smaller than the steric transition diameter. By knowing the steric transition diameter, it is possible to ascertain the working mode if the size range of the sample components is known.

Sample Types

For the studies performed to determine the steric transition points for the three sizes of μ-ElFFF systems, particles of various types and sizes of were used. For the μ-ElFFF systems with channel heights of 5 μm, gold RLS particles were used. These particles had diameters of 40, 60, 80 and 100 nm. For the systems with channel heights of 30 μm, both RLS particles and uncoated polystyrene (PS) beads were used. The PS beads had diameters of 65, 110, 210 and 300 nm. Finally, for the systems with channel heights of 150 μm, fluorescin coated polystyrene (PS) beads were used. The coated PS beads had diameters of 1.0, 4.35 and 9.91 μm.

Experimental Details

For these studies, the first step was to use samples of a single size of particles and determine the retention time for a specific flow rate and applied voltage. Once the retention times were found for each size of particle, particles of different sizes were

mixed together and injected into the system while maintaining the same flow rate and applied voltage. The retention time for a specific size of particle will stay constant, making it possible to determine which peak corresponds to which size of particle. From the graph resulting from the separation of a sample composed of various sizes, and knowing the retention times for each size of particle in the sample, it is possible to determine the steric transition diameter if the range of particle sizes used is large enough (i.e., sample components larger and smaller than the steric transition diameter).

Experimental Results

For the μ-ElFFF systems with channel heights of 5μm, the steric inversion point could not be established, as the systems were not capable of significantly retaining any size of RLS particles (Figure 4.7). The μ-ElFFF systems with a channel height of about 30 μm were able to show some retention of 100 nm RLS particles, but not of 80 nm particles (Figure 4.8). The graphs show that 100 nm particles are more retained than 80

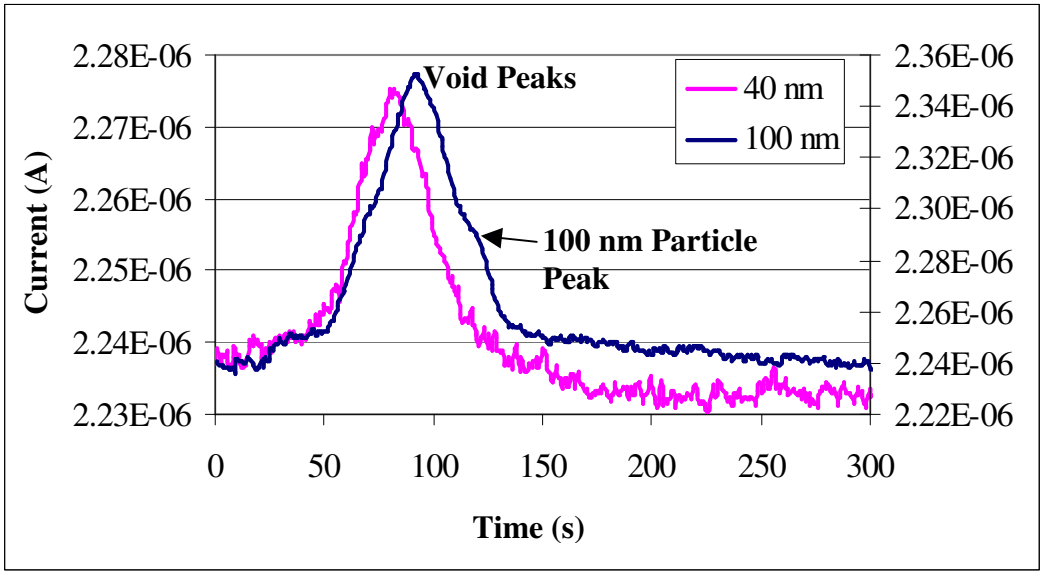

Figure 4.7: Graph showing (on left axis) fractograms for 40 nm and (right axis) 100 nm gold RLS particle separations in a μ-ElFFF system. (t_{inj} = 15s)

nm particles, signifying that the system is still operating in normal mode when the particles are less than 100 nm.

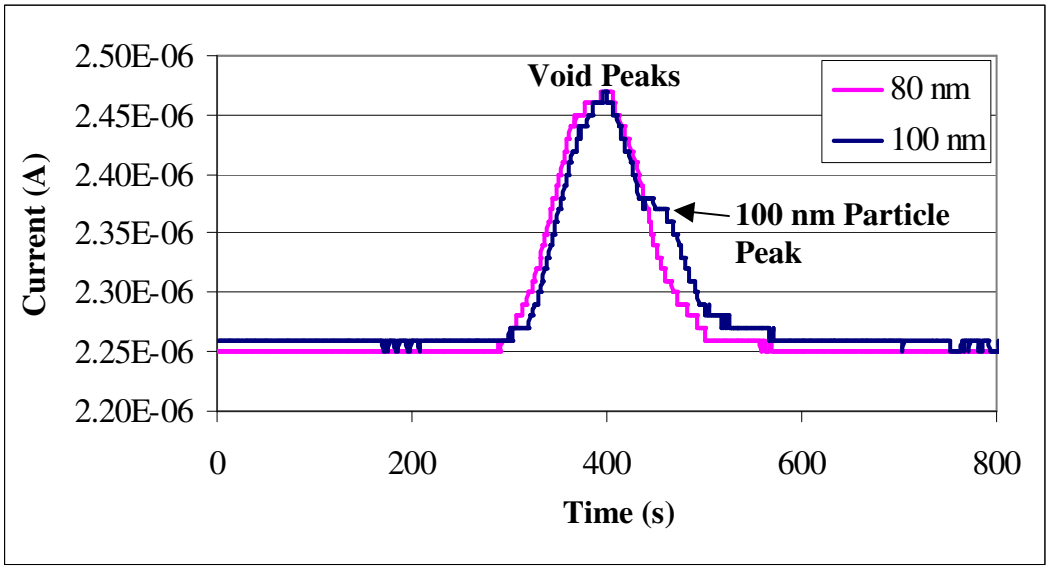

Figure 4.8: Fractograms of 80 and 100 nm gold RLS particles separated in a µ-ElFFF system. (t_{inj} = 15s)

For testing diameters greater than 100 nm, PS particles were used. Unfortunately, the system was not able to retain the larger particles with sufficient resolution to be able to resolve particles with differences less than about 200 nm, as shown in Figure 4.9, which is a multiparticle separation of 110, 210 and 300 nm diameter PS beads. However, when a mixture of larger PS particles was passed through the system, a shorter retention time was noted, indicating that components in the sample mixture had diameters larger than the steric inversion point (Figure 4.10). Finally, for the µ-ElFFF systems with channel heights of 150 µm, greater retention was shown for larger diameter (9.91 and 4.35 µm) PS beads coated with fluorescin than for smaller 1.0 µm diameter beads of

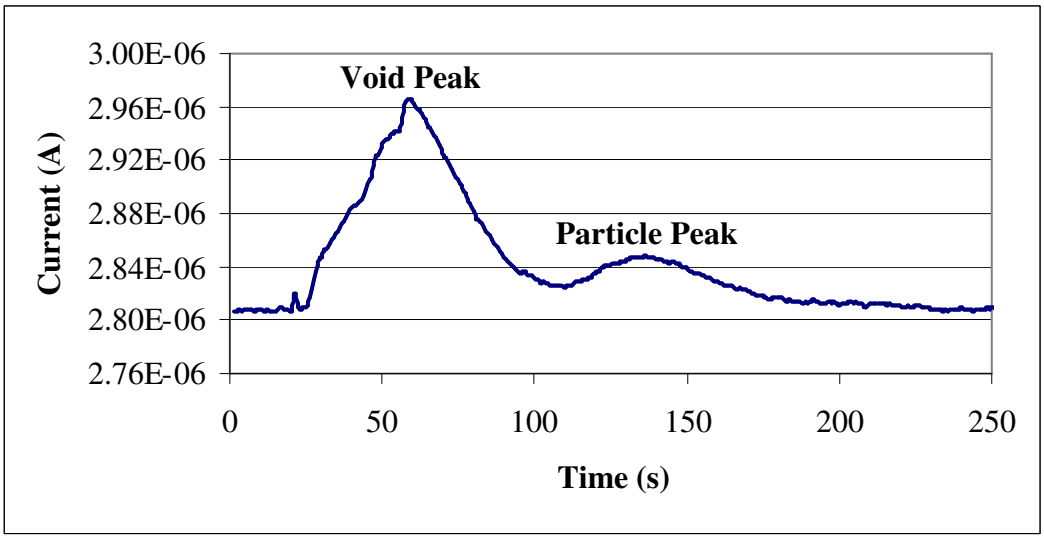

Figure 4.9: Fractogram of a multiparticle separation of 110, 210 and 300 nm diameter PS beads. (t_{inj} = 15s)

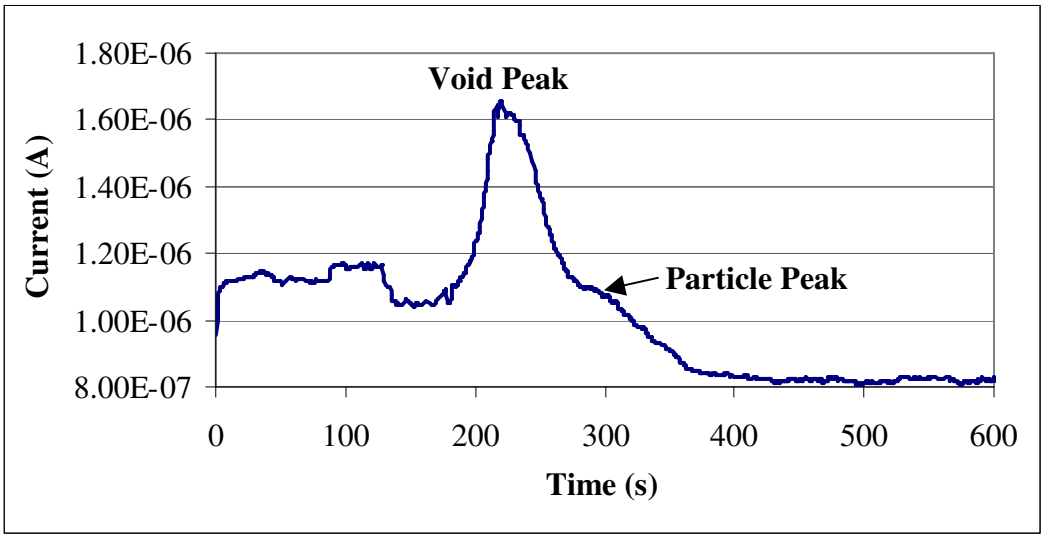

Figure 4.10: Fractogram of a multiparticle separation of 1.0, 4.35 and 9.91 µm diameter PS beads. (t_{inj} = 15s)

similar composition (Figure 4.11). This result is expected for normal mode, indicating that the steric transition diameter is larger than 4.35 µm and may be larger than 9.91 µm.

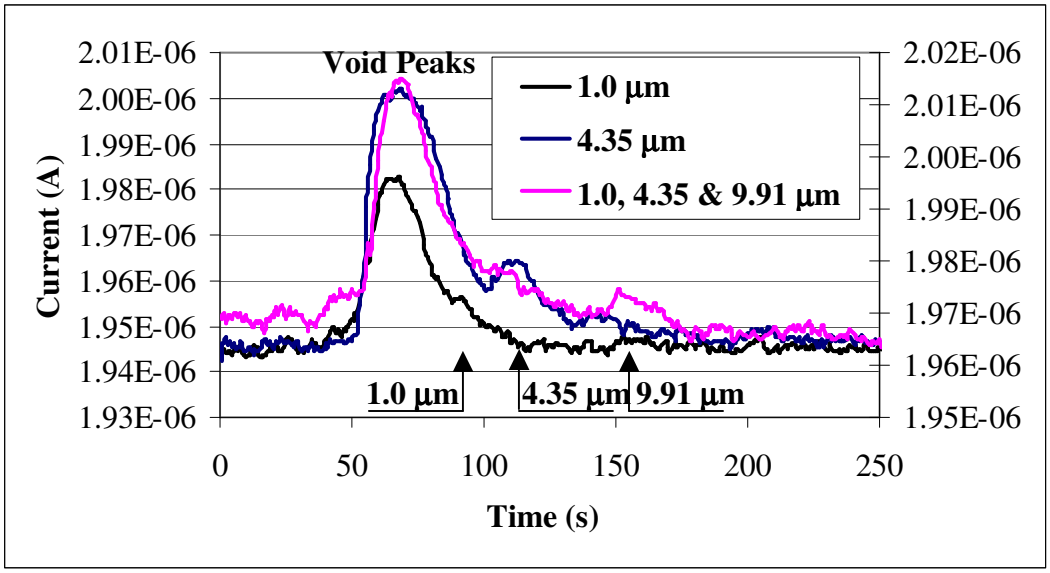

Figure 4.11: Fractograms of (left axis) single and (right axis) multiparticle separations of 1.0, 4.35 and 9.91 µm diameter fluorescin-coated PS beads. (t_{inj} = 15s)

Biocompatibility Testing (Qualitative)

Qualitative testing for biocompatibility of the µ-ElFFF systems was performed to indicate their potential usefulness for biomedical applications, as the biomedical field already represents a large market for microfluidic systems and devices, and is still experiencing significant growth as discussed in Chapter 1. The biocompatibility of glass, gold and platinum is well established, but the use of ITO in direct contact with biological components is not common, so the biocompatibility of ITO is still uncertain.

Sample Types

To test the μ-ElFFF systems and ITO for the degree of biocompatibility required for separations of cells and cellular components in μ-ElFFF systems, bovine chromaffin cells and human breast cancer cells were used. The cells had diameters of approximately 10 μm, and had been cultured for 1-2 days prior to use.

Experimental Details

Two experiments were performed. First, the effect of ITO on human breast cancer cells was examined. To accomplish this, the first step was to remove the cells from the culture media and wash them using phosphate buffered saline (PBS). Next, the cells were stained with a viability stain (trypan-blue) and injected into the channel. With the μ-ElFFF system on the stage of microscope with UV illumination, the carrier fluid (either PBS or DI water) was pumped through the system until the cells were seen between the ITO electrodes. The flow was stopped and after the cells had settled, making contact with the ITO, they were imaged at various times over a period of 20 minutes. This is a sufficient amount of time as most separations in μ-ElFFF systems are much less than 20 minutes.

The second test was to perform a separation with a DC voltage applied to the main electrodes using fluorescently dyed chromaffin cells (S7575, Invitrogen Corp., Carlsbad, CA) and then examine the cells after they exited the system. Following extraction, the fluid with the cells was placed on a glass slide and viewed under UV illumination to search for living cells.

Experimental Results

Figure 4.12 shows pictures of a human breast cancer cell flowing into a μ-ElFFF channel with ITO electrodes and stopping to rest on the bottom electrode. The cell remained viable for over 20 minutes. Separations of chromaffin cells in μ-ElFFF systems

were successfully performed, as shown in Figure 4.13. Pictures of cells during and after the separations were obtained and are shown in Figure 4.14. Due to the extremely low concentration of the cells upon elution, it was difficult to locate them for visualization. It appears, however, that the cells remained viable during and after the separation.

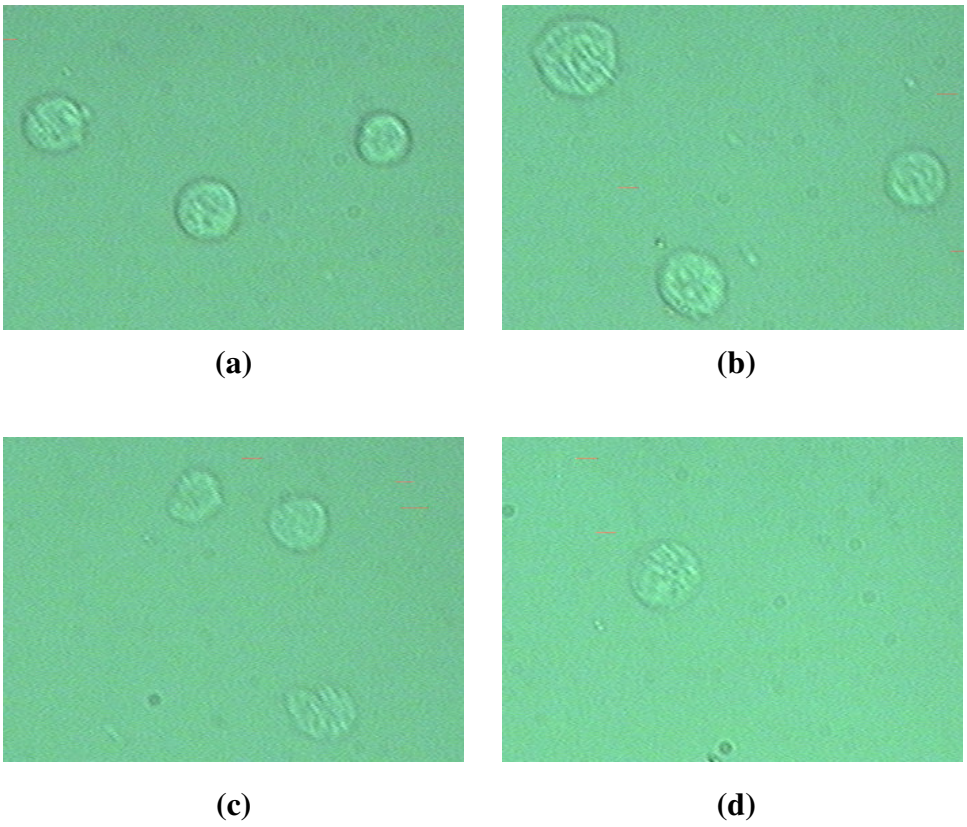

(a) **(b)**

(c) **(d)**

Figure 4.12: Photos of bovine chromaffin cells (a) before and (b-d) after μ-ElFFF separations at different applied potentials and resulting currents of (b) 0.0 V, 0.0 μA; (c) 1.5 V, 142 μA; and (d) 4.5 V, 3700 μA. The photos were taken at 5X magnification.

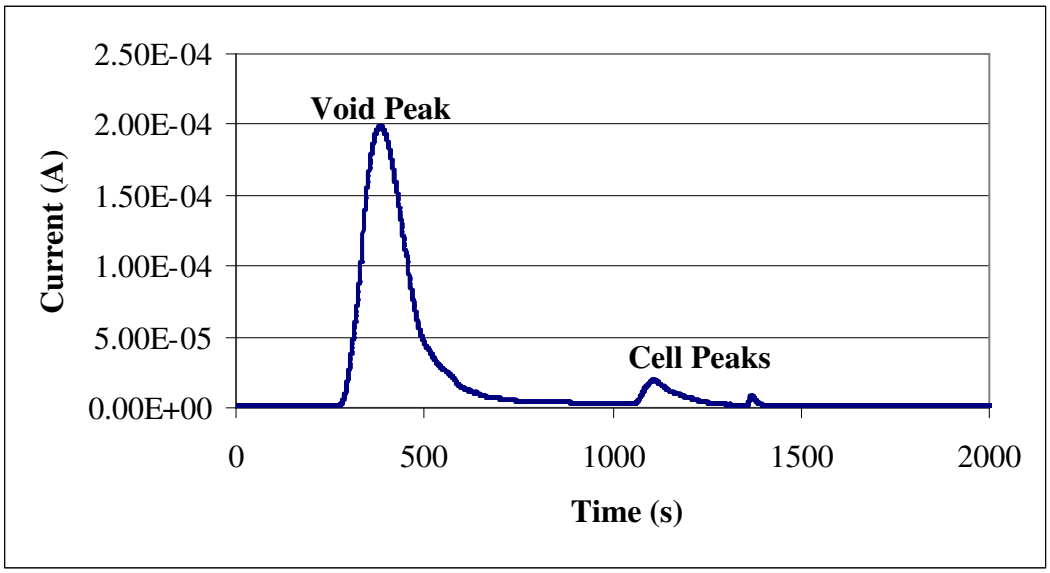

Figure 4.13: Graph resulting from the separation of bovine chromaffin cells in a μ-ElFFF system. (t_{inj} = 30s)

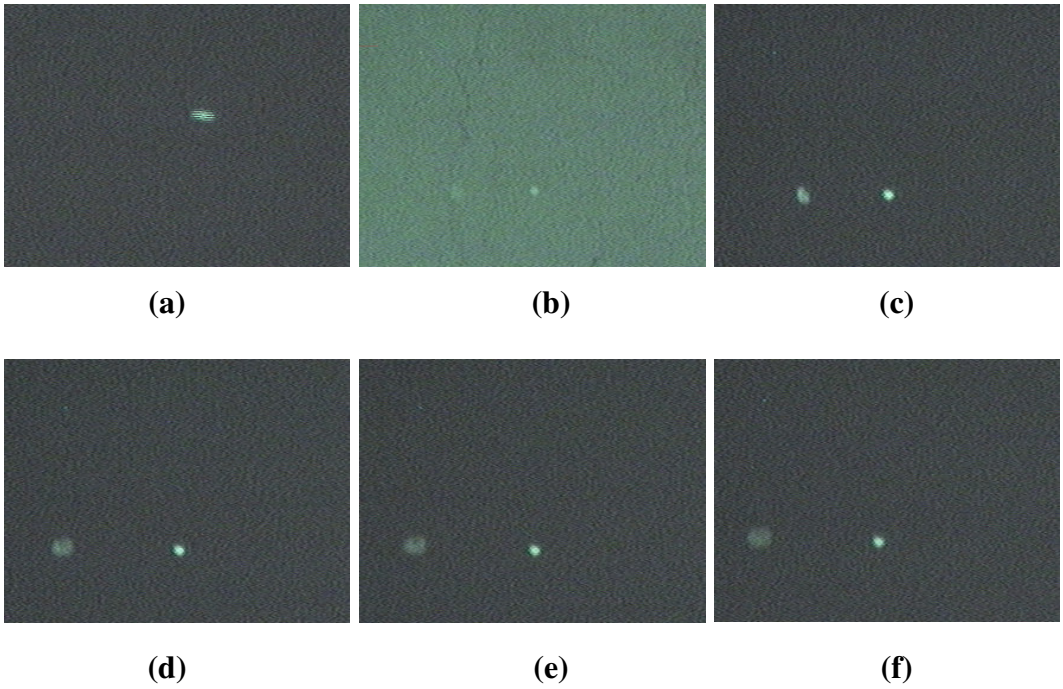

Figure 4.14: Images of human breast cancer cells in a μ-ElFFF channel with ITO electrodes showing a cell (a) flowing and then (b-f) stopped and resting on an ITO electrode. In (b), the ITO is visible and appears to have a cracked surface. The cell was imaged at (b, c) 0 minutes, (d) 5 minutes, (e) 10 minutes, and (f) 20 minutes and showed little or no change during the experiment.

4.3 Conclusions

Experimental Setup

For the sizes of μ-ElFFF systems used in this work, the equipment used for testing characterizing the devices was generally sufficient. The syringe pump was used at a flow rate close to its lower limit for the thinnest channels, but still performed well. Using a constant-rate syringe as the method of sample injection yields good results, but is not the ideal method for several reasons. For instance, the flow rate of the carrier solution and the constant-rate syringe is almost never the same, causing a sudden increase or decrease in the carrier flow. Also, the injection site is highly localized, and upon spreading out to cover the breadth of the channel, some resolution is lost. While RLS particles and cells can easily be seen at magnifications as low as 100X, for image capture and analysis (e.g., velocimetry measurements, particle counting), stronger objectives with long working distances (i.e., greater than 1 mm) could be more useful.

System Characterization

Others have developed, tested, and well characterized microscale ElFFF systems with channel heights comparable to the systems with channel heights of 30 and 150 μm that were used for this work. Therefore, the performance of these systems can be easily compared. However, there is not much if any work directly comparable to the μ-ElFFF systems with channel heights of 5 μm developed in this work.

Retention Times

Since the value of the retention parameter is ultimately based on several factors, it is not a constant value for a given sample type. In theory, and as Equation 2.17 shows, the retention parameter can be used to determine certain physical constants. However, because there is uncertainty regarding the effects of the double-layer at the electrode/carrier fluid interface and the distribution of the electric field is unknown, in

ElFFF, the ability to precisely determine the values of parameters like the electrophoretic mobility or charge on a particle remains a major challenge. Nevertheless, the retention parameters for various samples were found using results from each system, proving their effectiveness as particle separators.

Plate Heights

The plate heights of each system for various flow rates were calculated. It is suspected that changes to the injection method could lower the minimum plate height for the μ-ElFFF systems by reducing the instrumental contribution to the plate height, which is likely to become more significant for smaller channel heights.

Steric Transition Points

Finite values of the steric inversion diameters were not determined, but general trends were observed as normal mode and steric mode operation occurred. A wider range of sample sizes and perhaps longer channels would help accurately determine discrete steric transition diameters for each μ-ElFFF system.

Biocompatibility (Qualitative)

The μ-ElFFF systems fabricated with ITO electrodes did not show adverse effects on the human breast cancer cells and the effect of separations on chromaffin cells is still unknown. Interestingly, the human breast cancer cells appeared to remain viable in channels when DI water was used as the carrier solution. This fact is not too surprising since the cells were injected while suspended in a buffer solution (either PBS or culture media). Once in the channel, the diffusion between the DI water and the buffer solution was probably too slow to affect the cells in the buffer solution. Furthermore, the low concentration of cells in the buffer solution likely helped the cells remain viable as there is more buffer solution for a given sample volume with lower cell concentrations.

CHAPTER 5

ELECTRICAL AND OPTICAL DETECTION IN μ-ElFFF SYSTEMS

Compatible detection systems for the micro scale systems are essential components of the overall biochemical analysis system. The detection systems can be either off-chip or on-chip (i.e., integrated). The information obtained from these detection systems can be used to determine discrete chemical and physical properties such as the type and size of the biochemical species, the concentration of the sample, and the electrical characteristics of the sample components (e.g. the electrophoretic mobility and charge density). On-column detection systems are preferable, since they are minimally affected by Brownian diffusion related effects associated with downstream, off-chip detection systems. Direct, on-column, detection within the miniaturized separation device improves the resolution, decreases the band broadening, lowers the plate height, and shortens the overall analysis time. Detection mechanisms (e.g. electrical, optical) can be integrated into the system and the data obtained from each system can be used to elucidate information on the electrical and physical characteristics of a sample.

In the previous chapter, Chapter 3, the development and fabrication of three sizes of micro electrical field-flow fractionation (μ-ElFFF) systems, with complimentary on-column detection systems, was presented. In this chapter, a detailed description of both detection systems will be given, including their various components and their methods of operation.

5.1 Integrated Electrical Detection

The first detection system to be described is the electrical conductivity measurement (ECM) system. The ECM system is an on-chip, on-column detection

method that can be used for detecting several types of sample components, including organic/inorganic particles and biochemicals. The ECM detection is based on changes in the current flow across the channel due to the presence of analytes and the conductivity and electrical permittivity of the sample medium.

Electrode Configuration

As mentioned in Chapter 3, the main electrodes and the approximately 75 μm wide ECM electrodes were defined simultaneously of conductive material (e.g., Cr/Au, Ti/Pt or ITO), with a separation distance of 500 μm from the end of the main electrodes to the center of the ECM traces. This method of fabrication enabled the ECM detection to occur on-chip.

The distance between opposing ECM electrodes was determined by the channel height since the electrodes were located on the top and bottom walls of the channel. Likewise, the length of the ECM electrodes was determined by the channel width, as they were designed to measure the conductance across the entire channel.

Method of Operation

The ECM detection can be performed by applying either a DC or an AC signal; however, for a given voltage, the use of an AC signal reduces the formation of bubbles at the electrodes caused by electrolysis of the carrier fluid. Therefore, for all experiments an AC or an AC signal with a DC offset was used.

The frequency of the AC signal was maintained at a fixed frequency for all experiments, but varied according to the device under test. In general, lower frequencies (2 kHz-500 kHz) were better for detecting a change in conductance across the channel. Higher frequencies appeared to be prone to parasitic capacitance that would distort the peaks and they also corresponded to higher baseline values (Figure 5.1). The type of particles being separated dictated the frequency used for detection. For instance, a

frequency of 100 kHz was used for detecting the gold RLS particles, whereas a frequency of 2 kHz was better for detecting the polystyrene beads.

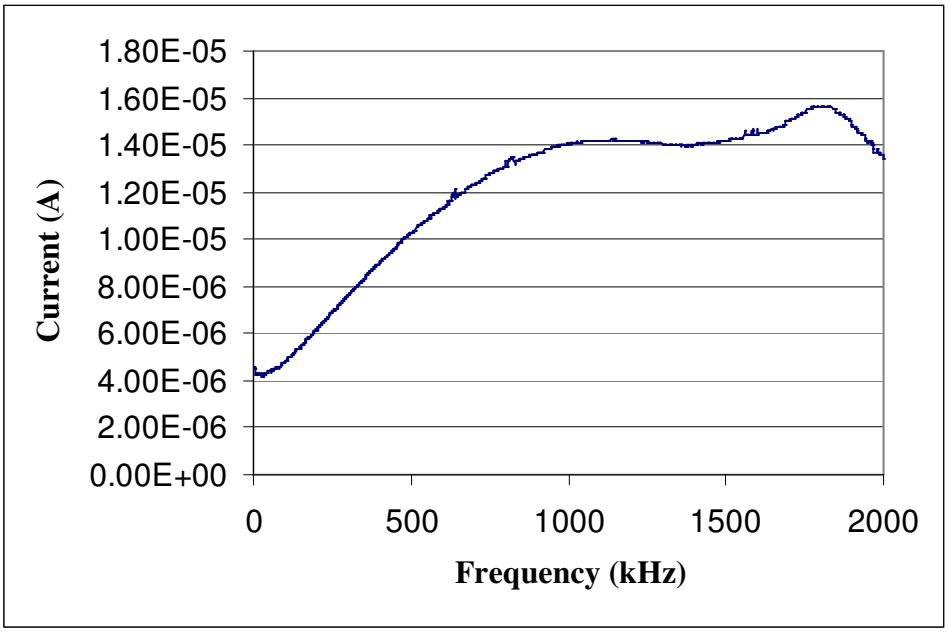

Figure 5.1: Graph showing relationship between the frequency of applied AC signal to the detector electrodes and the resulting current.

A sine wave was used as the waveform for the ECM detection, with the amplitude set to 1.24-1.59 Vrms (3.5-4.5 Vpp) for the 5 µm channel height and to 2.475 Vrms (7 Vpp) for the 150 µm and 30 µm channel heights. Higher values in the 30 µm and 5 µm high channels resulted in electrolysis while little or no detection occurred at low values. Increases in the applied voltage, like increases in the frequency, also yielded an increased baseline value (Figure 5.2).

For some experiments, a DC offset of up to 0.95 V was applied to the detector signal, resulting in an increased baseline and better signal to noise ratios.

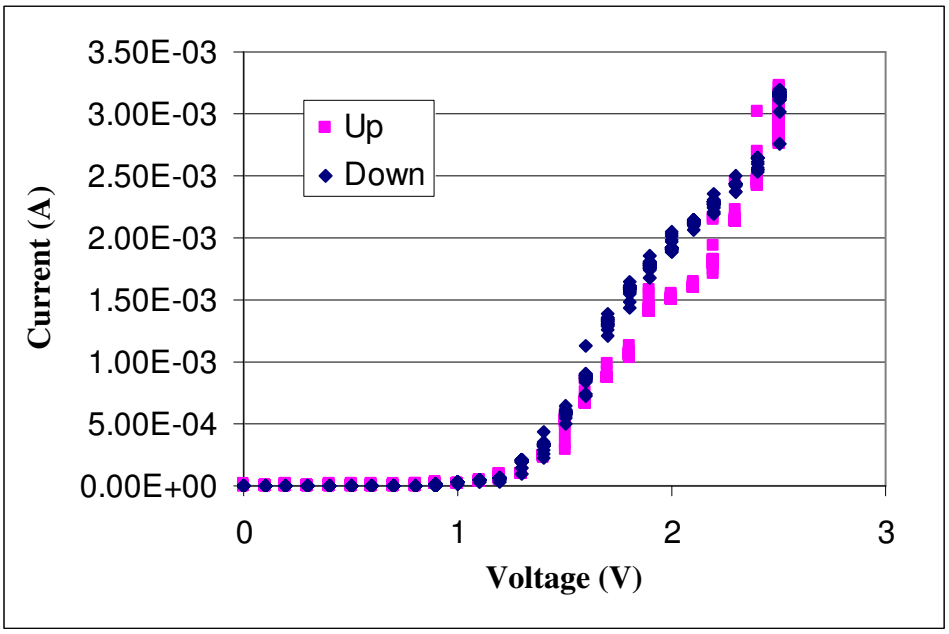

Figure 5.2: Graph showing the relationship between the applied AC voltage and the current between the detector electrodes.

Results

The on-chip electrical detector was used to measure the electrical conductance across the channel during single and multiple particle separations (Figures 5.3 and 5.4). For each of the fractograms from the conductivity detector shown in Figures 5.3 and 5.4, the first peak is termed the void peak [109]. The subsequent peaks represent the change in the conductance across the channel, near the detector electrodes, as the gold RLS particles passed through the detector region. The smaller, 40-nm diameter RLS particles eluted earlier than the 60 or 80 nm diameter particles, which were affected by the field more strongly and therefore traveled at slower average velocities. The width of the peaks was related to the width of the respective particle band, and was affected by several factors including the length of the separation channel, the flow velocity, and the applied voltage.

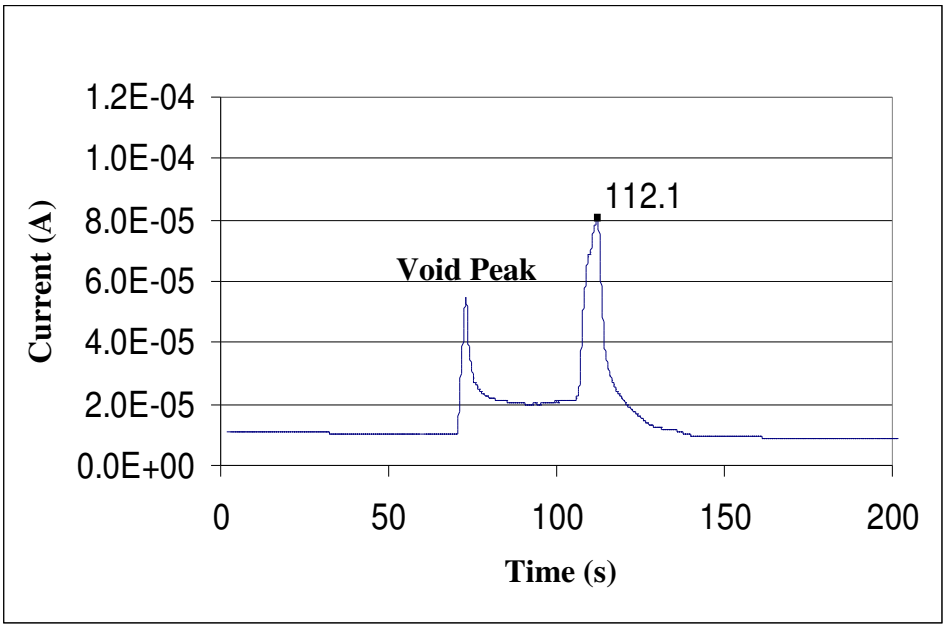

(a)

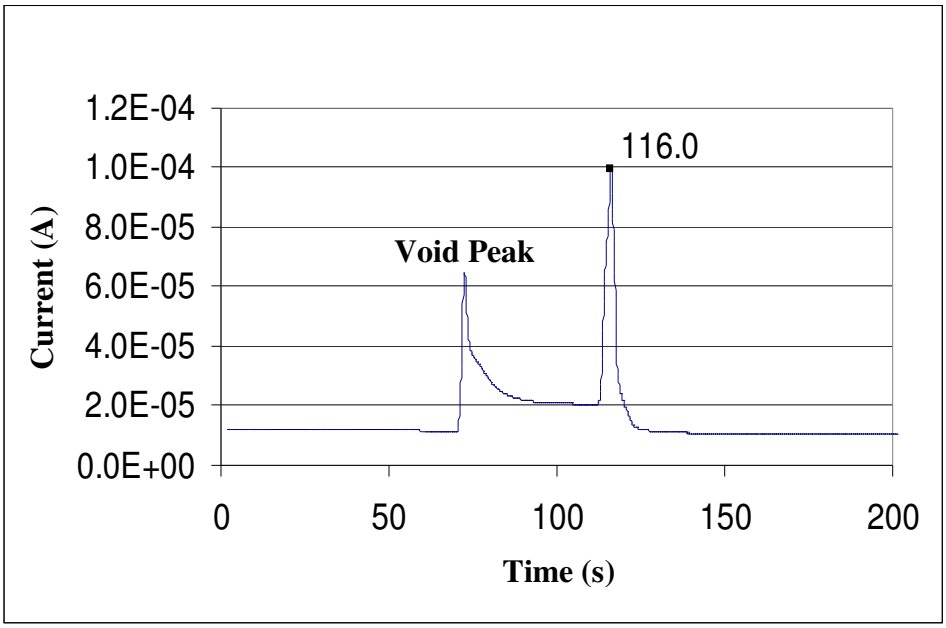

(b)

Figure 5.3: Graphs showing single particle separations of (a) 40 nm and (b) 60 nm gold RLS particles. Samples were injected at 60 seconds.

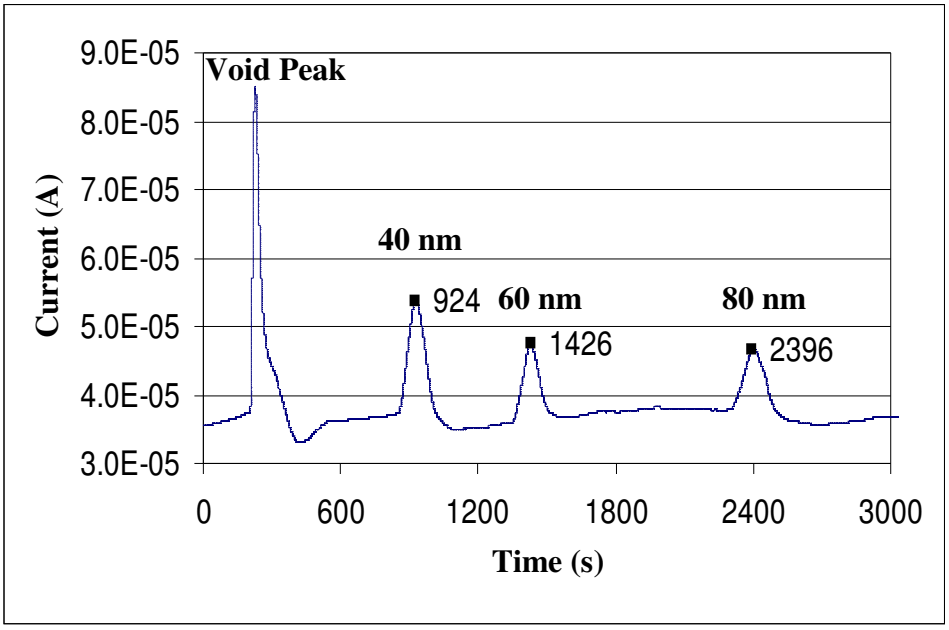

Figure 5.4: Graph showing a multiparticle separation of 40, 60 and 80 nm gold RLS particles. The first peak is the void peak. (t_{inj} = 60s)

5.2 Integrated Optical (RLS) Detection

The second detection system is the resonance light scattering (RLS) detection system for off-chip, on-column particle detection as well as for general flow visualization in micro channels. Using an on-column optical detection scheme with a microsystem has several advantages. The principal advantages of RLS optical detection include being non-invasive, having a high sensitivity for single particle detection, being a relatively low cost detection system, providing real-time monitoring, being complementary to electrical detection (i.e., it can be used as one in a suite of detectors for improved selectivity), and being useful for system characterization (e.g., flow patterns, dispersion/diffusion patterns, sample injection characterization, etc.). In 2001, the use of RLS as an on-column optical detection methodology for μ-EFFF systems was reported as the first demonstration of on-column RLS detection in microsystems [61].

Materials and Optical Setup

As previously mentioned, one of the main reasons glass was chosen as the substrate material for the μ-ElFFF devices was because it is transparent to light in the visible spectrum. This fact is important since both the illuminating light for and the scattered light from the RLS Particles™ have wavelengths in the visible spectrum.

The field of view when using a 10X objective is approximately 3 mm^2, and since the trace width of the ECM electrodes is about 75 μm, optical detection is easily accomplished at the site electrical detection. For optical detection elsewhere in the channel, two options were available. The first option was to fabricate windows within the main electrodes to allow visualization of the channel at discrete points. The second option was to use a transparent electrode material (e.g., ITO) that enabled optical detection at all points along the length of the channel. While both options worked well, the second option was preferred since the ITO electrodes allowed detection of bubbles that formed between the main electrodes as a result of electrolysis of the carrier fluid.

Figure 5.5 shows a diagram of the experimental setup. A color CCD camera (2222-1040, Cohu, Inc.) was used to perform the optical detection. By connecting the camera to a PC, the capturing of digital images using image software (Image-Pro® Plus, Media Cybernetics) was made possible. In order to facilitate the accurate positioning of the camera, a monitor was used, and a VCR was used to record each run in analog format. For each experiment, the μ-EFFF system was placed on a prism that was integrated into the microscope stage [100]. The prism helped reduce the amount of incident light lost due to reflections and surface defects. Immersion oil, used between the prism and the system, further reduced scattered light from defects or other irregularities of the back surface of the systems. Finally, an optical fiber placed perpendicular to the edge of the prism was used to deliver white light from a tungsten/halogen lamp to the focal plane of the microscope.

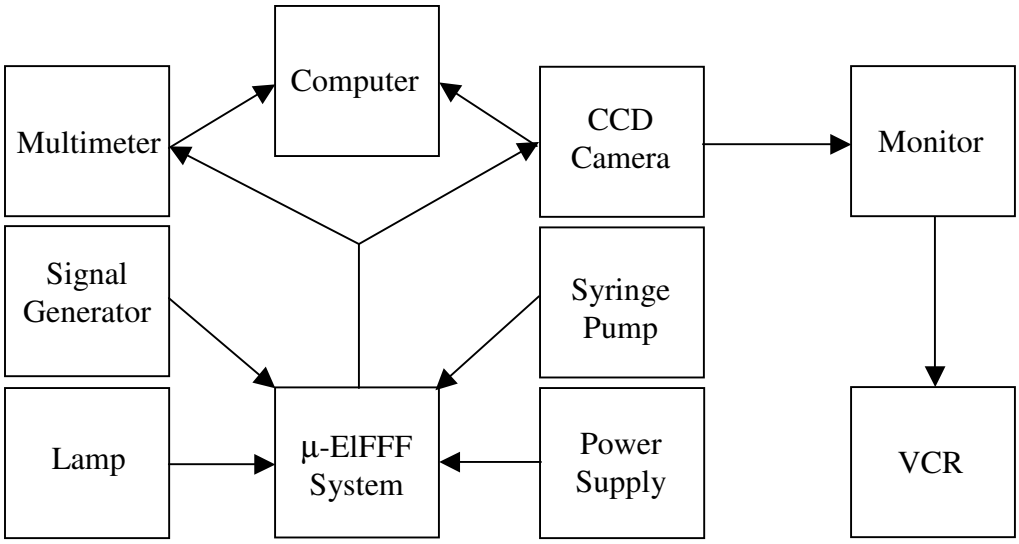

Figure 5.5: Diagram showing the experimental setup. The μ-ElFFF system is on a microscope stage that has an integrated prism to allow illumination from a fiber optic (from the lamp) to pass through the channel at an angle.

Results

The use of transparent substrates and the integration of windows in the driving electrodes or the use of ITO enabled on-column optical viewing of the particles during the separations. The particles were also observed near the electrical detector electrodes, and captured digitally as shown in Figure 5.6. For each image of Figure 5.6, the flow direction is from left to right. The 1.0 μL sample of 80 nm diameter gold RLS particles was injected at 2 seconds and the images were acquired at 3, 15, 16, 18, 22 and 24 seconds. The dimensions of the channel were 150 μm x 1.0 cm x 6.2 cm and the flow rate was 7.0 mL/hr. In each frame, the particles are circled to help distinguish the particles from the background. The main electrode and the detector electrode are labeled in Figure 5.6 (a), with a distance of 500 μm from the end of the main electrode to the center of the detector electrode. The bottom electrodes are visible, a little to the right of the top electrodes, as the substrates were slightly misaligned during bonding.

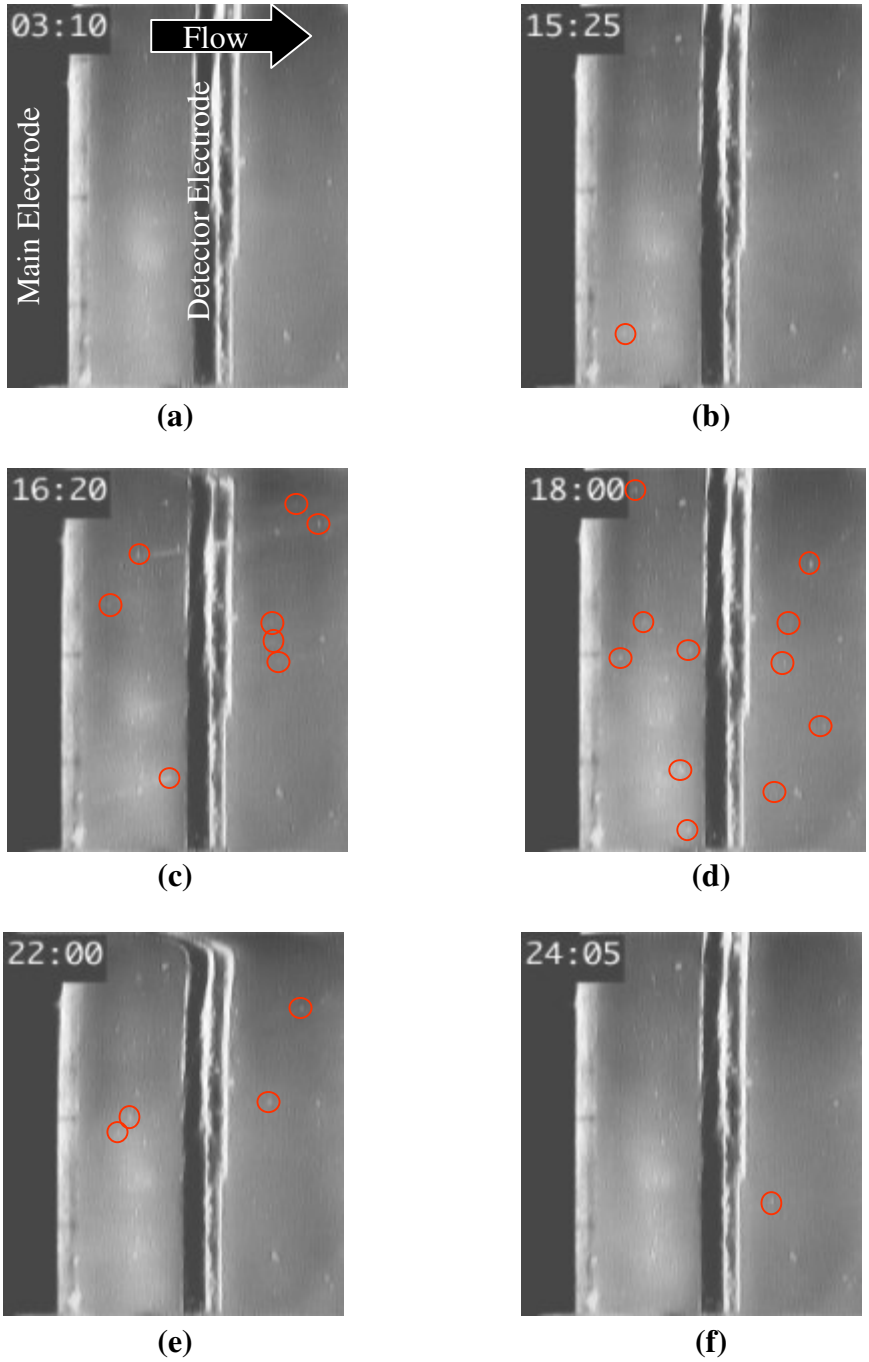

Figure 5.6: Digital images of 80 nm gold RLS particles near detector region of a μ-ElFFF system taken at (a) 1, (b) 13, (c) 14, (d) 16, (e) 20, and (f) 22 seconds after sample injection. The particles are circled for easier identification. Flow direction is from left to right as indicated by the arrow in (a). Main and detector electrodes can be clearly seen in each image and are labeled in (a).

5.3 Conclusions

The experimental results show that the ECM detection system was capable of detecting the particles and that the resulting signal was proportional to the particle concentration. The images obtained from the RLS detection system showed that the particles could be seen clearly, enabling the determination of particle type and size. Finally, as will be shown in Chapter 6, the data from the ECM and RLS detection systems can be compared and a quantitative analysis/correlation may be performed, thereby enabling the independent use of either system.

CHAPTER 6

QUANTITATIVE CORRELATION OF OPTICAL AND ELECTRICAL SIGNALS

The μ-ElFFF systems developed had integrated electrical detector electrodes and were designed and fabricated to enable the use of resonance light scattering technology for optical detection of sample components. In this chapter, the electrical and optical detection methods will be discussed and a quantitative correlation between the electrical and optical signals will be shown.

6.1 Electrical Measurements

Electrical detection in the μ-ElFFF systems was based on a change in the current flow between the two detector electrodes near the end of the fluid channel (see Figure 3.3 (f)) as sample components passed through the area of current flow. Therefore, it was essential to establish a current between the electrodes. This was done by connecting the electrodes to a signal generator as shown in Figure 6.1. To monitor and record the current, a multimeter was connected in series with the signal generator and the electrode.

The output waveform of the signal generator was a sine wave, which provided an AC current to the electrodes. The applied peak-to-peak voltage depended on both the channel height and the sample type, and ranged from 3.5 to 7.0 V. The optimal frequency for detection was dependent on the sample type and, therefore, was set to either 2 kHz for PS beads or to 100 kHz for RLS particles.

The multimeter that was placed in series between the signal generator and one of the electrodes (Figure 6.1) was connected to a PC for data acquisition and for the software to set the measurement mode (i.e., AC current).

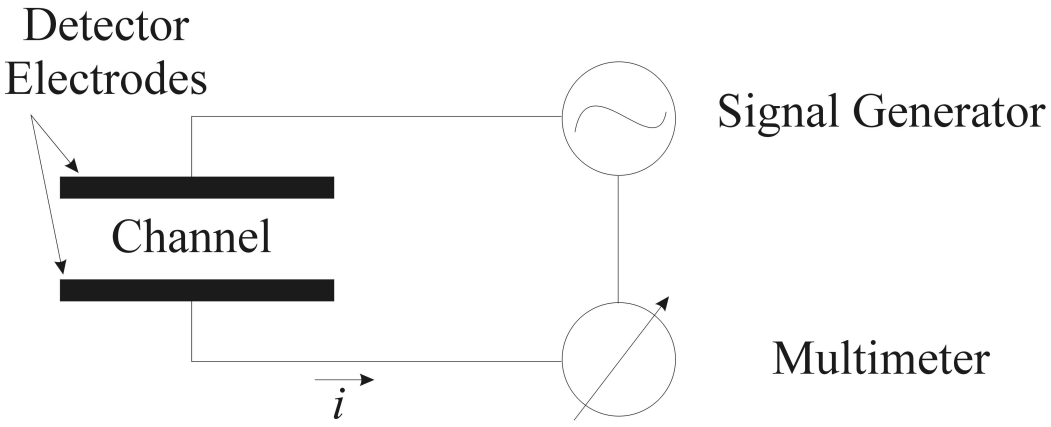

Figure 6.1: Diagram showing configuration of signal generator, detector electrodes and multimeter for on-chip electrical detection in the μ-ElFFF system.

6.2 Optical Signal Detection and Recording

As mentioned in Chapter 3, one of the novel changes made to existing μ-ElFFF systems was that of using transparent substrates, or, more specifically, glass. This design issue was based on the fact that RLS detection requires, as discussed in Chapter 2, that the sample components be illuminated by an incident light that passes through the channel at an angle. Therefore, for the optical detection experiments, the μ-ElFFF systems were placed on the microscope stage with the integrated prism, as shown in Figure 5.6, and the flow through the devices established.

A CCD camera, connected to a VCR and a PC, was mounted to the body tube of the microscope (see Figure 5.5), and was used for the optical detection of the sample components. Digital videos and still images were obtained by one of two methods. In the first method, an analog recording was made using the VCR, and later transferred directly to the PC via the video capture card (PCI-1411, National Instruments Corp.,

Austin, TX). For the second method, the VCR was bypassed by directly connecting the CCD camera to the capture card. Computer software (i.e., LabVIEW™) was used to either capture photos or video of the sample components as they passed through the detector region (Appendix C).

Particles with diameters between 40 and 100 nm were easily and clearly seen at a magnification of 100X with the human eye, and were therefore imaged using a standard, analog CCD camera. For imaging at magnifications greater than 100X, a zoom adapter with a zoom range from 0.9 to 2.25X was used. To facilitate the use of microscope lenses with short working distances, some of the μ-ElFFF systems were fabricated using a thin (~150 μm) glass slide of #1 thickness for the top substrate. The major drawback to such devices was the ease with which the interconnects could break off and render the device unusable. Other drawbacks were that the thinner substrates were easy to damage during fabrication, and the channels could not tolerate high fluid pressures often used to remove air bubbles.

6.3 Analysis of Electrical and Optical Signals

To demonstrate a quantitative correlation between the electrical and optical signals, known concentrations of RLS particles were used for a series of separations. During each separation, the optical data was recorded in a digital format. After a thorough analysis of electrical and optical detection signals, a correlation was noted and quantified.

The samples for all experiments related to the correlation between the electrical and optical signals were gold RLS Particles™ of 40, 60, 80 or 100 nm diameter. Two types of experiments were performed. First, for both electrical and optical detectors, the relationship between the response of the detector and particle concentration was tested. The second type of experiment was to test each detectors response in relation to the size of a given sample type.

Electrical Data Analysis

The on-chip, integrated electrical detector was tested for its sensitivity to changes in concentration and its ability to discriminate between sample components of various sizes.

Electrical Detection vs. Concentration

To test the response of the electrical detector to changes in sample concentration, several concentrations of gold 80 nm RLS Particles™ were used. The detector electrodes were excited using a 100 kHz sine wave with an amplitude of 3.5 Vpp, and the concentrations used for the experiments are listed in Table 6.1.

Table 6.1: Concentrations of 80 nm gold RLS particles.

Dilution Ratio	Concentration (OD)	Concentration (M)
Undiluted	1.0	1.73×10^{-11}
1:1	0.5	8.64×10^{-12}
1:2	0.3	5.76×10^{-12}
1:3	0.25	4.32×10^{-12}
1:4	0.2	3.45×10^{-12}
1:5	0.17	2.88×10^{-12}
1:10	0.09	1.57×10^{-12}

In Figure 6.2, it can be seen that as concentration increases, so does the current measured between the detector electrodes. In this example, a concentration difference of 3.15 pM resulted in a current difference of approximately 0.018 μA for a sensitivity of 0.006 μA/pM. Changes in the current when the overall particle concentrations were lower than 1.57 pM were very small, with a signal to noise ratio near unity.

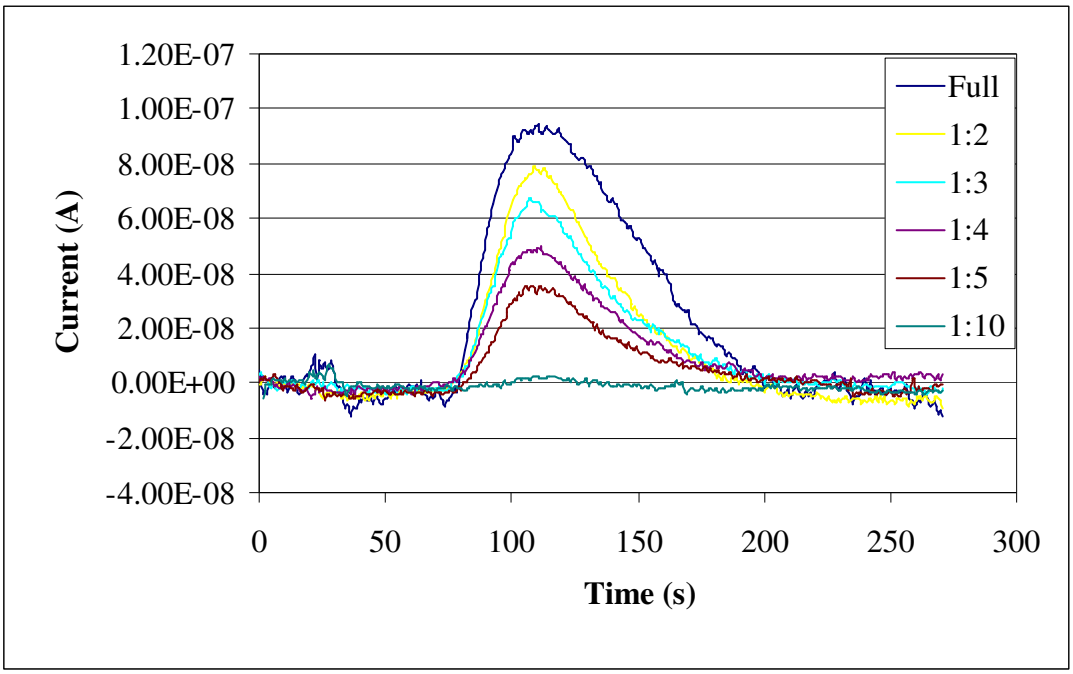

Figure 6.2: Graph of various concentrations of 80 nm gold RLS particles during a separation in a µ-ElFFF system showing the effect of concentration on conductance across the detector electrodes.

Electrical Detection vs. Size

For measuring the response of the integrated electrical detector to various sizes of particles, 1.0 µL samples of 40, 60, 80 and 100 nm RLS Particles™ were injected into the µ-ElFFF channel. The concentrations of each are listed in Table 6.2.

Table 6.2: Concentrations of various sizes of gold RLS particles.

Diameter	Concentration (OD)	Concentration (#/L)	Concentration (M)
40	1.0	7.08×10^{13}	1.18×10^{-10}
60	1.0	2.32×10^{13}	3.85×10^{-11}
80	1.0	1.04×10^{13}	1.73×10^{-11}
100	1.0	6.54×10^{12}	1.09×10^{-11}

The response of the electrical detector to each size of RLS particle is shown in Figure 6.3. As noted in Table 6.2, each of the four sizes of gold RLS particles used for

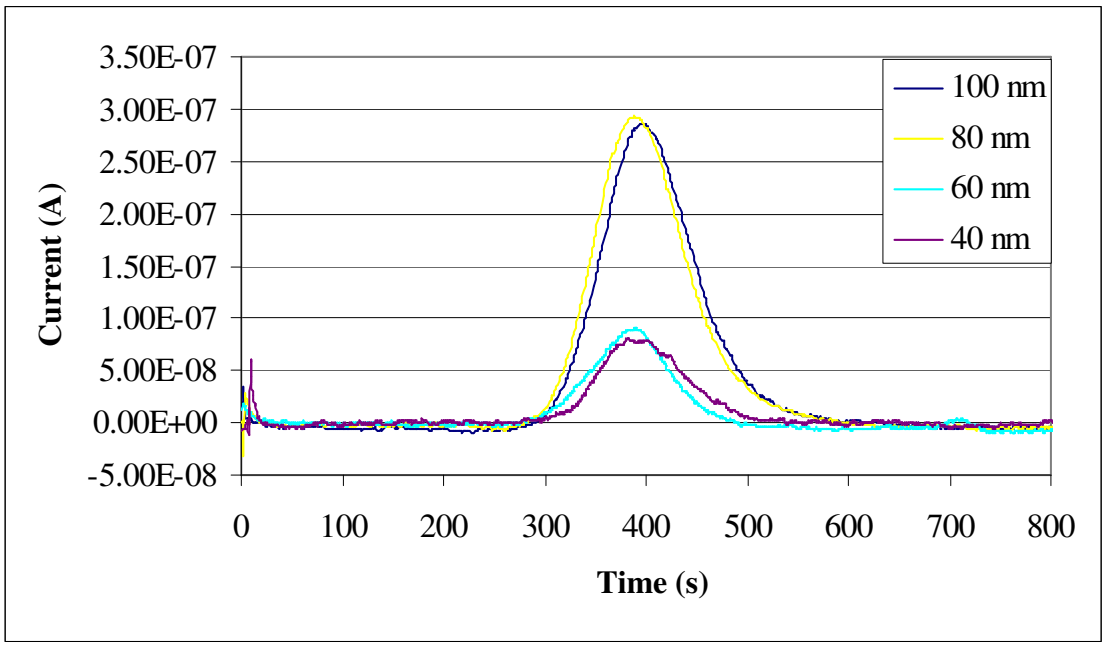

Figure 6.3: Graph of 40, 60, 80 and 100 nm diameter gold RLS particles showing the difference in measured current by the on-chip detector for differences in size. The optical density of all particles was 1.0.

the experiments had an optical density of 1.0. The results demonstrate that the size of particles affects the measured current significantly, with the measured current being higher for larger particles and lower for smaller particles, in agreement with Equation 2.23 and the theory presented in Section 2.5 of Chapter 2. The graph in Figure 6.3 shows that the change in current flow across the channel is approximately the same for 80 and 100 nm diameter particles even though the concentration of the 100 nm diameter particles is about 63% that of the 80 nm diameter particles. A similar relationship is seen between

40 and 60 nm diameter particles. In the latter case, the 60 nm diameter particles have a concentration of about 33% that of the 40 nm diameter RLS particles.

Finally, the experimental results indicate that in order to determine concentrations from the electrical measurements, the size of the particles should be known since similar changes in the current flow across the channel occur with different concentrations of different sized particles. Therefore, it is useful to utilize a second, complementary detection method that can be used to measure both concentration and size. One such method is optical, resonance light scattering detection.

Optical Data Analysis

As a complementary detection method to the on-chip electrical detector, the on-column, optical, RLS detection can be used to verify the response of the integrated detector to various types of sample components. Furthermore, RLS detection is much more sensitive as single particles can be seen. Therefore, in addition to being useful for measuring the size and concentration of a sample, optical detection enables the identification of particle type.

Optical Detection vs. Concentration

The intensity of the light scattered by colloidal solution of is directly proportional to the concentration of the particles if the particles scatter light independently. This condition is met when the distance between the particles is large enough that the waves of scattered light from individual particles do not interfere with each other, and each particle scatters the incident light, not the scattered light from other particles.

To enable quantitative correlation of the optical measurements with the electrical detector response, separations of various concentrations of 80 nm gold RLS particles (as listed in Table 6.1) were performed and relative values of scattered light intensity for the different particle concentrations were obtained (Figure 6.4). Two to four 30-second

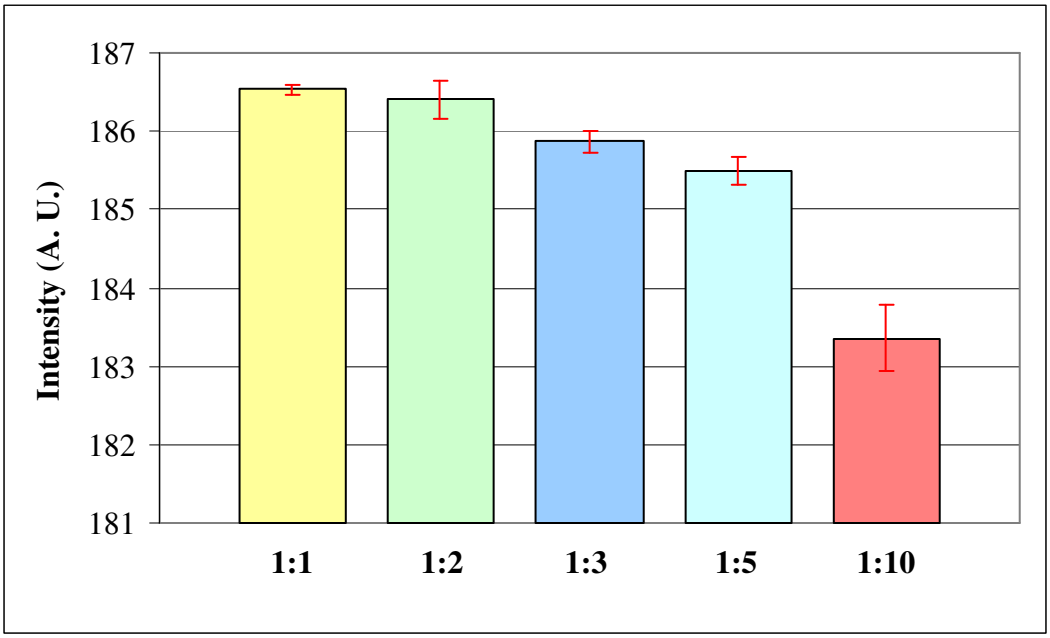

Figure 6.4: Bar graph showing the intensity of scattered light from gold RLS particles as a function of concentration.

sequences of digital video were captured when the response of the electrical detector was maximal (i.e., when the largest number of RLS particles were passing between the detector electrodes). Then, the frames of each video were analyzed individually using a program developed in LabVIEW (Appendix D). For each frame, the program measured the average intensity of a discrete, rectangular area near the detector electrodes. The average intensities of each frame were further averaged and compared, showing that the measured intensity decreases with decreasing concentration (Figure 6.4). This result is in accordance with the theory presented in Chapter 2.

Optical Detection vs. Size

Size can be easily determined through optical detection in one of two ways. First, as discussed in Chapter 2, and shown by Equation 2.25, the intensity of scattered light is proportional to the particle radius raised to the sixth power (intensity $\propto$ radius^6).

Experimental results of separations of 40, 60, 80, and 100 nm diameter gold RLS particles, shown in Figure 6.5, illustrate the large difference in the intensity of the scattered light from such particles. Each sample had a concentration as shown in Table 6.2, and the measured intensity was normalized to the concentrations. Similar to the analysis of the electrical data, individual frames of several 30-second digital videos of each separation that were taken when the electrical current measurement reached its maximal value were analyzed using the same LabVIEW program.

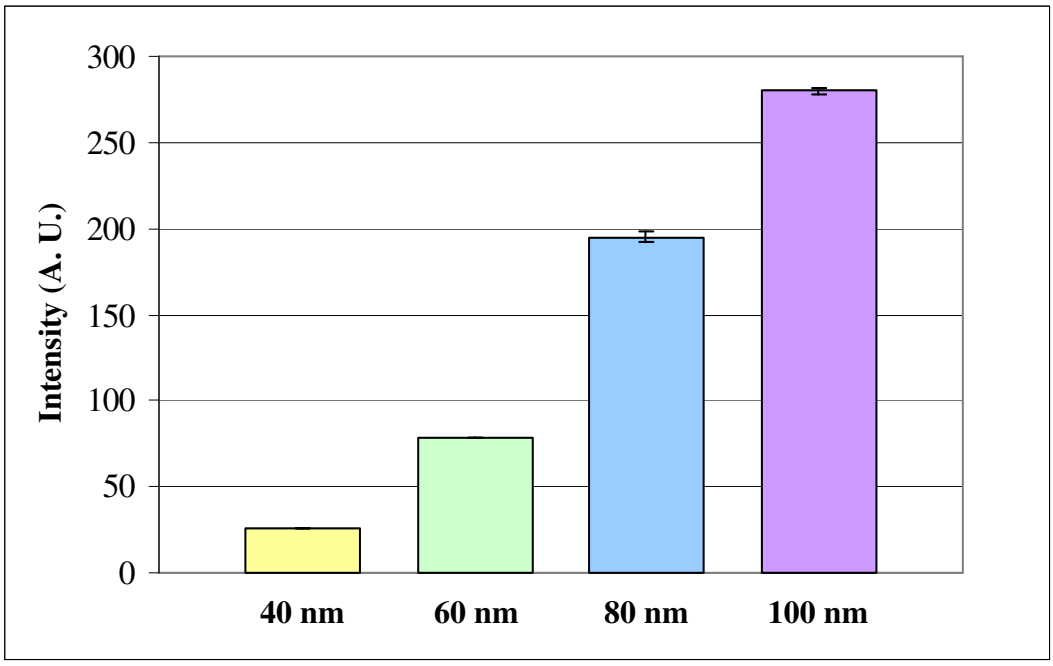

Figure 6.5: Bar graph showing the intensity of scattered light from gold RLS particles as a function of their diameter.

Optical Detection vs. Color

If the composition of the light scattering particles is known, then it is possible to determine the particle size based on the color of the scattered light. The theory regarding

this phenomenon was discussed in detail in Chapter 2. Figure 6.6 shows three images that demonstrate this fact.

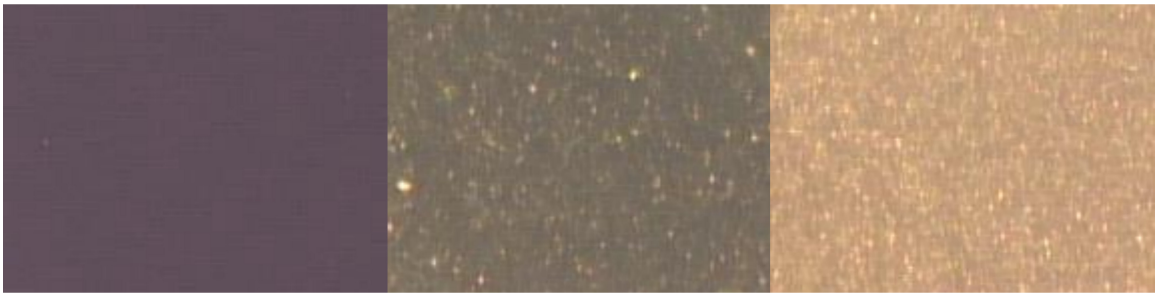

Figure 6.6: Images taken of (left) a droplet of DI water, (middle) a droplet of 60 nm diameter gold RLS particles and (right) a droplet of 80 nm diameter gold RLS particles. Each droplet (2 μL) was placed between glass slides spaced 0.17 mm apart. The concentrations of the 60 and 80 nm diameter particle solutions were 3.85×10^{-11} M and 1.73×10^{-11} M, respectively.

The use of color to determine the composition of the analytes as they passed the detection region was difficult in the μ-ElFFF systems because the spacing between the particles was large (e.g., independent scattering conditions). Under such conditions, it is necessary to use high magnification (e.g., 500X), as several pixels are required to accurately represent the color of the scattered light from a single particle.

6.4 Correlation of Electrical and Optical Signals

The correlation between on-chip electrical and on-column optical detection in the μ-ElFFF systems showed complementary results. As shown in Figure 6.7, the separations were viewed, captured digitally, and recorded on videotape. The collection of the corresponding conductivity measurement data was simultaneously performed on a PC using LabVIEW™ (LabVIEW™ 7 Express, National Instruments Corp., Austin, TX). For each of the images in Figure 6.7, the 80 nm gold RLS Particles™ were flowing from

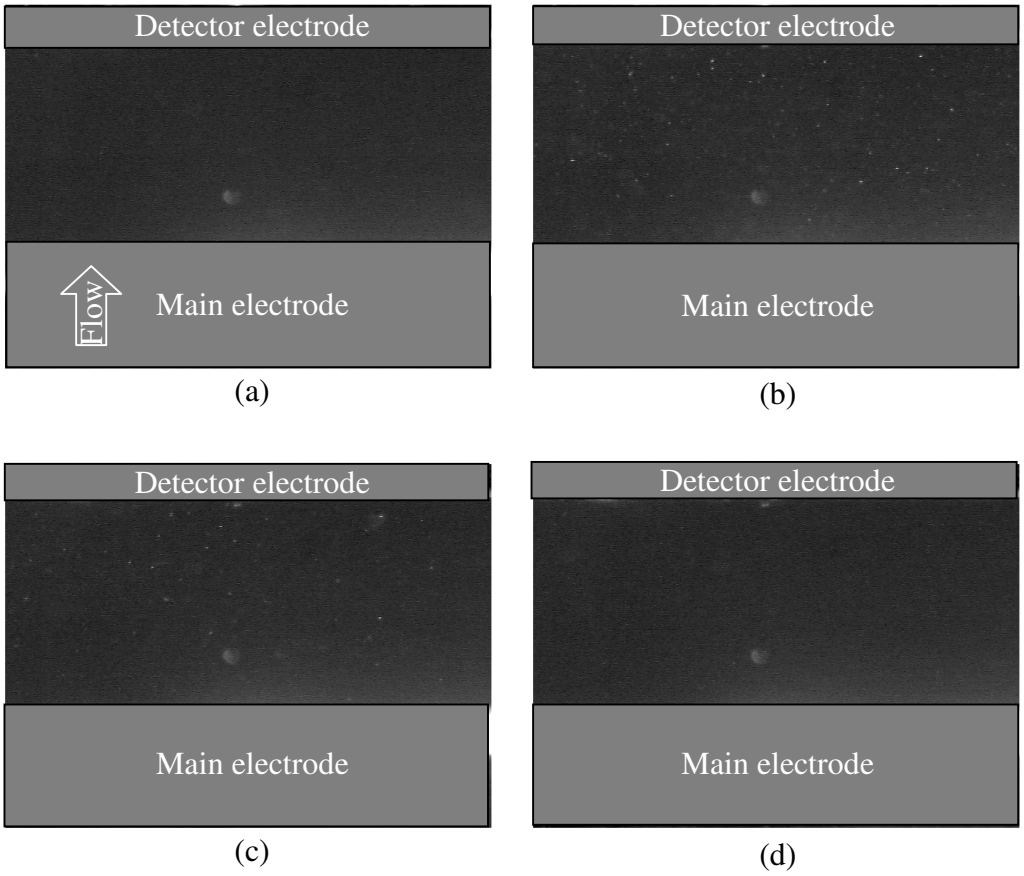

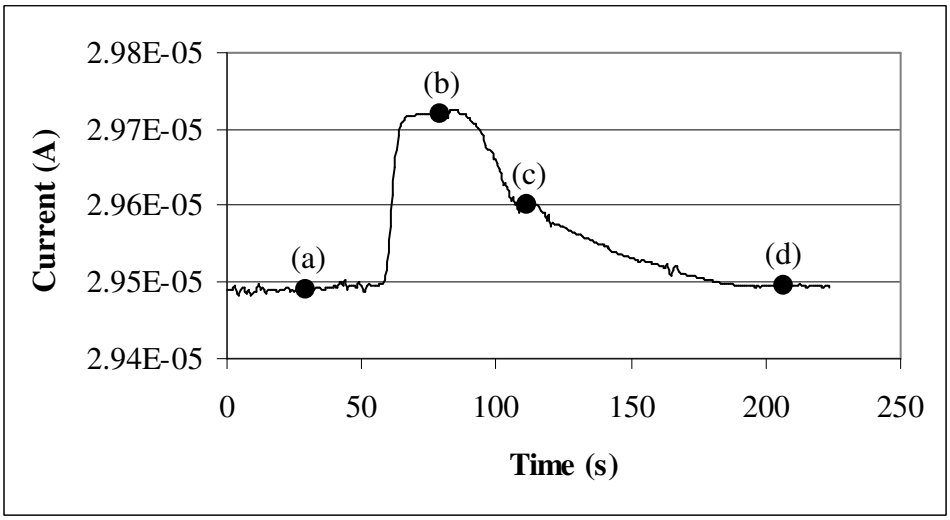

(e)

Figure 6.7: Digital images of 80-nm gold RLS Particles™ at (a) time of injection (29.3 seconds), (b) 79.3 seconds, (c) 111.6 seconds, and (d) 206.7 seconds. The locations of the detector and main electrodes (above and below the window) are shown. The light spot in the middle of the window (in each figure) is a bubble in the immersion oil below the device. Also shown is the corresponding electrical signal (e).

the bottom to the top of each frame, as indicated by the arrow in Figure 6.7 (a). Also shown is the correlation between the electrical and optical detection measurements (Figure 6.7 (e)). These results show that the optical and electrical signals can be correlated for quantification of the sample peak characteristics such as particle concentration and particle type.

6.5 Conclusions

Experimental results of the complementary electrical and optical detection methods showed a good correlation between theory and empirical results. Both methods were shown to be useful for measuring sample concentration and size. However, optical detection is much more sensitive as individual particles can be observed. Furthermore, the color of the analytes can be used to determine the particle size or type if other parameters are known.

The combination of these two types of detection methods enables powerful analysis of separated sample components. This capability is especially useful for determining the efficacy of the μ-ElFFF system if two types of particles have similar retention times.

CHAPTER 7

CONCLUSION

7.1 Objective and Specific Aims

The objective of this work was to develop efficient μ-ElFFF systems with complementary electrical and optical detection capabilities. Such systems are capable of separating a wide variety of sample components, including biological and synthetic substances.

To accomplish the objective, four specific aims were identified:

1. Design and fabricate a glass-based μ-ElFFF system for optical and electrical detection of biological and non-biological samples
2. Integrate resonance light scattering detection with the μ-ElFFF system
3. Characterize the μ-ElFFF system
4. Determine a quantitative correlation of optical and electrical signals

In Chapter 3, the design and fabrication of three sizes of μ-ElFFF systems was presented. The operation and characterization of the systems was discussed in detail and presented in Chapter 4. The integration of electrical detection and on-column optical RLS detection was discussed in Chapter 5. And finally, a quantitative analysis and correlation between optical and electrical signals was provided in Chapter 6.

7.2 Contributions of Completed Work

This work represents a significant contribution to the fields of separation science, MEMS and BioMEMS. The μ-ElFFF separation systems with channel heights of 5 μm are unique and have the potential of being useful for separations of smaller particles and molecules like DNA fragments or synthetic polymeric molecules.

The development of μ-ElFFF systems fabricated using thermal bonding of glass substrates yields extremely robust systems capable of hundreds of runs. This quality makes them desirable for applications that require portable systems and enables full characterization of each system individually. Additionally, the use of all-glass devices would enable the use of corrosive or organic/solvent type carrier fluids since these liquids degrade many kinds of seals typically employed by most FFF systems [6]. The ability to use a wider variety of carrier fluids would enable the separation of many more types of particles.

This work represents the first use of RLS detection with μ-ElFFF devices. Optical detection can be used as a stand-alone technique for sample analysis, or as a complementary technique. Using optically transparent substrate and electrode materials (e.g., ITO) makes the RLS detection capability useful for observing separation phenomena during the separation in addition to performing particle detection after completion of the separation.

Finally, several fabrication processes were developed or modified for this work since glass was used as the substrate. For instance, novel techniques and methods were developed for enhancing the adhesion of SU-8 on glass substrates; for using SU-8 as a bonding agent; and for bonding substrates with patterned electrodes.

7.3 Possible Related Future Work

This novel advances made in this work provide the foundation for many possible enhancements to the μ-ElFFF systems. Future work may include the design of an improved method of sample injection. If the sample injection was integrated on chip, a sample could be introduced into the channel in a way that would reduce band broadening; a smaller, more precise injection volume could be achieved; and in many configurations, for instance an electrically actuated injector, human error could be minimized. There has

been much work published regarding micropumps, which could be one means of providing the on-chip sample injection [110, 111].

Another possible enhancement would be to incorporate electrodes that help to concentrate the sample, as demonstrated by F.A. Shaikh and V.M. Ugaz [112]. This would likely only require a modification to the masks used to pattern the electrodes.

With the development of the μ-ElFFF systems in this work that enable RLS detection, the foundation is provided whereby the integration of Raman Spectra detection would be relatively straightforward (Figure 7.1). Enhanced sample characterization would be the result of such an improvement.

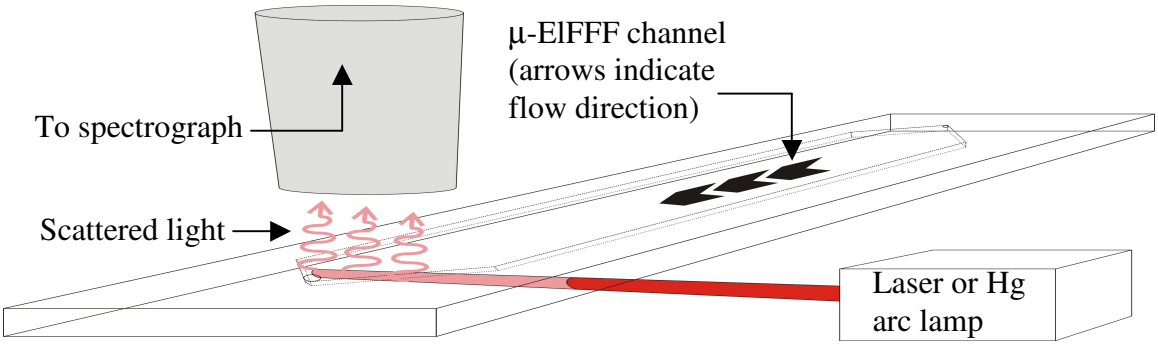

Figure 7.1: Diagram showing concept of integrating Raman spectroscopy with μ-ElFFF systems

Finally, the electrical detection could also be performed by employing a Wheatstone bridge configuration where the microchannel would function as one of the resistors (Figure 7.2). This is the principle many katharometers and electrolytic conductivity detectors are based on.

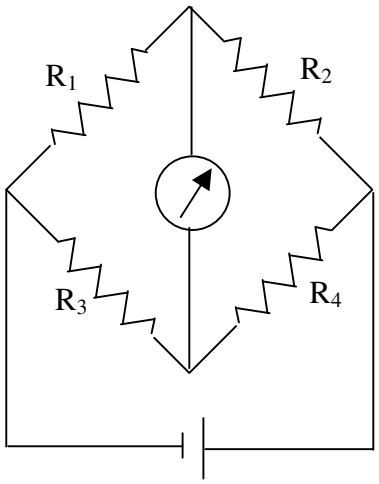

$R_1 R_4 = R_2 R_3$

Figure 7.2: Wheatstone bridge schematic. If the equation $R_1 R_4 = R_2 R_3$ is not satisfied, a current will pass through the ammeter. For the suggested application, three of the resistor values are fixed and one represents the resistance across the channel.

7.4 Conclusions

Microfabricated ElFFF systems capable of separating a wide variety of substances were designed and tested. The integration of electrical detection and the use of on-column RLS detection was described and presented. Correlation between the complementary detection methods was performed and the results show that the tandem use of these methods provides an enhanced method for sample detection and analysis.

Several novel processes were developed for fabricating the μ-ElFFF systems described in this work that have potential applications for making other microfabricated devices. Furthermore, the use of substrates that are non-conventional in the field of MEMS provides the groundwork for the future development of innovative devices based on similar substrates and similar fabrication processes. Finally, MEMS and BioMEMS are rapidly growing fields and the establishment of fundamental technologies and techniques, as presented in this work, are essential to creating a toolbox that will drive the further development of novel devices and systems.

APPENDIX A

LabVIEW: HP3458A and 33250A FFF with Image.vi

Front Panel

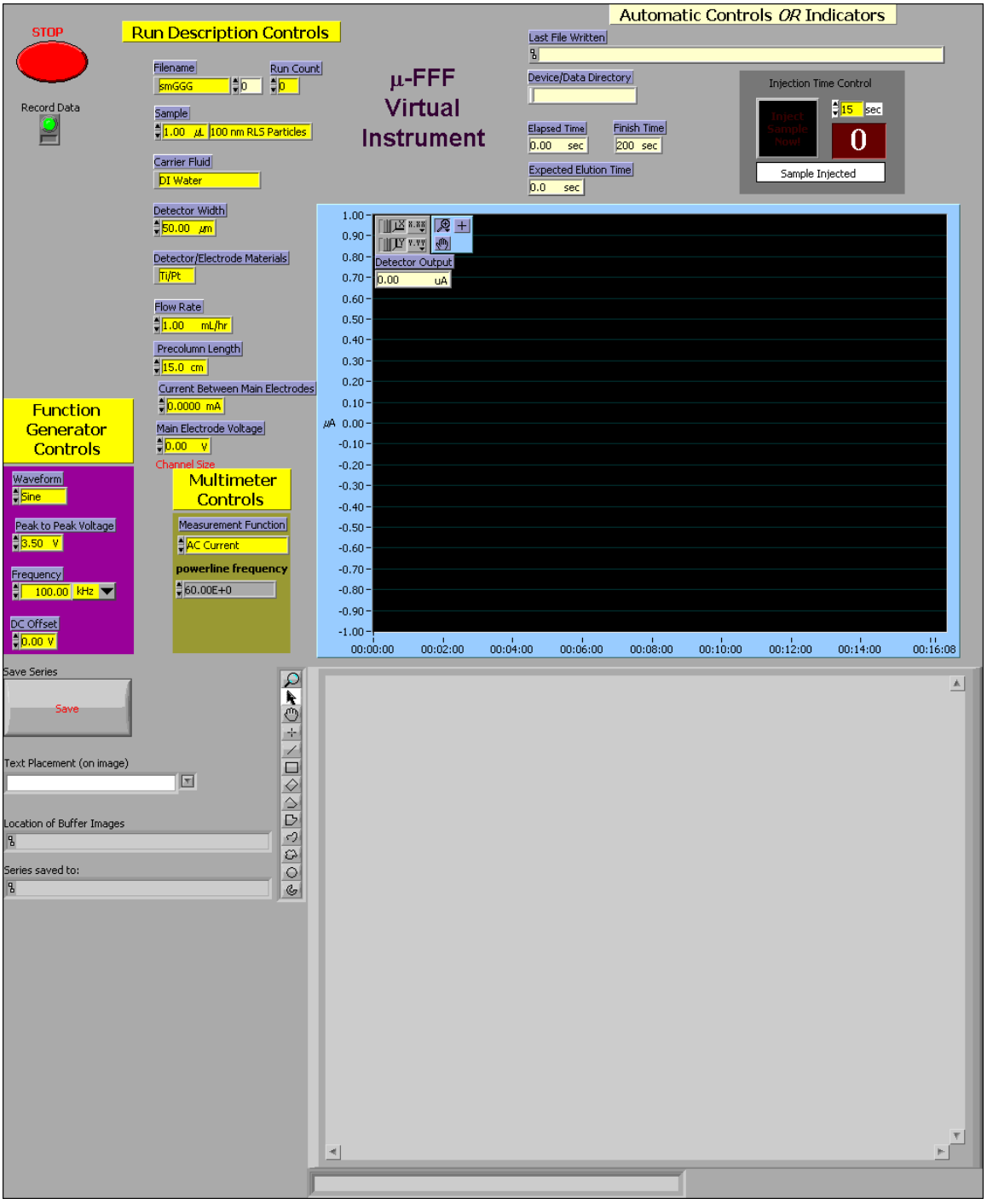

Controls and Indicators

Instr. Descriptor (GPIB:22) A string that uniquely identifies the instrument to open or initialize. The grammar for the instrument descriptor is shown below. Parameters are shown in lower-case and optional parameters are shown in square brackets ([]).

Default Value: GPIB::22::INSTR

GPIB - GPIB[bd]::prim addr[::sec addr]
VXI - VXI[bd]::logical addr
GPIB-VXI - GPIB-VXI[bd][::prim addr]::logical addr

Parameters (default value):
bd - GPIB board (0)
prim addr - GPIB primary address (1)
sec addr - GPIB secondary address (none)
logical addr - VXI logical address

EXAMPLE: A GPIB instrument on GPIB board 0, at primary address 5, and no secondary addressing.

GPIB::5

error in (no error) error in is a cluster that describes the error status before this VI executes. If error in indicates that an error occurred before this VI was called, this VI may choose not to execute its function, but just pass the error through to its error out cluster. If no error has occurred, then this VI executes normally and sets its own error status in error out. Use the error handler VIs to look up the error code and to display the corresponding error message. Using error in and error out clusters is a convenient way to check errors and to specify execution order by wiring the error output from one subVI to the error input of the next.

Valid Range:
Not Applicable

Default:
status= False (no error)
code = 0
source = empty string

status status is TRUE if an error occurred before this VI was called, or FALSE if not. If status is TRUE, code is a non-zero error code. If status is FALSE, code can be zero or a warning code.

Valid Range:
T: Error
F: No Error (default)

code code is the number identifying an error or warning. If status is TRUE, code is a non-zero error code. If status is FALSE, code can be zero or a warning code. Use the error handler VIs to look up the meaning of this code and to display the corresponding error message.

Valid Range:
Not Applicable

Default:0

source source is a string that indicates the origin of the error, if any. Usually source is the name of the VI in which the error occurred.

Default:
Empty String

error out error out is a cluster that describes the error status after this VI executes. If an error occurred before this VI was called, error out is the same as error in. Otherwise, error out shows the error, if any, that occurred in this VI. Use the error handler VIs to look up the error code and to display the corresponding error message. Using error in and error out clusters is a convenient way to check errors and to specify execution order by wiring the error output from one subVI to the error input of the next.

Valid Range:
Not Applicable

Default:
status= False (no error)
code = 0
source = empty string

status status is TRUE if an error occurred, or FALSE if not. If status is TRUE, code is a non-zero error code. If status is FALSE, code can be zero or a warning code.

Valid Range:
T: Error
F: No Error (default)

code code is the number identifying an error or warning. If status is TRUE, code is a non-zero error code. If status is FALSE, code can be zero or a warning code. Use the error handler VIs to look up the meaning of this code and to display the corresponding error message.

Valid Range:
Not Applicable

Default:0

source source is a string that indicates the origin of the error, if any. Usually source is the name of the VI in which the error occurred.

Default:
Empty String

Block Diagram

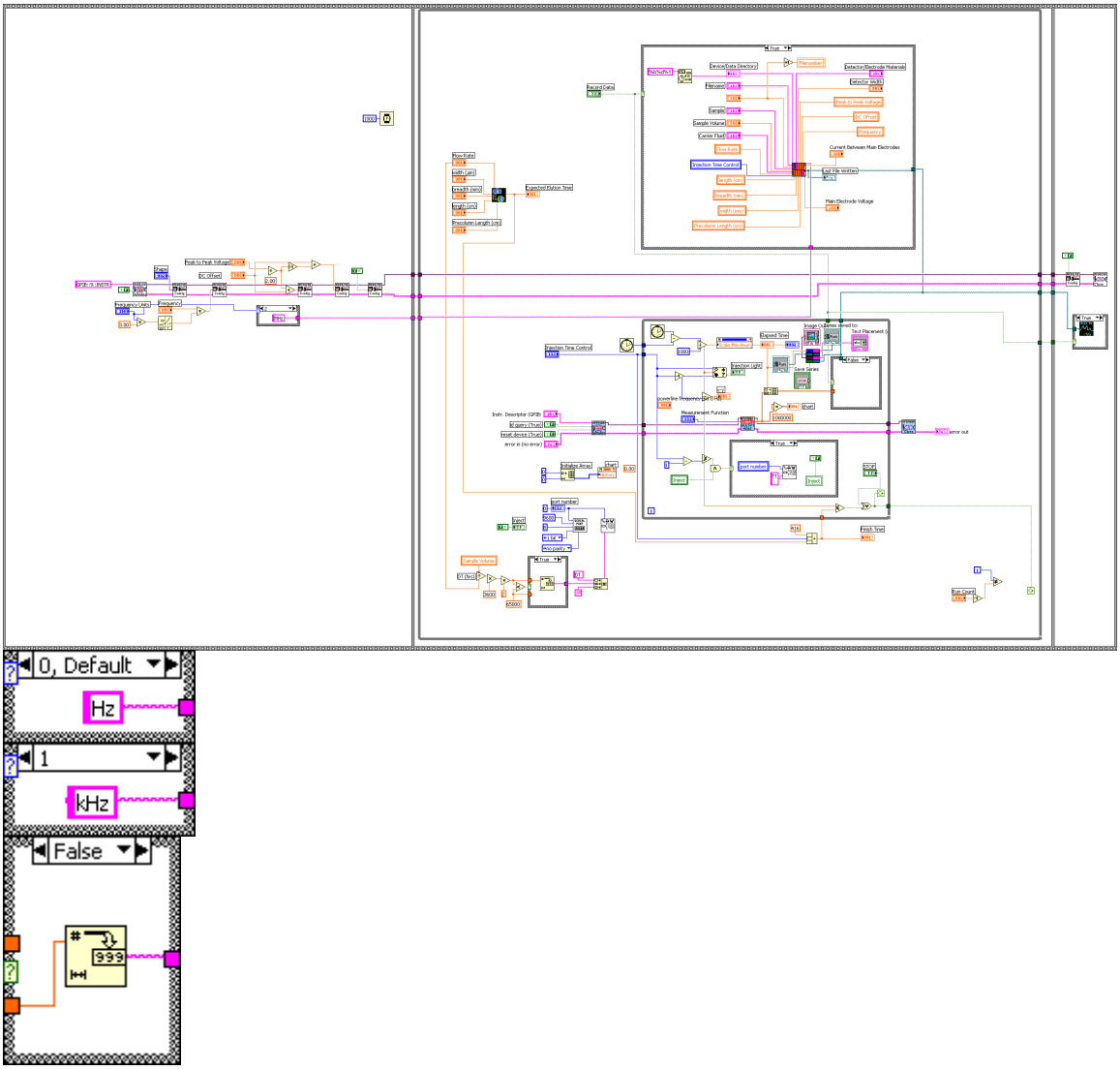

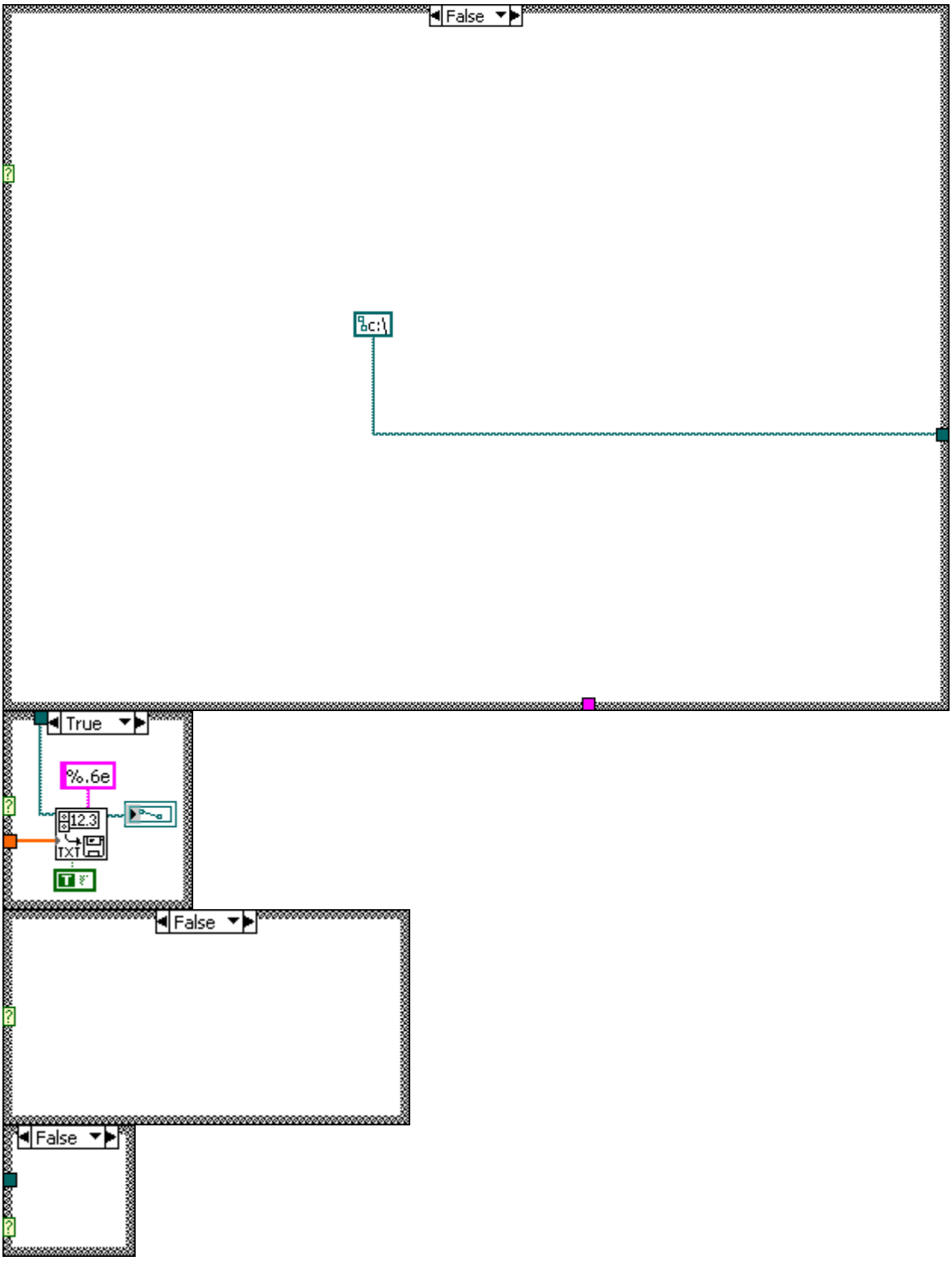
False
c:\
True
%.6e
12.3
txt
False
False

List of SubVIs and Express VIs

Write To Spreadsheet File.vi
C:\Program Files\National Instruments\LabVIEW 7.0\vi.lib\Utility\file.llb\Write To Spreadsheet File.vi

ag33250a Initialize.vi
F:\National Instruments\LabVIEW\INSTR.LIB\ag33250a\ag33250a.LLB\ag33250a Initialize.vi

ag33250a Output Function Shape Setup.vi
F:\National Instruments\LabVIEW\INSTR.LIB\ag33250a\ag33250a.LLB\ag33250a Output Function Shape Setup.vi

ag33250a Output Frequency Setup.vi
F:\National Instruments\LabVIEW\INSTR.LIB\ag33250a\ag33250a.LLB\ag33250a Output Frequency Setup.vi

ag33250a Output Setup.vi
F:\National Instruments\LabVIEW\INSTR.LIB\ag33250a\ag33250a.LLB\ag33250a Output Setup.vi

ag33250a Close.vi
F:\National Instruments\LabVIEW\INSTR.LIB\ag33250a\ag33250a.LLB\ag33250a Close.vi

ag33250a Output Voltage High Setup.vi
F:\National Instruments\LabVIEW\INSTR.LIB\ag33250a\ag33250a.LLB\ag33250a Output Voltage High Setup.vi

ag33250a Output Voltage Low Setup.vi
F:\National Instruments\LabVIEW\INSTR.LIB\ag33250a\ag33250a.LLB\ag33250a Output Voltage Low Setup.vi

Serial Port Init.vi
C:\Program Files\National Instruments\LabVIEW 7.0\vi.lib\Instr\Serial.llb\Serial Port Init.vi

Serial Port Write.vi
C:\Program Files\National Instruments\LabVIEW 7.0\vi.lib\Instr\Serial.llb\Serial Port Write.vi

FFF Data File Header
F:\My Documents\Mason\Mason.llb\FFF Data File Header

Elution Time
F:\My Documents\Mason\Mason.llb\Elution Time

hp3458a Initialize.vi
C:\Program Files\National Instruments\LabVIEW 7.0\instr.lib\hp3458a\hp3458a.LLB\hp3458a Initialize.vi

hp3458a Multi-point Measurement.vi
C:\Program Files\National Instruments\LabVIEW 7.0\instr.lib\hp3458a\hp3458a.LLB\hp3458a Multi-point Measurement.vi

hp3458a Close.vi
C:\Program Files\National Instruments\LabVIEW 7.0\instr.lib\hp3458a\hp3458a.LLB\hp3458a Close.vi

DatatoPNG.vi
F:\My Documents\Mason\Mason.llb\DatatoPNG.vi

TESTPhoto.vi
F:\My Documents\Mason\TESTPhoto.vi

APPENDIX B

MATLAB: Code for Finding the Plate Heights of Multiple FFF Files

```
% Initialize
clear;                                                  % Clear the variables

for i=8:1:101


% Get the Data
%name=input('What is the filename?  lgGGG_','s');              % Get the filename
filename=['smGGG_',num2str(i-1),'.fff'];                % Complete the filename

data=dlmread(filename,'\t',20,0);                       % Get the data without the header
%datetime=head(1,1);
all = textread(filename,'%s','delimiter','\t','whitespace','');
sample=all(6);
file=all(2);
sampvol(i)=dlmread(filename,'\t',[3 1 3 1]);
TI(i)=dlmread(filename,'\t',[4 1 4 1]);
carrier=all(12);
FR(i)=dlmread(filename,'\t',[6 1 6 1]);                 % Carrier flow rate (mL/hr)
width(i)=dlmread(filename,'\t',[7 1 7 1]);
breadth(i)=dlmread(filename,'\t',[8 1 8 1]);
length(i)=dlmread(filename,'\t',[9 1 9 1]);
prelength(i)=dlmread(filename,'\t',[10 1 10 1]);
detector=all(24);
detwidth(i)=dlmread(filename,'\t',[12 1 12 1]);
detfreq(i)=dlmread(filename,'\t',[13 1 13 1]);
detvolt(i)=dlmread(filename,'\t',[14 1 14 1]);
detdc(i)=dlmread(filename,'\t',[15 1 15 1]);
elecfreq(i)=dlmread(filename,'\t',[16 1 16 1]);
elecvolt(i)=dlmread(filename,'\t',[17 1 17 1]);
eleccurr(i)=dlmread(filename,'\t',[18 1 18 1]);

% Manipulate the data
time=data(:,1);                                         % Extract the time vector from the data
signal=data(:,2);                                       % Extract the signal vector from the data
signal=signal-mean(signal(25:50));                      % Move the signal baseline to zero
area(i)=((width(i))/25000)*(breadth(i)/100);    % Cross sectional area of channel in cm^2
velocity(i)=FR(i)/area(i)/3600;                         % Carrier fluid velocity in cm/sec

% Find important parameters for calculating the plate height
sig_max(i)=max(signal);                                 % Find the signal peak
max_ind=find(signal==sig_max(i));               % Find the vector index of the signal peak
```

```
max_length=size(max_ind);
if max_length(1,1) > 1
   max_mid=int8(max_length(1,1)/2);
   max_ind(i)=max_ind(max_mid(1,1));
elseif max_length(1,1)==1
   max_ind(i)=max_ind;
end
TP(i)=time(max_ind(i))-TI(i);                    % Find the time at which the signal peaks
sig_half(i)=sig_max(i)/2;                        % Find the half max value (HMV) of the signal
half_ind=find(sig_half(i) <= signal & signal <= sig_max(i));  % Find the vector index of
                                                                the signal HMV
vsize=find(half_ind==max_ind(i));      % Find the index of the vector at maximum value
half_ind1(i)=min(half_ind(1:vsize));                % Index of first signal at HMV
half_ind2(i)=max(half_ind(vsize:end));              % Index of second signal at HMV
TW1(i)=time(half_ind1(i))-TI(i);                    % First time at signal HMV
TW2(i)=time(half_ind2(i))-TI(i);                    % Second time at signal HMV

% Calculate the plate height
N(i)=5.54*(TP(i)/(TW2(i)-TW1(i)))^2;                % Number of theoretical plates
H(i)=(length(i))/N(i);                                          % Plate height
end

plateheight=zeros(i,2);
plateheight(1:end,1)=velocity.';
y=find(velocity);
nvelocity=velocity(y);
plateheight(1:end,2)=H.';
z=find(H);
nH=H(z);
y=find(plateheight(:,1));
z=find(plateheight(:,2));
nplateheight(:,1)=plateheight(y,1);
nplateheight(:,2)=plateheight(z,2);
dlmwrite('plateheight.fff',nplateheight,'\t');

% Plot the Plate Height vs. Velocity
plot(nvelocity,nH,'o','MarkerEdgeColor','k','MarkerFaceColor','r');% 2D plot of the signal
                                                                versus time

title({'Plate Height versus Velocity for a 30 \mum on-chip Ti/Au detector'});
text(0,10,{num2str(width),'\mum x ',num2str(breadth),'cm x ',num2str(length),'mm +
',num2str(prelength),'cm precolumn tubing.'});
xlabel('Carrier Velocity (cm/sec)');
ylabel('Plate Height (cm)');
axis([0 1 0 .5]);
```

APPENDIX C

LabVIEW: Video Maker with Time Control.vi

Front Panel

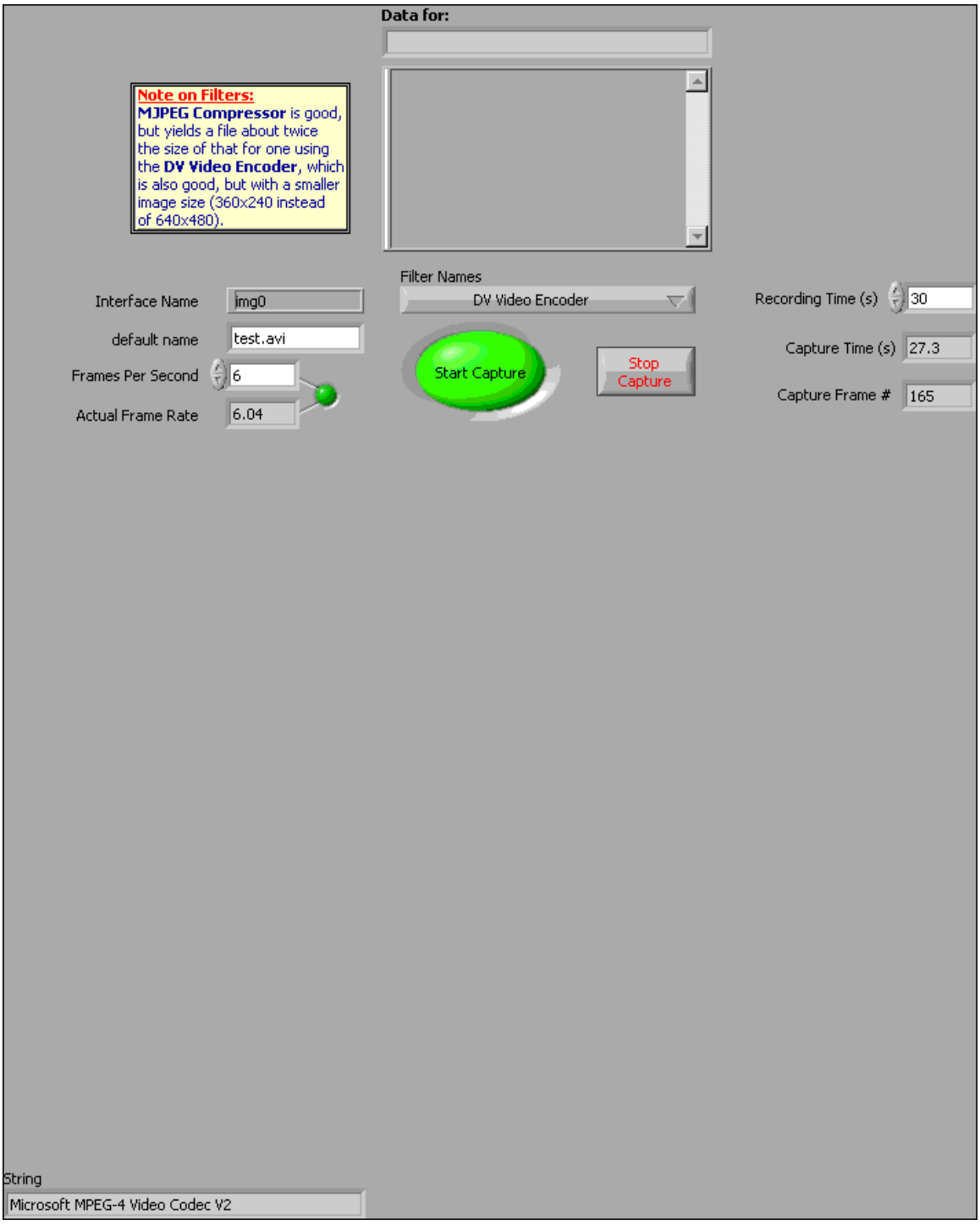

Block Diagram

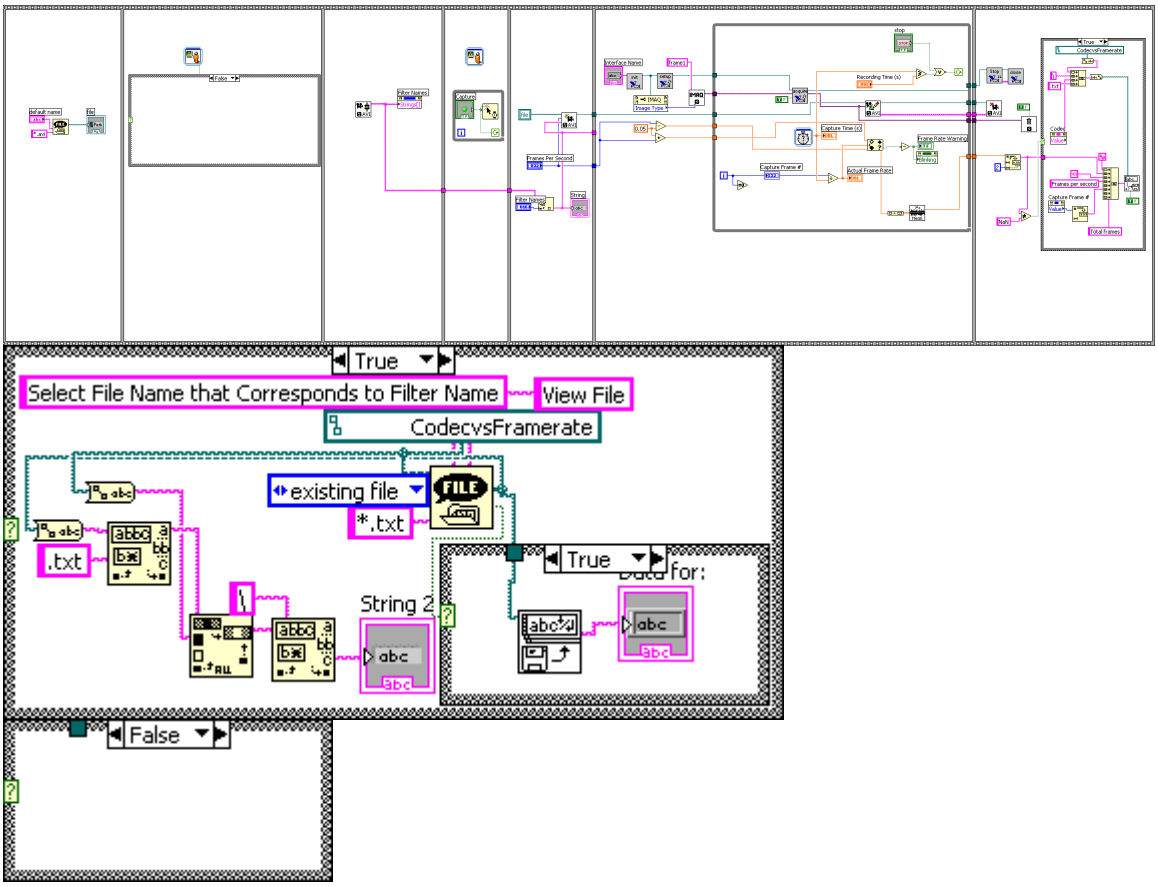

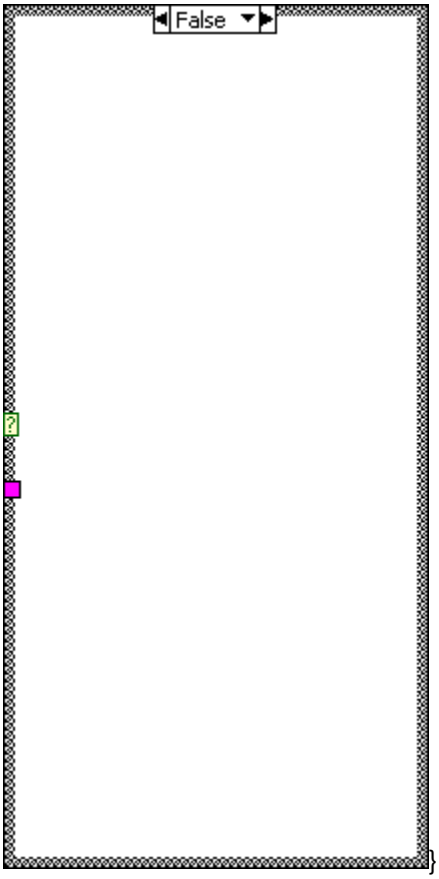

List of SubVIs and Express VIs

IMAQ Init.vi
C:\Program Files\National Instruments\LabVIEW 7.0\vi.lib\vision\driver\imaqhl.llb\IMAQ Init.vi

IMAQ Create
C:\Program Files\National Instruments\LabVIEW 7.0\vi.lib\vision\Basics.llb\IMAQ Create

IMAQ AVI Create
C:\Program Files\National Instruments\LabVIEW 7.0\vi.lib\vision\Avi1.llb\IMAQ AVI Create

IMAQ Grab Setup.vi
C:\Program Files\National Instruments\LabVIEW 7.0\vi.lib\vision\driver\imaqhl.llb\IMAQ Grab Setup.vi

IMAQ AVI Get Filter Names
C:\Program Files\National Instruments\LabVIEW 7.0\vi.lib\vision\Avi2.llb\IMAQ AVI Get Filter Names

IMAQ Close.vi
C:\Program Files\National Instruments\LabVIEW 7.0\vi.lib\vision\driver\imaqhl.llb\IMAQ Close.vi

IMAQ Stop.vi
C:\Program Files\National Instruments\LabVIEW 7.0\vi.lib\vision\driver\imaqll.llb\IMAQ Stop.vi

IMAQ Grab Acquire.vi
C:\Program Files\National Instruments\LabVIEW 7.0\vi.lib\vision\driver\imaqhl.llb\IMAQ Grab Acquire.vi

IMAQ AVI Write Frame
C:\Program Files\National Instruments\LabVIEW 7.0\vi.lib\vision\Avi1.llb\IMAQ AVI Write Frame

Elapsed Time
Elapsed Time

IMAQ Dispose
C:\Program Files\National Instruments\LabVIEW 7.0\vi.lib\vision\Basics.llb\IMAQ Dispose

IMAQ AVI Close
C:\Program Files\National Instruments\LabVIEW 7.0\vi.lib\vision\Avi1.llb\IMAQ AVI Close

Mean.vi
C:\Program Files\National Instruments\LabVIEW 7.0\vi.lib\Analysis\baseanly.llb\Mean.vi

Write Characters To File.vi
C:\Program Files\National Instruments\LabVIEW 7.0\vi.lib\Utility\file.llb\Write Characters To File.vi

Display Message to User
Display Message to User

Display Message to User2
Display Message to User

Read Lines From File.vi
C:\Program Files\National Instruments\LabVIEW 7.0\vi.lib\Utility\file.llb\Read Lines From File.vi

APPENDIX D

LabVIEW: Intensity.vi

Front Panel

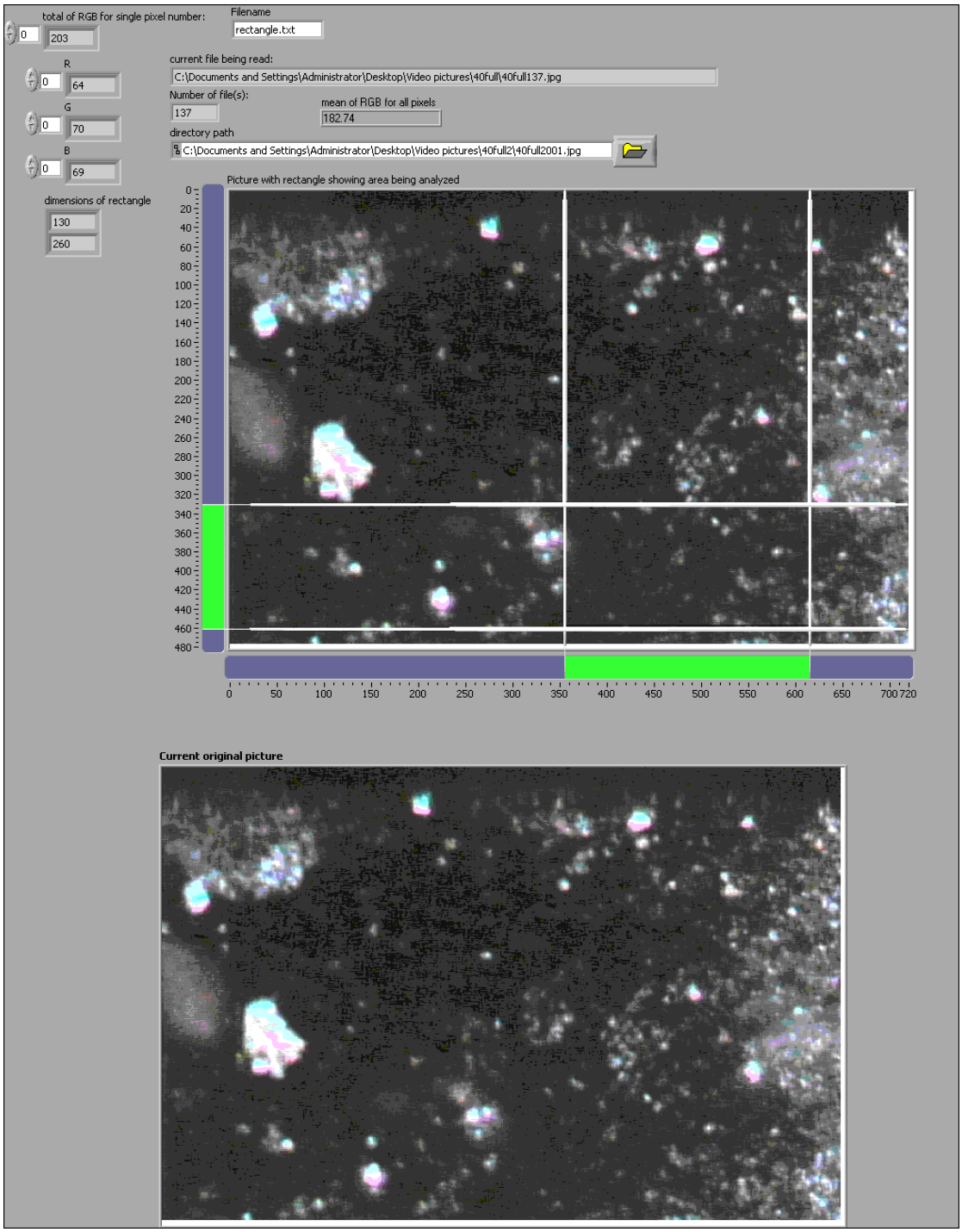

Block Diagram

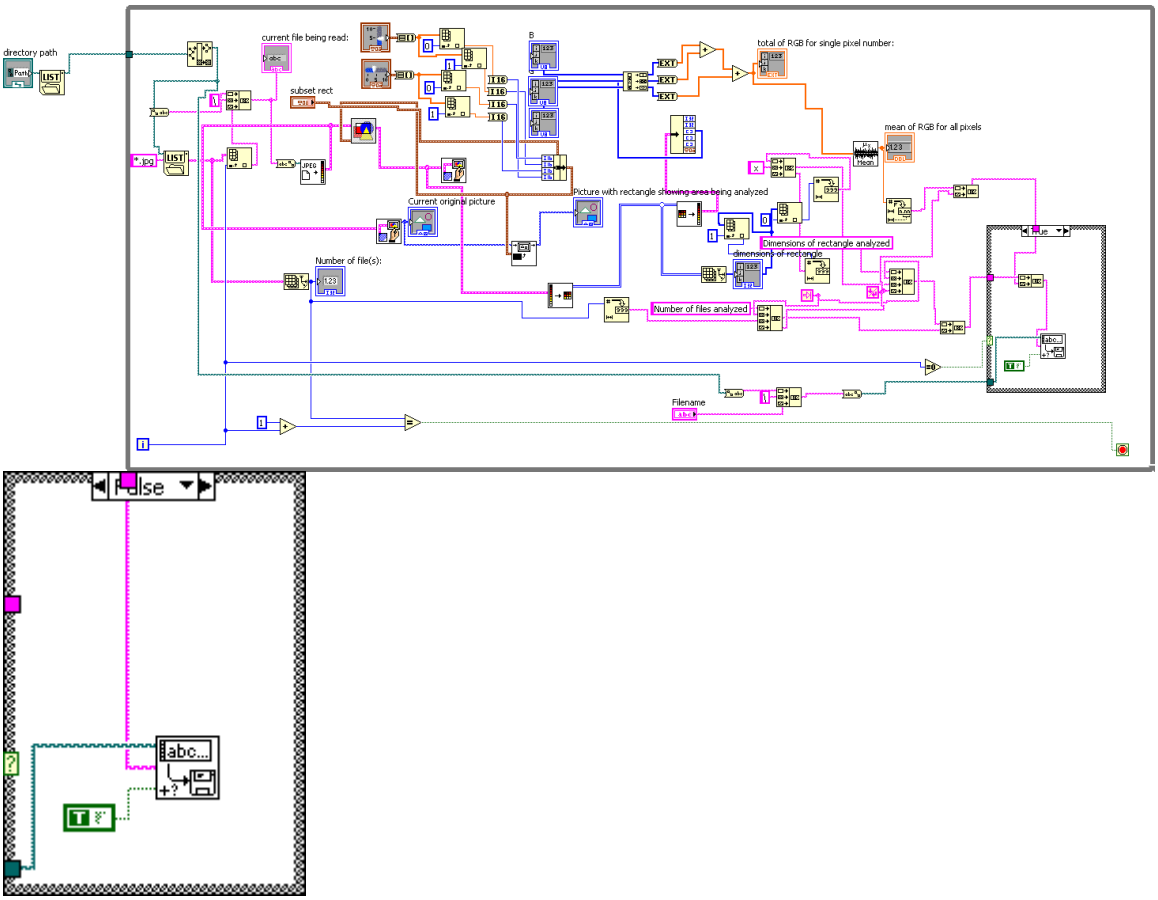

List of SubVIs and Express VIs

Get Image Subset.vi
C:\Program Files\National Instruments\LabVIEW 7.0\vi.lib\picture\pictutil.llb\Get Image Subset.vi

Draw Flattened Pixmap.vi
C:\Program Files\National Instruments\LabVIEW 7.0\vi.lib\picture\picture.llb\Draw Flattened Pixmap.vi

Draw Rect.vi
C:\Program Files\National Instruments\LabVIEW 7.0\vi.lib\picture\picture.llb\Draw Rect.vi

Unflatten Pixmap.vi
C:\Program Files\National Instruments\LabVIEW 7.0\vi.lib\picture\pixmap.llb\Unflatten Pixmap.vi

Mean.vi
C:\Program Files\National Instruments\LabVIEW 7.0\vi.lib\Analysis\baseanly.llb\Mean.vi

Read JPEG File.vi
C:\Program Files\National Instruments\LabVIEW 7.0\vi.lib\picture\jpeg.llb\Read JPEG File.vi

Write Characters To File.vi
C:\Program Files\National Instruments\LabVIEW 7.0\vi.lib\Utility\file.llb\Write Characters To File.vi

REFERENCES

[1] T. C. Scott, "Use of Electric Fields in Solvent Extraction: A Review and Prospectus," *Separtion and Purification Methods*, vol. 18, pp. 65-109, 1989.

[2] J. H. Siegell, G. D. Dupre, and J. C. Pirkle, Jr., "Chromatographic Separations in a Crossflow Magnetically Stabilized Bed," *Recent Advances in Separation Techniques*, vol. 82, pp. 128-134, 1986.

[3] M. V. Sussman, K. N. Astill, R. Rombach, A. Cerullo, and S. S. Chen, "Continuous Surface Chromatography," *Industrial & Engineering Chemistry Fundamentals*, vol. 11, pp. 181-190, 1972.

[4] X. Chen, K.-G. Wahlund, and J. C. Giddings, "Gravity-Augmented High-Speed Flow/Steric Field-Flow Fractionation: Simultaneous Use of Two Fields," *Analytical Chemistry*, vol. 60, pp. 362-365, 1988.

[5] M. N. Myers and J. C. Giddings, "A Continuous Steric FFF Device for the Size Separation of Particles," *Powder Technology*, vol. 23, pp. 15-20, 1979.

[6] G. Liu and J. C. Giddings, "Separation of Particles in Nonaqueous Suspensions by Thermal-Electrical Field-Flow Fractionation," *Analytical Chemistry*, vol. 63, pp. 296-299, 1991.

[7] R. Sargent and W. Rieman, III, "Salting-out Chromatography II: Amines," *Analytica Chimica Acta*, vol. 17, pp. 408-414, 1957.

[8] C. A. Burtis, "The Determination of the Base Composition of RNA by High-Pressure Cation-exchange Chromatography," *Journal of Chromatography*, vol. 51, pp. 183-194, 1970.

[9] M. H. Moon and J. C. Giddings, "Size Distribution of Liposomes by Flow Field-flow Fractionation," *Journal of Pharmaceutical and Biomedical Analysis*, vol. 11, pp. 911-920, 1993.

[10] J. J. Kirkland, W. W. Yau, and F. C. Szoka, "Sedimentation Field-flow Fractionation of Liposomes," *Science*, vol. 215, pp. 296-298, 1982.

[11] T. Provder, American Chemical Society. Division of Polymeric Materials: Science and Engineering., and American Chemical Society. Meeting, *Particle Size Distribution II: Assessment and Characterization*. Washington, DC: American Chemical Society, 1991.

[12] K. D. Caldwell and Y.-S. Gao, "Electrical Field-Flow Fractionation in Particle Separation. 1. Monodisperse Standards," *Analytical Chemistry*, vol. 65, pp. 1764-1772, 1993.

[13] G. Liu and J. C. Giddings, "Separation of Particles in Aqueous Suspensions by Thermal Field-flow Fractionation. Measurement of Thermal Diffusion Coefficients," *Chromatographia*, vol. 34, pp. 483-492, 1992.

[14] J. C. Giddings and M. H. Moon, "Measurement of Particle Density, Porosity, and Size Distribributions by Sedimentation/Steric Field-flow Fractionation: Application to Chromatographic Supports," *Analytical Chemistry*, vol. 63, pp. 2869-2877, 1991.

[15] M. Graff and A. B. Frazier, "Resonance Light Scattering (RLS) Detection of Nanoparticle Separations in a Microelectrical Field-flow Fractionation System," *IEEE Transactions on Nanotechnology*, To be published.

[16] S. C. Terry, "A Gas Chromatography System Fabricated on a Silicon Wafer Using Integrated Circuit Technology," vol. Ph.D.: Stanford University, 1975.

[17] S. C. Terry, "Gas Chromatographic Air Analyzer Fabricated on a Silicon Wafer," *IEEE Transactions on Electronic Devices*, vol. 26, 1979.

[18] J. C. Gluckman and M. Novotny, "Nitrogen-sensitive Thermionic Detection in Microcolumn Liquid Chromatography," *Journal of Chromatography*, vol. 333, pp. 291-300, 1985.

[19] A. Manz, Y. Miyahara, J. Miura, Y. Watanabe, H. Miyagi, and K. Sato, "Design of an Open-tubular Column Liquid Chromatograph Using Silicon Chip Technology," *Sensors and Actuators B*, vol. 1, pp. 249-255, 1990.

[20] A. Manz, D. J. Harrison, E. M. J. Verpoorte, J. C. Fettinger, A. Paulus, H. Lüdi, and H. M. Widmer, "Planar Chips Technology for Miniaturization and Integration of Separation Techniques Into Monitoring Systems Capillary Electrophoresis on a Chip," *Journal of Chromatography*, vol. 593, pp. 253-258, 1992.

[21] D. E. Raymond, A. Manz, and H. M. Widmer, "Continuous Separation of High Molecular Weight Compounds Using a Microliter Volume Free-flow Electrophoresis Microstructure," *Analytical Chemistry*, vol. 68, pp. 2515-2522, 1996.

[22] D. E. Raymond, A. Manz, and H. M. Widmer, "Continuous Sample Pretreatment Using a Free-flow Electrophoresis Device Integrated onto a Silicon Chip," *Analytical Chemistry*, vol. 66, pp. 2858-2865, 1994.

[23] B. K. Gale, A. B. Frazier, and K. D. Caldwell, "Micromachined Electrical Field-flow Fractionation (μ-EFFF) System," presented at Tenth Annual Workshop on Micro Electro Mechanical Systems, 1997, Nagoya, Japan, 1997.

[24] B. C. C. Inc., "RC-073N Separations Systems for Commercial Biotechnology," Business Communications Company, Inc., 2003.

[25] B. He and F. Regnier, "Microfabricated Liquid Chromatography Columns Based on Collocated Monolith Support Structures," *Journal of Pharmaceutical and Biomedical Analysis*, vol. 17, pp. 925-932, 1998.

[26] A. T. Woolley, G. F. Sensabaugh, and R. A. Mathies, "High-speed DNA Genotyping Using Microfabricated Capillary Array Electrophoresis Chips," *Analytical Chemistry*, vol. 69, pp. 2181-2186, 1997.

[27] M. Freemantle, "Downsizing Chemistry," *Chemical and Engineering News*, vol. 77, pp. 27-36, 1999.

[28] P. C. Simpson, D. Roach, A. T. Woolley, T. Thorsen, R. Johnston, G. F. Sensabaugh, and R. A. Mathies, "High-Throughput Genetic Analysis Using Microfabricated 96-Sample Capillary Array Electrophoresis Microplates," *Proceedings of the National Academy of Sciences of the United States of America*, vol. 95, pp. 2256-2261, 1998.

[29] G. Stemme and G. Kittilsland, "New Fluid Filter Structure in Silicon Fabricated Using a Self-aligning Technique," *Applied Physics Letters*, vol. 53, pp. 1566-1568, 1988.

[30] T. Deng, M. Prentiss, and G. M. Whitesides, "Fabrication of Magnetic Microfiltration Systems Using Soft Lithography," *Applied Physics Letters*, vol. 80, pp. 461-463, 2002.

[31] A. Manz, N. Graber, and H. M. Widmer, "Miniaturized Total Chemical Analysis Systems: A Novel Concept for Chemical Sensing," *Sensors and Actuators B*, vol. 1, pp. 244-248, 1990.

[32] D. J. Harrison, A. Manz, Z. Fan, H. Lüdi, and H. M. Widmer, "Capillary Electrophoresis and Sample Injection Systems Integrated on a Planar Glass Chip," *Analytical Chemistry*, vol. 64, pp. 1926 - 1932, 1992.

[33] S. C. Jacobson, R. Hergenröder, L. B. Koutny, and J. M. Ramsey, "High-speed Separations on a Microchip," *Analytical Chemistry*, vol. 66, pp. 1114-1118, 1994.

[34] S. C. Jacobson, R. Hergenröder, L. B. Koutny, R. J. Warmack, and J. M. Ramsey, "Effects of Injection Schemes and Column Geometry on the Performance of Microchip Electrophoresis Devices," *Analytical Chemistry*, vol. 66, pp. 1107-1113, 1994.

[35] A. T. Woolley and R. A. Mathies, "Ultra-high-speed DNA Fragment Separations Using Microfabricated Capillary Array Electrophoresis Chips," *Proceedings of the National Academy of Sciences of the United States of America*, vol. 91, pp. 11348-11352, 1994.

[36] P. F. Gavin and A. G. Ewing, "Continuous Separations with Microfabricated Electrophoresis-Electrochemical Array Detection," *Journal of the American Chemical Society*, vol. 118, pp. 8932-8936, 1996.

[37] J. Cheng, M. A. Shoffner, G. E. Hvichia, L. J. Kricka, and P. Wilding, "Chip PCR. II. Investigation of Different PCR Amplification Systems in Microfabricated Silicon-glass Chips," *Nucleic Acids Research*, vol. 24, pp. 380-385, 1996.

[38] J. Cheng, M. A. Shoffner, K. R. Mitchelson, L. J. Kricka, and P. Wilding, "Analysis of Ligase Chain Reaction Products Amplified in a Silicon-glass Chip Using Capillary Electrophoresis," *Journal of Chromatography A*, vol. 732, pp. 151-158, 1996.

[39] S. Lüdtke, T. Adam, and K. K. Unger, "Application of 0.5-µm Porous Silanized Silica Beads in Electrochromatography," *Journal of Chromatography A*, vol. 786, pp. 229-235, 1997.

[40] I. Sugimoto, M. Nakamura, and H. Kuwano, "Organic Gas Sorption Characteristics of Plasma-Deposited Amino Acid Films," *Analytical Chemistry*, vol. 66, pp. 4316-4323, 1994.

[41] R. R. Reston and E. S. Kolesar, Jr., "Sillicon-Micromachined Gas Chromatography System Used to Separate and Detect Ammonia and Nitrogen Dioxide--Part I: Design, Fabrication, and Integration of the Gas Chromatography System," *Journal of Microelectromechanical Systems*, vol. 3, pp. 134-146, 1994.

[42] S. Hannoe, I. Sugimoto, K. Yanagisawa, and H. Kuwano, "Enhanced Chromatographic Performance of Silicon-micromachined Capillary Column with Clean Structure and Interactive Plasma Organic Films," presented at 1997 International Conference on Solid-State Sensors and Actuators, Chicago, Illinois, USA, 1997.

[43] J. C. Giddings, "A New Separation Concept Based on a Coupling of Concentration and Flow Nonuniformities," *Separation Science*, vol. 1, pp. 123-125, 1966.

[44] T. L. Edwards, "Microfabricated Acoustic and Thermal Field-flow Fractionation Systems," in *School of Electrical and Computer Engineering*, vol. Doctor of Philosophy. Atlanta: Georgia Institute of Technology, 2005.

[45] G. H. Thompson, M. N. Myers, and J. C. Giddings, "Thermal Field-flow Fractionation of Polystyrene Samples," *Analytical Chemistry*, vol. 41, pp. 1219-1222, 1969.

[46] M. E. Hovingh, G. H. Thompson, and J. C. Giddings, "Column Parameters in Thermal Field-flow Fractionation," *Analytical Chemistry*, vol. 42, pp. 195-203, 1970.

[47] J. C. Giddings, M. E. Hovingh, and G. H. Thompson, "Measurement of Thermal Diffusion Factors by Thermal Field-flow Fractionation," *Journal of Physical Chemistry*, vol. 74, pp. 4291-4294, 1970.

[48] J. C. Giddings, F. J. F. Yang, and M. N. Myers, "Sedimentation Field-flow Fractionation," *Analytical Chemistry*, vol. 46, pp. 1917-1924, 1974.

[49] J. J. Kirkland and W. W. Yau, "Sedimentation Field-flow Fractionation: Applications," *Science*, vol. 218, pp. 121-127, 1982.

[50] J. C. Giddings, F. J. F. Yang, and M. N. Myers, "Flow Field-flow Fractionation: A Versatile New Separation Method," *Science*, vol. 193, pp. 1244-1245, 1976.

[51] J. C. Giddings, F. J. F. Yang, and M. N. Myers, "Theoretical and Experimental Characterization of Flow Field-flow Fractionation," *Analytical Chemistry*, vol. 48, pp. 1126-1132, 1976.

[52] J. Yang, Y. Huang, X.-B. Wang, F. F. Becker, and P. R. C. Gascoyne, "Cell Separation on Microfabricated Electrodes Using Dielectrophoretic/Gravitational Field-flow Fractionation," *Analytical Chemistry*, vol. 71, pp. 911-918, 1999.

[53] S. R. Springston, M. N. Myers, and J. C. Giddings, "Continuous Particle Fractionation Based on Gravitational Sedimentation in Split-flow Thin Cells," *Analytical Chemistry*, vol. 59, pp. 344-350, 1987.

[54] H. C. Berg, E. M. Purcell, and W. W. Stewart, "A Method for Separating According to Mass a Mixture of Macromolecules or Small Particles Suspended in a Fluid, II. Experiments in a Gravitational Field," *Proceedings of the National Academy of Sciences of the United States of America*, vol. 58, pp. 1286-1291, 1967.

[55] S. N. Semyonov and K. I. Maslow, "Acoustic Field-flow Fractionation," *Journal of Chromatography A*, vol. 446, pp. 151-156, 1988.

[56] N. Tri and R. Beckett, "The Use of Acoustic Forces in Thin Channel Separations," presented at Ninth International Symposium on Field-flow Fractionation, Golden, Colorado, 2001.

[57] K. D. Caldwell, L. F. Kesner, M. N. Myers, and J. C. Giddings, "Electrical Field-flow Fractionation of Proteins," *Science*, vol. 176, pp. 296-298, 1972.

[58] B. K. Gale, K. D. Caldwell, and A. B. Frazier, "A Micromachined Electrical Field-flow Fractionation (μ-EFFF) System," *IEEE Transactions on Biomedical Engineering*, vol. 45, pp. 1459-1469, 1998.

[59] B. K. Gale, K. D. Caldwell, and A. B. Frazier, "Geometric Scaling Effects in Electrical Field-flow Fractionation. 2. Experimental Results," *Analytical Chemistry*, vol. 74, pp. 1024-1030, 2002.

[60] B. K. Gale, K. D. Caldwell, and A. B. Frazier, "Geometric Scaling Effects in Electrical Field-flow Fractionation. 1.Theoretical Analysis," *Analytical Chemistry*, vol. 73, pp. 2345-2352, 2001.

[61] M. Graff and A. B. Frazier, "Visualization of Separation in a Micromachined Electrical Field-Flow Fractionation System (μ-ElFFF) with Complementary Optical and Electrical Detection Systems," presented at Ninth International Symposium on Field-Flow Fractionation, Golden, Colorado, 2001.

[62] B. K. Gale, "Scaling Effects in a Microfabricated Electrical Field-flow Fractionation System With an Integrated Detector," in *Department of Bioengineering*, vol. Doctor of Philosophy. Salt Lake City: University of Utah, 2000.

[63] S. C. Jacobson, A. W. Moore, and J. M. Ramsey, "Fused Quartz Substrates for Microchip Electrophoresis," *Analytical Chemistry*, vol. 67, pp. 2059-2063, 1995.

[64] A. W. Moore, Jr., S. C. Jacobson, and J. M. Ramsey, "Microchip Separations of Neutral Species via Micellar Electrokinetic Capillary Chromatography," *Analytical Chemistry*, vol. 67, pp. 4184-4189, 1995.

[65] E. Verpoorte, A. Manz, H. Lüdi, A. E. Bruno, F. Maystre, B. Krattiger, and H. M. Widmer, "A Silicon Flow Cell for Optical Detection in Miniaturized Total Chemical Analysis Systems," *Sensors and Actuators B*, vol. 6, pp. 66-70, 1992.

[66] C. S. Effenhauser, A. Manz, and H. M. Widmer, "Glass Chips for High-Speed Capillary Electrophoresis Separations with Submicrometer Plate Heights," *Analytical Chemistry*, vol. 65, pp. 2637-2642, 1993.

[67] G. Ocvirk, E. Verpoorte, A. Manz, and H. M. Widmer, "Integration of a Micro Liquid Chromatograph onto a Silicon Chip," presented at The 8th International Conference on Solid-State Sensors and Actuators, Stockholm, Sweden, 1995.

[68] E. S. Kolesar, Jr. and R. R. Reston, "Sillicon-Micromachined Gas Chromatography System Used to Separate and Detect Ammonia and Nitrogen Dioxide--Part II: Evaluation, Analysis, and Theoretical Modeling of the Gas Chromatography System," *Journal of Microelectromechanical Systems*, vol. 3, pp. 147-154, 1994.

[69] H. Nakanishi, T. Nishimoto, N. Nakamura, S. Nagamachi, A. Arai, Y. Iwata, and Y. Mito, "Fabrication of Electrophoresis Devices on Quartz and Glass Substrates Using a Bonding with HF Solution," presented at The Tenth Annual International Workshop on Micro Electro Mechanical Systems, Nagoya, Japan, 1997.

[70] M. Tswett, "On a New Category of Adsorption Phenomena and Their Application to Biochemical Analysis," presented at Proceedings of the Warsaw Society of Natural Sciences-Biological Section, 1903.

[71] M. S. Tswett, "Adsorptionsanalyse und chromatographische Methode. Anwendung an die Chemie des Chlorophylls," *Berichte der Deutschen Botanischen Gesellschaft*, vol. 24, pp. 316 and 384, 1906.

[72] M. Verzele and C. Dewaele, *Preparative High Performance Liquid Chromatography: A Practical Guideline*. Gent, Belgium: TEC, 1986.

[73] R. Kuhn and E. Lederer, *Berichte der Deutschen Chemischen Gesellschaft*, vol. 64, pp. 1349, 1931.

[74] R. Kuhn and E. Lederer, *Naturwissenschaften*, vol. 19, pp. 306, 1931.

[75] R. Kuhn, A. Winterstein, and E. Lederer, *Hoppe-Seyler's Zeitschrift fur Physiologische Chemie*, vol. 197, pp. 141, 1931.

[76] J. N. Wilson, "A Theory of Chromatography," *Journal of the American Chemical Society*, vol. 62, pp. 1583-1591, 1940.

[77] A. J. P. Martin and R. L. M. Synge, "A New Form of Chromatogram Employing Two Liquid Phases," *Biochemical Journal*, vol. 35, pp. 1358-1368, 1941.

[78] E. Glueckauf, "Theory of Chromatography. Part II. Chromatograms of a Single Solute," *Journal of the Chemical Society*, pp. 1302-1308, 1947.

[79] A. T. James and A. J. P. Martin, "Gas-liquid Partition Chromatography: the Separation and Micro-estimation of Volatile Fatty Acids from Formic Acid to Dodecanoic Acid," *Biochemical Journal*, vol. 50, pp. 679-690, 1952.

[80] A. J. P. Martin and R. L. M. Synge, "Separation of the Higher Monoamino-acids by Counter-current Liquid-liquid Extraction: The Amino-acid Composition of Wool," *Biochemical Journal*, vol. 35, pp. 91-121, 1941.

[81] J. H. Purnell, "The Correlation of Separating Power and Efficiency of Gas-chromatographic Columns," *Journal of the American Chemical Society*, pp. 1268-1274, 1960.

[82] H. M. N. H. Irving, H. Freiser, T. S. West, and International Union of Pure and Applied Chemistry. Analytical Chemistry Division., *Compendium of Analytical Nnomenclature: Definitive Rules 1977*, 1st ed. Oxford; New York: Pergamon Press, 1978.

[83] J. C. Giddings, "A New Separation Concept Based on Coupling of Concentration and Flow Nonuniformities," *Separation Science*, vol. 1, pp. 123-125, 1966.

[84] N.-T. Nguyen and S. T. Wereley, *Fundamentals and Applications of Microfluidics*. Boston: Artech House, 2002.

[85] J. C. Giddings, *Unified Separation Science*. New York: Wiley, 1991.

[86] S. Palkar and M. R. Schure, "Mechanistic Study of Electrical Field Flow Fractionation. 1. Nature of the Internal Field," *Analytical Chemistry*, vol. 69, pp. 3223-3229, 1997.

[87] C. M. A. Brett and A. M. O. Brett, *Electrochemistry: Principles, Methods, and Applications*. Oxford; New York: Oxford University Press, 1993.

[88] M. Dunkel, N. Tri, R. Beckett, and K. D. Caldwell, "Electrical field-flow fractionation: A tool for characterization of colloidal adsorption complexes," *Journal of Microcolumn Separations*, vol. 9, pp. 177-183, 1997.

[89] B. L. Karger, L. R. Snyder, and C. Horvâath, *An Introduction to Separation Science*. New York: Wiley, 1973.

[90] A. I. K. Lao, D. Trau, and I.-M. Hsing, "Miniaturized Flow Fractionation Device Assisted by a Pulsed Electric Field for Nanoparticle Separation," *Analytical Chemistry*, vol. 74, pp. 5364-5369, 2002.

[91] W. H. Coulter, "High Speed Automatic Blood Cell Counter and Cell Size Analyzer," *Medical Electronics*, vol. 12, pp. 1034-1042.

[92] D. Satake, H. Ebi, N. Oku, K. Matsuda, H. Takao, M. Ashiki, and M. Ishida, "A Sensor for Blood Cell Counter Using MEMS Technology," *Sensors and Actuators B*, vol. 83, pp. 77-81, 2002.

[93] J. Tyndall, "On the Blue Colour of the Sky, the Polarization of Skylight, and on the Polarization of Light by Cloudy Matter Generally," *Proceedings of the Royal Society of London*, vol. 17, pp. 223-233, 1869.

[94] L. Rayleigh, *Philosophical Magazine*, vol. 41, pp. 107-120, 1871.

[95] L. Rayleigh, *Philosophical Magazine*, vol. 41, pp. 274-279, 1871.

[96] G. Mie, *Ann. der Phys.*, vol. 25, pp. 377-445, 1908.

[97] J. Yguerabide and E. E. Yguerabide, "Light-scattering Submicroscopic Particles as Highly Fluorescent Analogs and Their Use as Tracer Labels in Clinical and Biological Applications 1. Theory," *Analytical Biochemistry*, vol. 262, pp. 137-156, 1998.

[98] M. Kerker, *The Scattering of Light, and Other Electromagnetic Radiation*. New York: Academic Press, 1969.

[99] *Tables of Scattering Functions for Spherical Particles*: U. S. Government, 1949.

[100] J. Yguerabide and E. E. Yguerabide, "Light-scattering Submicroscopic Particles as Highly Fluorescent Analogs and Their Use as Tracer Labels in Clinical and Biological Applications II. Experimental Characterization," *Analytical Biochemistry*, vol. 262, pp. 157-176, 1998.

[101] H. C. v. d. Hulst, *Light Scattering by Small Particles*. New York: Wiley, 1957.

[102] C. F. Bohren, "Recurrence Relations for the Mie Scattering Coefficients," *Journal of the Optical Society of America A*, vol. 4, pp. 612-613, 1987.

[103] C. F. Bohren and D. R. Huffman, *Absorption and Scattering of Light by Small Particles*. New York: Wiley, 1983.

[104] M. Horisberger, *Scanning Electron Microscopy*, vol. 2, pp. 9-31, 1981.

[105] M. Horisberger and M. F. Clerc, *Histochemistry*, vol. 82, pp. 219-223, 1985.

[106] S. L. Goodman, B. M. Hodges, L. K. Trejdosiewiczk, and D. C. Livingston, *Scanning Electron Microscopy*, vol. 3, pp. 619-628, 1979.

[107] W. P. Faulk and G. M. Taylor, *Immunochemistry*, vol. 8, pp. 1081-1083, 1971.

[108] W. D. Geoghegan and G. A. Ackerman, *Journal of Histochemistry and Cytochemistry*, vol. 25, pp. 1187-1200, 1977.

[109] M. Schimpf, K. D. Caldwell, and J. C. Giddings, *Field-flow Fractionation Handbook*. New York: Wiley-Interscience, 2000.

[110] K.-H. Heng, W. Wang, and M. C. Murphy, "UV-LIGA Microfabrication and Test of an AC-Type Micropump Based on the Magnetohydrodynamic (MHD) Principle," *Proceedings of SPIE*, vol. 4177, pp. 174-184, 2000.

[111] K.-S. Yun, I.-J. Cho, J.-U. Bu, G.-H. Kim, Y.-S. Jeon, C.-J. C. Kim, and E. Yoon, "A Micropump Driven by Continuous Electrowetting Actuation for Low Voltage and Low Power Operations," pp. 487-490, 2001.

[112] F. A. Shaikh and V. M. Ugaz, "Enhanced Separation Performance in Microfabricated Electrophoresis Devices by Electric Field Induced Collection and Metering of DNA," presented at NSTI Nanotechnology Conference and Trade Show, Anaheim, California, 2005.